APPLICATION OF BIOCHAR IN SUSTAINABLE CEMENT-BASED COMPOSITES

LIANG CHEN

PhD

The Hong Kong Polytechnic University

2022

The Hong Kong Polytechnic University

Department of Civil and Environmental Engineering

Application of Biochar in Sustainable Cement-based Composites

LIANG CHEN

A thesis submitted in partial fulfilment of the
requirements for the degree of Doctor of Philosophy

March 2022

CERTIFICATE OF ORIGINALITY

I hereby declare that this thesis is my own work and that, to the best of my knowledge and belief, it reproduces no material previously published or written, nor material that has been accepted for the award of any other degree or diploma, except where due acknowledgement has been made in the text.

The work presented in Chapter 3 was previously published in *Chemical Engineering Journal* as "Roles of biochar in cement-based stabilization/solidification of municipal solid waste incineration fly ash" by Liang Chen (first author, student), Lei Wang (corresponding author, co-supervisor) and Daniel C. W. Tsang (corresponding author, chief supervisor) and others.

The work presented in Chapter 4 was previously published in *ACS Sustainable Chemistry* as "Roles of biochar and CO_2 curing in sustainable magnesia cement-based Composites" by Lei Wang (co-first author, co-supervisor), Liang Chen (co-first author, student) and Daniel C. W. Tsang (corresponding author, chief supervisor) and others.

The work presented in Chapter 5 was previously published in *Chemical Engineering*

Journal as “Biochar-augmented carbon-negative concrete” by Liang Chen (first author, student), Lei Wang (corresponding author, co-supervisor) and Daniel C. W. Tsang (corresponding author, chief supervisor) and others.

These mentioned studies were conceived by all of the authors. I designed the studies, carried out the tests, data collection and analysis, took the lead in writing the manuscript. All the authors contributed to the final version of the manuscript.

____

CHEN Liang (Name of the student)

ABSTRACT

Biochar is a known product to permanently remove carbon from its cycle. It is essential to find high-quality and large-quantity utilization for biochar. Application of biochar in cement-based composite to produce low carbon and even carbon-negative construction material is a promising technology to achieve circular economy and carbon neutrality.

This study investigated the roles of carbon-negative rice husk biochar (RBC) and yard waste biochar (YBC) as green additives in the cement system. Experimental results illustrated that the addition of both biochars promoted cement hydration reaction via pozzolanic reaction and internal curing. In particular, the incorporation of 10 wt.% RBC (rich in activated Si) significantly increased the content of calcium-silicate-hydrate (C-S-H) gel from 41.6 wt.% (control sample) to 52.0 wt.% and increased the average degree of connectivity of C-S-H gel from 1.43 to 1.52 as indicated by quantitative X-ray diffraction and ^{29}Si nuclear magnetic resonance analysis. In addition, the low-carbon biochar cement binder was applied for stabilization/solidification (S/S) of municipal solid waste incineration (MSWI) fly ash. The incorporation of RBC and YBC (20 or 30 wt.%) enhanced the immobilization efficiency of potentially toxic elements in MSWI fly ash due to the additional hydration products and high adsorption ability of biochar. For instance, in R-80FA and Y-80FA samples (namely, 20 wt.% binder dosage, of which RBC or YBC accounted for 10 wt.% of binder), the immobilization efficiency for Pb could reach 96.2% and comply with the leachability limit. The biochar-modified S/S blocks achieved comparable strength to the cement-based S/S blocks, presenting a mechanically stable

solidified matrix for engineering application. Therefore, this study expands the emerging application of biochar and demonstrates that biochar-augmented binder can ensure low-carbon and high-performance S/S of hazardous materials.

This study also assessed the efficacy of biochar on the hydration of magnesia cement (MC) and magnesia cement−Portland binary cement (MP)-based pastes and evaluated the synergistic effect of biochar and CO_2 curing on the pastes. The thermogravimetric and X-ray diffraction analyses showed that the incorporation of biochar, especially CO_2 gasification biochar, promoted the generation of hydration products due to the internal curing effect. The use of CO_2 curing effectively accelerated the carbonation of pastes. Hydrated magnesium carbonates were preferentially formed in CO_2-cured MC pastes, whereas $CaCO_3$ was preferentially generated in CO_2-cured MP pastes. Moreover, the incorporation of biochar, especially porous CO_2 gasification biochar, could further facilitate CO_2 diffusion and promote carbonation. As a result, the synchronous use of biochar and CO_2 curing significantly enhanced the mechanical strength of blocks. Therefore, biochar-augmented and CO_2-enhanced composites could be novel and low-carbon construction materials for sustainable engineering applications.

Based on the above findings, this study proposed a revolutionary design of carbon-negative concrete with a large volume of biochar incorporation and elaborated the roles of biochar in the cement hydration and microstructure development of biochar-augmented concrete. The total CO_2 emissions and economic values of biochar-augmented concrete were, for the first time, quantified by conducting life cycle assessment and cost-benefit analysis. Pre-soaked biochar as aggregate in concrete

promoted the cement hydration process, facilitating the formation of C-S-H gel and enhancing the polymerization degree of C-S-H gel via internal curing. The incorporation of supplementary cementitious materials (SCMs) in the binder further enhanced the mechanical strength of biochar-augmented concrete via time-dependent pozzolanic reaction. The life cycle assessment confirmed that the biochar incorporation significantly reduced CO_2 emissions, and most importantly, the combined use of biochar and SCMs successfully achieved carbon-negative concrete production. Preliminary cost and benefit analysis illustrated that the biochar-augmented concrete could yield satisfactory overall economic profits. Considering the mechanical performance, resource availability, negative CO_2 emissions, and economic profits, the 30BC-MK (with biochar as aggregate and metakaolin as a binder representing 30 wt.% and 9 wt.%, respectively) was the most promising mixture, which could sequester 59 kg CO_2 tonne^{-1} and potentially generate the overall profit of 35.4 USD m^{-3}. In summary, our novel design of biochar-augmented concrete can open up a new field of biochar application that produces technically feasible and financially profitable carbon-negative construction materials.

PUBLICATIONS ARISING FROM PHD STUDY

<u>First Author Journal Papers of Biochar Cement based Composites:</u>

1. **Chen, L.,** Wang, L., Zhang, Y., Ruan, S., Mechtcherine, V., Tsang, D.C.W., 2022. Roles of biochar in cement-based stabilization/solidification of municipal solid waste incineration fly ash. Chem. Eng. J. 430, 132972. doi:10.1016/j.cej.2021.132972.
2. **Chen, L.,** Wang, L., Ruan, S., Mechtcherine, V., Tsang, D.C.W., 2022. Biochar-augmented carbon-negative concrete. Chem. Eng. J. 133946. https://doi.org/10.1016/j.cej.2021.133946.
3. Wang, L.# (co-first author), **Chen, L.# (co-first author)**, Poon, C.S., Wang, C.H., Ok, Y.S., Mechtcherine, V., Tsang, D.C.W., 2021. Roles of biochar and CO_2 curing in sustainable magnesia cement-based composites. ACS Sustain. Chem. Eng. 9, 8603-8610. https://doi.org/10.1021/acssuschemeng.1c02008.
4. **Chen, L.,** Wang, L., Cho, D.W., Tsang, D. C. W., Tong, L., Zhou, Y., Yang, J., Hu, Q., Poon, C. S., 2019. Sustainable stabilization/solidification of municipal solid waste incinerator fly ash by incorporation of green materials. J. Clean. Prod., 222, 335–343. https://doi.org/10.1016/j.jclepro.2019.03.057. (ESI Highly Cited)

Book Chapters of Biochar Cement based Composites:

Chen, L., Wang, L., 2021. Biochar for green and sustainable stabilization/solidification. Chapter 6, Low Carbon Stabilization and Solidification of Hazardous Wastes. Elsevier ISBN: 978-0-12-824004-5.

First Author Journal Papers of Other Waste Recycling:

1. **Chen, L.,** Wang, Y. S., Wang, L., Zhang, Y., Li, J. Tong, L. Hu, Q. Dai, J. G., Tsang, D. C. W., 2020. Stabilisation/solidification of municipal solid waste incineration fly ash by phosphate-enhanced calcium aluminate cement. J. Hazard. Mater., 124404 https://doi.org/10.1016/j.jhazmat.2020.124404.
2. **Chen, L.,** Wang, L., Tsang, D. C. W., Mechtcherine, V., Poon, C. S., 2020. Efficacy of green alternatives and carbon dioxide curing in reactive magnesia cement-bonded particleboards. J. Clean. Prod., 258, 120997. https://doi.org/10.1016/j.jclepro.2020.120997.

Other Journal Papers of Biochar Cement based Composites:

1. Wang, L., **Chen, L.,** Tsang, D. C. W., Guo, B.; Yang, J., Shen, Z., Hou, D., Sik, Y., Sun, C., 2020 Biochar as green additives in cement-based composites with carbon dioxide curing. J. Clean. Prod., 258, 120678. https://doi.org/10.1016/j.jclepro.2020.120678 (ESI Highly Cited).
2. Wang, L., **Chen, L.,** Tsang, D. C. W., Kua, H. W., Yang, J., Ok, Y. S., Ding, S., Hou, D., Poon, C. S. 2019. The roles of biochar as green admixture for sediment-based construction products. Cem. Concr. Compos., 104, 103348. https://doi.org/10.1016/j.cemconcomp.2019.103348.

<u>Other Journal Papers of Other Waste Recycling:</u>

3. Wang, L., Zhang, Y., **Chen, L.**, Guo, B., Tan, Y., Sasaki, K., Tsang, D.C.W., 2022. Designing novel magnesium oxysulfate cement for stabilization/solidification of municipal solid waste incineration fly ash. J. Hazard. Mater. 423. doi:10.1016/j.jhazmat.2021.127025.
4. Sun, J., Wang, L., Yu, J., Guo, B., **Chen, L.**, Zhang, Y., Wang, D., Shen, Z., Tsang, D.C.W., 2022. Cytotoxicity of stabilized/solidified municipal solid waste incineration fly ash. J. Hazard. Mater. 424. doi:10.1016/j.jhazmat.2021.127369.
5. Wang, L., Ur, N.; Curosu, I., Zhu, Z., Abdul, M., Beigh, B., Liebscher, M., **Chen, L.,** Tsang, D. C. W., Hempel, S., Mechtcherine, V. 2021. On the Use of Limestone Calcined Clay Cement (LC3) in High-Strength Strain-Hardening Cement-Based Composites (HS-SHCC). Cem. Concr. Res., 144, 106421. https://doi.org/10.1016/j.cemconres.2021.106421.
6. Guo, B., Tan, Y., Wang, L., **Chen, L.,** Wu, Z., Sasaki, K., Mechtcherine, V., Tsang, D.C.W., 2021. High-efficiency and low-carbon remediation of zinc contaminated sludge by magnesium oxysulfate cement. J. Hazard. Mater. 408. doi:10.1016/j.jhazmat.2020.124486.
7. Zhang, Y., Wang, L., **Chen, L.,** Ma, B., Zhang, Y., Ni, W., Tsang, D.C.W., 2021. Treatment of municipal solid waste incineration fly ash: State-of-the-art technologies and future perspectives. J. Hazard. Mater. doi:10.1016/j.jhazmat.2021.125132.
8. Li, J., **Chen, L.,** Zhan, B., Wang, L., Poon, C.S., Tsang, D.C.W., 2021. Sustainable stabilization/solidification of arsenic-containing soil by blast slag and cement blends. Chemosphere 271. doi:10.1016/j.chemosphere.2021.129868.

9. Zhang, Y., Labianca, C., **Chen, L.,** De Gisi, S., Notarnicola, M., Guo, B., Sun, J., Ding, S., Wang, L., 2021. Sustainable ex-situ remediation of contaminated sediment: A review. Environ. Pollut. 287. doi:10.1016/j.envpol.2021.117333.
10. Wang, L., **Chen, L.,** Tsang, D.C.W., 2020. Green remediation by using low-carbon cement-based stabilization/solidification approaches, in: Sustainable Remediation of Contaminated Soil and Groundwater. pp. 93–118. doi:10.1016/b978-0-12-817982-6.00005-7.
11. Hossain, M.U., Wang, L., **Chen, L.,** Tsang, D.C.W., Ng, S.T., Poon, C.S., Mechtcherine, V., 2020. Evaluating the environmental impacts of stabilization and solidification technologies for managing hazardous wastes through life cycle assessment: A case study of Hong Kong. Environ. Int. 145. doi:10.1016/j.envint.2020.106139
12. Wang, L., **Chen, L.,** Guo, B., Tsang, D.C.W., Huang, L., Ok, Y.S., Mechtcherine, V., 2020. Red mud-enhanced magnesium phosphate cement for remediation of Pb and As contaminated soil. J. Hazard. Mater. 400. doi:10.1016/j.jhazmat.2020.123317.
13. Wang, L., **Chen, L.,** Tsang, D.C.W., 2020. Green and sustainable stabilization/solidification, in: soil and groundwater remediation technologies. 213–222. doi:10.1201/9780429322563-15.
14. Xiong, X., Yu, I.K.M., Tsang, D.C.W., **Chen, L.,** Su, Z., Hu, C., Luo, G., Zhang, S., Ok, Y.S., Clark, J.H., 2020. Study of glucose isomerisation to fructose over three heterogeneous carbon-based aluminium-impregnated catalysts. J. Clean. Prod. 268. doi:10.1016/j.jclepro.2020.122378
15. Wang, L., **Chen, L.,** Tsang, D. C. W., Zhou, Y., Rinklebe, J., Song, H.; Kwon, E. E., Baek, K., Sik Ok, Y., 2019. Mechanistic insights into red mud, blast furnace

slag, or metakaolin-assisted stabilization/solidification of arsenic-contaminated sediment. Environ. Int., 133, 105247. https://doi.org/10.1016/j.envint.2019.105247.

16. Wang, L., **Chen, L.,** Provis, J. L., Tsang, D. C. W., Poon, C. S., Accelerated carbonation of reactive mgo and portland cement blends under flowing CO_2 gas., 2020. Cem. Concr. Compos. 106, 103489. https://doi.org/10.1016/j.cemconcomp.2019.103489 (ESI Highly Cited).
17. Wang, L., **Chen, L.,** Cho, D.W., Tsang, D.C.W., Yang, J., Hou, D., Baek, K., Kua, H.W., Poon, C.S., 2019. Novel synergy of Si-rich minerals and reactive MgO for stabilisation/solidification of contaminated sediment. J. Hazard. Mater. 365, 695–706. doi:10.1016/j.jhazmat.2018.11.067 (ESI Highly Cited).
18. Wang, L., **Chen, L.,** Tsang, D. C. W., Li, J. S., Baek, K., Hou, D., Ding, S., Poon, C. S., 2018. Recycling dredged sediment into fill materials, partition blocks, and paving blocks: technical and economic assessment. J. Clean. Prod., 199, 69–76. https://doi.org/10.1016/j.jclepro.2018.07.165.
19. Wang, L., **Chen, L.,** Tsang, D.C.W., Li, J.S., Yeung, T.L.Y., Ding, S., Poon, C.S., 2018. Green remediation of contaminated sediment by stabilization/solidification with industrial by-products and CO_2 utilization. Sci. Total Environ. 631–632, 1321–1327. doi:10.1016/j.scitotenv.2018.03.103.

ACKNOWLEDGEMENTS

At the end of my PhD journey, I would like to thank all the people who have given me support. Foremost, I would like to express my deepest appreciation to my chief supervisor, Prof. Dan Tsang for granting me the opportunity to do research with so many talented groupmates. He suggested me this innovative research direction, provided me with a lot of insights for my research works and taught me to think critically and deeply. He always pushed my limits and motivated me to step out of my comfort zone. I would like to extend my greatest thanks to my co-supervisor Prof. Lei Wang, who brought me into this area of cementitious materials, provided me with countless timely and meticulous suggestions for my lab work and paperwork. They have always been my role models, inspiring me to move forward. This thesis would not be accomplished without their great guidance, supervision and support throughout my PhD study. In my future academic career, I will follow their footsteps to be an integrity researcher.

I warmly thank all the laboratory technicians, Mr K. H. Wong, Ms. H.Y. Chan, Mr W. S. Lam and the others for helping me carry out time-consuming tests. I wish to acknowledge former postgraduate and undergraduate students, Z.Z. Wang, Z.H. Zhang, Henry, M.H. Ho for helping me conduct various experimental works.

I also want to thank all my talented groupmates, Xiaohong Zhu, Yuying Zhang, Zhonghao Wan, Mingjing He, Zibo Xu, Qiaozhi Zhang, Shuguang Xu, Mingzhe Su, Tiffany Mak, Xinxi Xiong, Season Chen, Iris Yu, and the others. They always

provided a hard-working atmosphere to motivate me. Their generous help and support for my research work and daily life are also acknowledged. Our revolutionary friendship during these extraordinarily tough years in Hong Kong will never be forgotten.

My sincere appreciations also go to my parents, grandpa and grandma, who are always proud of me and provided me unconditional support and encouragement. Last but not the least, I am much indebted to my beloved wife Lindan Guo. Without her greatest love, support, understanding and sacrifices through the long stressful study, I would not have been able to concentrate on my research work. For the rest of my life, I will try my best to reward the love of my family.

2 CONTENTS

CERTIFICATE OF ORIGINALITY I

ABSTRACT III

ACKNOWLEDGEMENTS XI

LIST OF FIGURES XVI

LIST OF TABLES XIX

LIST OF ABBREVIATIONS 1

CHAPTER 1. INTRODUCTION 4

1.1 Background 4

1.2 Research objective and scope 5

1.3 Thesis organization 6

CHAPTER 2. LITERATURE REVIEW 8

2.1 Biochar background 8

2.1.1 Production of biochar 8

2.1.2 Conventional application of biochar 8

2.2 Biochar properties affecting cement system 9

2.2.1 Chemical composition of biochar 9

2.2.2 Physical properties of biochar 10

2.3 Incorporation of biochar in different cement-system 12

2.3.1 Biochar in OPC system 12

2.3.2 Biochar in OPC-SCMs system 14

2.3.3 Biochar in Magnesia cement-system 16

2.4 Different application biochar cement composite... 18

2.4.1 Application of biochar in cement-based stabilization/solidification of wastes 18

2.4.2 Development of different biochar construction products..................... 19

CHAPTER 3. BIOCHAR CEMENT-COMPOSITE AND ITS APPLICATION IN STABILIZATION/SOLIDIFICATION OF MUNICIPAL SOLID WASTE INCINERATION FLY ASH 21

3.1 Introduction 21

3.2 Materials and methods 23

3.2.1 Materials.. 23

3.2.2 Sample preparation.. 25

3.2.3 Characterization methods.. 27

3.3 Results and discussion 28

3.3.1 Development of biochar cement-composite.. 28

3.3.2 Biochar cement composite for stabilization/solidification of MSWI FA.. 40

3.4. Conclusions.. 45

CHAPTER 4. ROLES OF BIOCHAR IN SUSTAINABLE MAGNESIA CEMENT- BASED COMPOSITES UNDER AIR CURING AND CO_2 CURING 47

4.1 Introduction... 47

4.2 Materials and methods 49

4.2.1 Materials.. 49

4.2.2 Sample preparation.. 50

4.2.3 Characterization methods..51

4.3 Results and discussion 52

4.3.1 Different biochar in magnesia cement systems under air curing 52

4.3.2 Synergistic effects of biochar and CO_2 curing on the cement systems.....58

4.4. Conclusions..62

CHAPTER 5. DEVELOPMENT OF BIOCHAR-AUGMENTED CARBON-NEGATIVE CONCRETE..64

5.1 Introduction..64

5.2 Materials and methods 65

5.2.1 Materials..65

5.2.2 Sample preparation..67

5.2.3 Characterization methods..69

5.3 Results and Discussion..72

5.3.1 Hydration reaction of biochar mortar..72

5.3.2 Efficacy of SCMs on biochar-augmented concrete..................................79

5.3.3 Microstructure and mechanical properties of the biochar mortar 85

5.3.4. LCA and CBA of the biochar blocks..89

5.4 Conclusions..93

CHAPTER 6. CONCLUSIONS AND PERSPECTIVES 95

REFERENCES..98

APPENDIX-SUPPLEMENTARY INFORMATION...119

List of Figures

Figure 3.1. Isothermal conduction calorimetry results of pastes with/without biochar (a) & (b) cumulative hydration heat per cement; (c) & (d) rate of hydration heat per cement (Stage I: initial period; Sage II: acceleration period; Stage III: deceleration period; Stage IV: slow reaction period). 30

Figure 3.2. (a) & (b) DTG curves of the 28-d pastes with/without biochar and (c) corresponding bound water of C-S-H and CH (Peak I: dehydration of C-S-H; Peak II: dehydroxylation of CH; Peak III: decarbonation of CC). 32

Figure 3.3. Results of analytical investigation of the 28-d pastes with/without biochar: (a) & (b) XRD patterns; (c) Q-XRD analysis; (d) C-S-H content calculation from Q-XRD analysis. 34

Figure 3.4. ^{29}Si NMR spectra for the 28-d pastes with/without biochar. 36

Figure 3.5. BSE/SEM images and elemental mapping of 28-d pastes with/without biochar: (a) BSE images; (b) SEM images; (c) SEM images elemental mapping of YBC-10; (d) elemental mapping of RBC-10. 37

Figure 3.6. Compressive strength of 7-d and 28-d pastes with/without biochar. 39

Figure 3.7. Results of analytical investigation of the 28-d MSWI fly ash S/S blocks: (a) DTG curves; (b) XRD patterns. 41

Figure 3.8. SEM images and elemental mapping of 28-d MSWI fly ash S/S blocks: (a) SEM images; (b) elemental mapping of R-90FA. 42

Figure 3.9. (a) TCLP leachability and (b) compressive strength of MSWI fly ash S/S blocks (Leachability limits of trace elements: 0.6 mg L^{-1} of Cr, 0.2 mg L^{-1} of Cu, 4.3 mg L^{-1} Zn, 5 mg L^{-1} of As, 0.75 mg L^{-1} of Pb; red line at 1 MPa: minimum required strength for fill materials; red line at 7 MPa: minimum required strength for partition

blocks). 44

Figure 4.1. DTG curves and XRD diffractograms of 28-d air cured MC and MP pastes with biochar addition: (a) DTG of MC pastes; (b) XRD diffractograms of MC pastes; (c) DTG of MP pastes; (d) XRD diffractograms of MP pastes. 54

Figure 4.2. Compressive strength of air cured MC and MP blocks with biochar addition (the letters (a-f) denote statistically significant differences of the experimental results). 58

Figure 4.3. DTG curves and XRD diffractograms of biochar-incorporated MC and MP pastes after 1-d CO_2 plus 6-d air curing: (a) DTG of CO_2 cured MC pastes; (b) XRD diffractograms of CO_2 cured MC pastes; (c) DTG of CO_2 cured MP pastes; (d) XRD diffractograms of CO_2 cured MP pastes. 59

Figure 4.4. SEM images and elemental mapping of biochar-incorporated MC pastes after 1-d CO_2 plus 6-d air curing: (a) SEM images of MC, MC-Air BC and MC-CO_2 BC samples; (b) Element mapping of MC sample; and (c) Element mapping of MC-CO_2 BC sample. 60

Figure 4.5. Compressive strength of CO_2 cured MC and MP blocks with biochar addition (the letters (a-f) denote statistically significant differences of the experimental results). 62

Figure 5.1. Isothermal conduction calorimetry results of biochar mortar: (a) cumulative hydration heat per cement and (b) rate of hydration heat per cement (Stage I: initial period; Stage II: acceleratory period; Stage III: deceleration period; Stage IV: slow reaction period). 74

Figure 5.2. (a) DTG curves and (b) XRD patterns of the 28-d biochar mortar.........76

Figure 5.3. ^{29}Si NMR spectra for the 28-d biochar mortar......................................78

Figure 5.4. Isothermal conduction calorimetry results of biochar mortar with SCMs

incorporation (a) cumulative hydration heat per binder and (b) rate of hydration heat per binder. 81

Figure 5.5. (a) DTG curves and (b) XRD patterns of the 28-d biochar mortar with SCMs incorporation. 83

Figure 5.6.^{29}Si NMR spectra for the 28-d biochar mortar with SCMs incorporation. 85

Figure 5.7. BSE images of the 28-d biochar mortar. 86

Figure 5.8. X-ray CT scan images of the 28-d biochar mortar (cement clinkers were highlighted in yellow color). 88

Figure 5.9. Compressive strength of the 3-d and 28-d biochar blocks (red line at 7 MPa: the required strength for partition blocks). 89

Figure 5.10. (a) carbon footprint and (b) cost and benefit of biochar blocks. 91

List of Tables

Table 3.1 Basic information of biochar. 24

Table 3.2 Mixture design (wt.%) of biochar modified pastes and MSWI fly ash S/S blocks. 26

Table 4.1 Basic information of air and CO_2 gasification biochar. 49

Table 5.1 Chemical composition of raw materials (wt.%). 66

Table 5.2 Basic information of biochar. 66

Table 5.3 Mixture design (wt.%) of biochar block and biochar mortar. 68

Table 5.4 Calculation results of ^{29}Si NMR spectra. 79

List of Abbreviations

AFm	Alumina ferric oxide mono
AFt	Ettringite
BET	Brunauer-Emmett-Teller
BSE	Back scattering electron
C_3A	Tricalcium aluminate
C_2S	Dicalcium silicate
C_3S	Tricalcium silicate
CBA	Cost-benefit analysis
CC	$CaCO_3$
CCUS	Carbon capture utilisation and storage
CETS	Carbon Emissions Trading Scheme
CH	$Ca(OH)_2$
C-S-H	Calcium-silicate-hydrate
CT	Computed tomography
DoH	Degree of hydration
DTG	Derivative thermogravimetric analysis
EDX	Energy-dispersive X-ray spectroscopy
GGBS	Ground granulated blast furnace slag
Hc	Hemicarboaluminate
HMC	Hydrated magnesium carbonates
ICC	Isothermal conduction calorimetry
ICP	Inductively coupled plasma

IPCC	Intergovernmental Panel on Climate Change
ITZ	Interfacial transition zone
LCA	Life cycle assessment
MC	Magnesia cement
Mc	Monocarboaluminate
MCL	Mean chain length
MIP	Mercury intrusion porosimetry
MK	Metakaolin
MP	Magnesia-Portland binary cement
MPC	Magnesium phosphate cemen
MSWI	Municipal solid waste incineration
NMR	Nuclear magnetic resonance
OPC	Ordinary Portland cement
PDXL	Powder diffraction software
PFA	Pulverized fly ash
PTEs	Potentially toxic elements
Q-XRD	Quantitative X-ray diffraction
RBC	Rice husk biochar
S/S	Stabilization/solidification
SCMs	Supplementary cementitious materials
SEM	Scanning electron microscopy
SF	Silica fume
SSD	Saturated surface dry
TCLP	Toxicity characteristic leaching procedure

TGA	Thermogravimetric analysis
WPPF	Whole powder pattern fitting
XRD	X-ray diffraction
XRF	X-ray fluorescence
YBC	Yard waste biochar

CHAPTER 1. Introduction

1.1 Background

Global warming and climate change cause severe impacts on ecosystems and human health. Reducing CO_2 emission and holding the elevation of global temperature have been an international consensus. In 2020, China, the world's biggest CO_2 emitter, aims to hit peak emissions before 2030 and achieve carbon neutrality by 2060 (BBC, 2020a) while European Commission agrees on a target that reduces the emission of greenhouse gases by 55% before 2030 and reaches a goal of net-zero emissions by 2050 (BBC, 2020b). Carbon capture, utilization and storage (CCUS) technologies should be developed to achieve the ambitious target of carbon neutrality (Hepburn, et al., 2019). Biochar is a carbon-enriched by-product obtained from pyrolysis of biomass with a limited supply of oxygen (Dissanayake, et al., 2020). The application of biochar is considered as one of the six most promising approaches to permanently remove carbon from its cycle as suggested by the Intergovernmental Panel on Climate Change (IPCC), because biochar can bind 2.0-2.6 tonnes of CO_2 compared to its own weight (Azzi, et al., 2019). Nowadays, biochar is mainly used as soil amendments (Xiong et al., 2017),however, some biomass waste streams are considered not suitable for use as a feed additive or soil conditioner due to the presence of impurities of potentially toxic elements (Liu et al., 2018; Wang et al., 2017). Moreover, limited farmland in densely-populated regions cannot accommodate abundant amount of biochar for soil application. Innovative and green use of biochar in the construction industry will open up a new field for the sake of carbon neutrality and a circular economy. The demand for cement and concrete as building materials is tremendous and constantly increasing with the rapid urbanization process. For instance, more than 10 billion tonnes of concrete were consumed in 2018, which was the second most consumable material only behind water (Scrivener et al., 2018). Since the production of ordinary Portland cement (OPC) generated substantial amount of CO_2 emission (0.8-1.0 tonne CO_2 per tonne), contributing to approximately 10% of global CO_2 emission (Geng et al., 2019), the use of carbon-negative biochar to partially substitute cement could remarkably alleviate the carbon footprint. Therefore, further studies are needed to develop and understand the biochar-cement composites

1.2 Research objective and scope

This study aims to develop different applications of low carbon or carbon-negative biochar-cement composites with excellent performance. The specific objectives of this study are listed as follows:

- Explore the mechanisms of biochar on the cement hydration, microstructure, and mechanical performance of biochar cement composite.
- Elucidate the mechanisms of biochar in changing the hydration progress, microstructure, and mechanical strength of the OPC and (magnesia cement) MC composites,
- Unravel the interplay between biochar and CO_2 curing for the accelerated carbonation of OPC and MC composites.
- Unlock the application of biochar in cement-based stabilization/solidification (S/S).
- Elaborate the roles of waste-derived biochar as aggregate in the cement hydration, microstructure, and strength development of biochar-augmented

concrete by advanced characterization techniques;

- Investigate the effects of various widely available supplementary cementitious materials (SCMs) on the cement chemistry and mechanical properties of biochar-augmented concrete;
- Quantify and justify the total CO_2 emissions and economic value of biochar-augmented concrete by means of life cycle assessment (LCA) and cost-benefit analysis (CBA).

1.3 Thesis organization

Chapter 1 introduces the research background, research objective and scope, and the structure of this thesis.

Chapter 2 states the current situation of biochar production, the conventional application of biochar, and the incorporation of biochar into cement-system. In addition, it summarizes the chemical composition and physical properties of biochar affecting the cement system. The third section of this chapter reviews the research related to the application of biochar in different cement systems. Moreover, it reviews the different applications of biochar and states the potential applications of biochar construction products.

Chapter 3 explores the roles of rise husk and yard waste biochar in cement system and investigated the application of biochar cement composite for S/S of municipal solid waste incineration fly ash(MSWI FA). The biochar-cement S/S blocks achieved comparable strength to the cement-based S/S blocks, presenting a mechanically stable solidified matrix for engineering application.

Chapter 4 investigates the efficacy of biochar on the hydration of magnesia cement−Portland binary cement (MP)-based pastes and MC and evaluated the synergistic effect of biochar and CO_2 curing on the pastes. It highlights that the incorporation of gasification biochar promoted the generation of hydration products and facilitated the CO_2 diffusion.

Chapter 5 develops an innovative technology of carbon-negative concrete with a large volume of biochar incorporation and elaborated the roles of biochar in the cement hydration and microstructure development of biochar-augmented concrete. It also assesses the CO_2 emissions and cost-benefit of the biochar-augmented concrete.

Chapter 6 presents the conclusions of the whole thesis. Recommendations for future research are discussed as well.

CHAPTER 2. Literature Review

2.1 Biochar background

2.1.1 Production of biochar

Biochar is a carbon-enriched by-product obtained from pyrolysis of biomass with limited supply of oxygen (Sun et al., 2021; He et al., 2021). During the pyrosis, volatile matter is released from the raw material, and most of the carbon can be retained in biochar in a highly stable form with limited CO_2 emissions. The release of volatile matter creates a honeycomb-like porous structure in the produced biochar with high specific surface area. The co-products (e.g., bio-oil and pyrolytic gas) can be used for bioenergy applications. The production of biochar can be affected by many factors, including the equipment, feedstock, temperature and different modification techniques (Wang et al., 2020a). Different types of feedstock include wood waste, food waste, industrial waste, fruit shells, crop residues and manure. Therefore, the application of the biochar from the different feedstocks, by different methods need to be systematically characterized.

2.1.2 Conventional application of biochar

Up to date, biochar has been mainly used as soil amendments in the agricultural industry. The addition of porous biochar could improve the water holding capacity and immobilize the contaminant in soil. In addition, biochar could also provide nutrients facilitating the plant growth (Sashidhar et al., 2020). However, it is difficult for biochar to demonstrate its full potential in densely populated metropolitan area with limited farmland. Due to the superior adsorption properties, biochar has also been applied in wastewater treatment to adsorb and remove contaminants. Using biochar in wastewater treatment. Nevertheless, some biochar pyrolyzed from contaminated waste may arouse concerns of secondary pollution (Liu, et al., 2018). The effect of diverse properties of biochar on wastewater treatment hasn`t been well studied. Therefore, the commercial application of biochar in wastewater treatment has still not been implemented.

2.2 Biochar properties affecting cement system

2.2.1 Chemical composition of biochar

Application of biochar cement composites in construction materials to generate low-carbon or even carbon-negative construction materials will break new ground to achieve carbon neutrality. Biochar cement composite is a novel composite made of biochar and cement. In this system, cement would provide the binding strength, whereas biochar can serve as internal curing material and provide additional nuclear points to improve cement hydration. However, the diverse properties of biochar would have different effects in the biochar cement system and therefore need to be investigated differently.

Biochar are mainly composed of H, C, N and inorganic elements. Their content are varied depending on the type of feedstock and the production approach. Biochar produced from hazelnut and peanut shells are composed a little defective graphite crystal or amorphous carbon (Yang et al., 2007; Quicker et al., 2016). Typically, biochar containing higher a content of carbon present higher values of hardness and toughness. The pyrolysis temperature was the dominant factor on the hardness and modulus of biochar. It was also mentioned that biochar with aromatic nature and with more ordered carbon molecules exhibited higher values of hardness/modulus (Das et al., 2015). On the contrary, the content of N in biochar reduced with the increasing pyrolysis temperature. And biochar pyrolysis from soft-wood have a higher content of N. In addition, the content of inorganic elements (e.g., K, Ca, Si, Al) of biochar is highly affected by the composition of feedstocks. A higher level of Si and Al can be found in the bark biochar (Vassilev et al., 2010;). Research showed that the biochar pyrolysis from coffee powder contained a high content of K. The K element could act as an alkali activating element and react with cement via a potassium salt reaction. As a result, the hydration was sped up and the mechanical properties of cementitious composites were improved (Gaskin et al., 2008; Onay et al., 2008). Reactive Si, which was proven element that can react with $Ca(OH)_2$ (CH) to form additional calcium-silicate-hydrate (C-S-H) gel to enhance mechanical performance, can be found in the composition of some biochar. For example, rice husk biochar, poultry litter biochar, paper and pulp sludge biochar were characterized with high content of silica and present high pozzolanic activity (Akhtar et al., 2018).

2.2.2 Physical properties of biochar

Other properties of biochar (e.g., pH, porosity, surface area) would also affect the cement hydration and mechanical performance. The biochar with a higher surface area would have a higher contact area with the cementitious materials, which might improve the adhesion between cement and biochar. The particle size distribution of the biochar can significantly affect the flowability and workability of the cement mixture. Studies showed that the microparticle biochar tends to have a higher water absorption capacity than the nanoparticle biochar, which would reduce the effective water to binder ratio of the cement mixture (Wei et al., 2002). The biochar at nanoscale have a higher surface area, which results in a negative effect on the structure of cement based composite. Because more atoms and molecules would be adsorbed on the surface of biochar with higher surface area, which would cause a stronger electrostatic force and Van der Waals force would be generated between the particles and between atoms and thus causing their re-agglomeration (Gupta et al., 2019; Cosentino et al., 2019).

The density of the biochar has an impact on the cement mortar as well. The particle density of biochar is much lower than the OPC and common aggregates, being around 1/2-1/3 of them. This presents the possibility of lightweight composite by incorporating biochar (Brewer et al., 2014). Typically, higher density can be found in the biochar produced from biomass with higher density. Reports showed that the true density of biochar would increase as the production temperature increase due to the shrinkage of the solid matrix while a strong correlation between the particle density and the pyrolysis temperature cannot be found (Pulido-Novicio et al., 2001). The pH of the biochar would significantly affect the cement hydration as too much higher or lower pH would destroy the structure of C-S-H. During the pyrolysis process, the acidic functional groups such as hydroxyl, carboxyl or formyl groups within the feedstock would decompose and regenerate a basic nature in the biochar. The feedstock, pyrolysis conditions and conversion process would have an impact on the pH value of biochar. It has been reported that higher pH value and high concentrations of basic cations could be detected in the softwood biochar. Studies showed that 2–8% incorporation of biochar has little effect on the alkalinity of the cement mixture, which would not affect the cement hydration. In addition, higher ash content could be detected in the biochar from higher pyrolysis temperature due to higher carbonization degree (Messaoudene et al., 2011; Dixit et al., 2019).

The shape of the biochar particle also affected the properties of the cement mixture. The biochar particles were characterized with angular-shaped would reduce the flowability of the cement paste. That biochar with roughness appearance might improve the adhesion between the cement and biochar (Yang et al., 1998; Khushnood et al., 2016). Fibre shape biochar might serve as a bridge between the cement hydrates and the Interfacial Transition Zone (ITZ), causing the stress redistribution and thus the brittle failure could be reduced. The grinding and milling process for the biochar particles could make them angular shapes, which are favorable for aggregate bridging. This specific property can guide the development of the crack to follow a flat fracture path through the aggregates that are not bonded to the cement hydrates (Merchant et al., 2001).

2.3 Incorporation of biochar in different cement-system

2.3.1 Biochar in OPC system

OPC is the most common and reliable cement. The pre-soaked biochar can serve as the internal curing additive to release water during the hydration process to improve the cement hydration degree. Cement hydration is the most important process that affects the cement performance. The cement hydrates include C-S-H, CH and $CaCO_3$ (CC). The C-S-H and CH are the main components responsible for the strength development of OPC system. And the formation of C-S-H is highly associated with cement hydration degree. The anhydrate cement clinkers are retained in nearly every cement system after hydration and they can be further hydrated with sufficient water or incorporation of a micro-filler (Poppe et al., 2005). And the addition of biochar with fine particles can serve as the micro-filler to fill part of the pores. However, the excessive addition of biochar would cause the significantly reduction of mechanical properties due to the introduction of porous and brittle structure of biochar. In addition, the effect of biochar on the improvement of hydration is irrespective of the biomass. Studies have shown that the incorporation of 5% biochar from wood sawdust, increased 30% hydration heat during the 96-h hydration (Gupta et al., 2020a). However, the cumulative hydration heat was found to be reduced by 15% after the introduction of 2% dairy manure biochar. This was because of the high ash content of 84%, containing high concentration of phosphorus, calcium and magnesium, which hindered the cement hydration (Gupta et al., 2020b). On the contrary, the incorporation of biochar with high content of cellulose increased the hydration heat. Interestingly, 9% higher against 9% lower hydration heat was detected in the hydration process after incorporating 2% biochar and bio-mass (sugarcane bagasse). Studies showed that the substitution of 8 wt.% of cement by fine biochar (< 150 μm) could increase the cement hydration degree in ultra-high-performance concrete (UHPC) with low water to binder ratio. The internal relative humidity is the important factor that affects the autogenous shrinkage and cracking of the cement system, especially when external curing is not available. The drying of cementitious materials is mainly composed of two phases. The diffusion of water vapor is the major mechanism to drive the water transfer within the cement system. And the reaction of capillary water also causes the reduction of the internal relative humidity. The biochar incorporation could also maintain the internal relative humidity and make it reduce more slowly to achieve a higher hydration degree, compare to the cement system without biochar. In addition, the fine biochar has a filler effect on the cement hydration that can reduce the setting via improving the effective water to binder ratio (Dixit et al., 2019; Dixit et al., 2021). The new granular materials, especially the small particle size, can provide the nuclear point for the formation of C-

S-H because of their large specific surface area. Studies demonstrated that poultry litter biochar may facilitate the generation of denser structures in the early period (Akhtar et al., 2018).

2.3.2 Biochar in OPC-SCMs system

SCMs are natural materials or industrial by-products, which could be regarded as low-carbon alternatives of OPC. The incorporation of SCMs in the biochar cement composite could further enhance the performance and lower the total CO_2 emission. The SCMs can be classified into two groups according to their composition. The hydraulic materials (e.g., ground granulated blast furnace slag (GGBS)) contain high content of calcium and they can spontaneously hydrate with water to form a binder like cement. On the other hand, the pozzolanic materials (e.g., silica fume (SF), metakaolin (MK)) contain a high concentration of silica or aluminum that can react with CH to generate C-S-H or calcium-aluminium-silicate-hydrate (C-A-S-H). In the section, studies about the common SCMs that have the potential for biochar incorporation by using biochar with SCMs in the cement system were reviewed.

Silica fume is a by-product with an ultrafine particle size collected from silicon and ferrosilicon alloy production (Skibsted et al., 2019). Typically, SF contains high content of reactive SiO_2 (> 80%). The reactive SiO_2 can consume the CH to generate an additional amount of C-S-H. Furthermore, the SF could serve as the role of physical filler in the cement mixture. The SF with ultrafine particle size (around 1/3 of the cement particles) could fill the pores created by evaporation of free water, achieving a denser structure of biochar cement composite and lower leachability of toxic elements (Lapeyre et al., 2018). The 10 wt. % substitution of cement with SF and biochar derived from wood and food waste has been studied. The authors claimed that the incorporation of biochar with SF increased the early strength, compared to the cement and silica fume binder (Gupta et al., 2020c). The pre-soaked biochar could release water continuously to facilitate the reaction degree of the silica fume and cement. And the reactive silica would consume the CH and generate additional amounts of C-S-H to enhance the mechanical properties (Gupta et al., 2020c).

PFA, a by-product produced from power plants, is another common SCMs that has the advantages of less energy consumption and higher cost-effective. It was one of the most promising SCMs to enhance the mechanical properties of the biochar cement composite (Roy et al., 2017b). The incorporation of Pulverized fly ash (PFA) particles with spherical shape could also improve flowability, mechanical strength by the friction rolling, pozzolanic effect and filler effect. The PFAs could be classified into Class-F PFA (low-Ca) and Class-C PFA (high-Ca) based on the Ca content. The Class-F PFA was characterized with high pozzolanic effect similar to silica fume. The incorporation of Class-F PFA can react with CH to generate additional C-S-H through pozzolanic reaction. On the other hand, Class-C PFA could present both pozzolanic and hydraulic effects to enhance the property of the cement mixture. Therefore, PFA could be another potential additive that can be with biochar to enhance the performance of the biochar cement composite.

GGBS is a by-product collect from steel and iron production. The incorporation of GGBS can lower the hydration heat of cement hydration and improve the resistance from chloride and sulphate. As a hydraulic material, it contains high content of calcium and it can spontaneously hydrate with just like OPC (Cheah et al., 2016; Samad et al., 2017). This means that it can replace cement and reduce the CO_2 emission of the biochar cement composite. In addition, GGBS with a small particle size could also serve as filler, achieving a more densify pore structure and improving the physical properties. Thus, the GGBS could be another promising additive to combine with biochar in cement system.

2.3.3 Biochar in Magnesia cement-system

MgO-based cement is another eco-friendly cement with lower CO_2 emissions that can combine with biochar in a sustainable approach. In this section, the mechanisms of the MgO-based cement and the application of biochar enhanced MgO based cement composite are introduced. generated from the calcination of magnesite at approximately 700 °C to 1000 °C (Ruan and Unluer, 2018), which is much lower than the temperature of OPC (1400 °C) (Mo et al., 2016). The recovery of MgO from salt lakes (e.g., $MgCl_2$) is regarded as a cleaner approach for magnesia cement (MC) production (Tan et al., 2016; Walling and Provis, 2016). A recent study further suggests that reject brine can also be a greener source for MgO production (Dong et al., 2018). The compressive strength of the MC was relatively low, and the water resistance was poor, which greatly limited the industrial application of MC. This was because the $Mg(OH)_2$ (MH) has a high solubility in water and weak durability. However, the properties of MC can be significantly enhanced by further carbonation. Upon hydration, MC can generate abundant MH, which could further carbonated by adsorbing CO_2 (Wang et al., 2016). After carbonation, the MH would convert to magnesium carbonates and hydrated magnesium carbonates. In addition, the pore-structure was densified and the mechanical strength was improved due to the formation of thermodynamically stable carbonates (Mo et al., 2016). However, the carbonation would generate on the surface of the MC and hinder the CO_2 diffusion, restricting the carbonation degree of MC.

Ahmad et al. (2020) have investigated the effect of biochar on the mechanical strength of magnesium phosphate cement (MPC). The biochar was pyrolysis from the wheat straw agro-food waste at 650 °C under N_2 atmosphere for 4-h. Results illustrated that the incorporation of biochar could improve the flexural strength and compressive strength of MPC mortars. For example, the addition of 1.5% biochar in samples increased the compressive strength by 17.3%, compared to the plain sample. The improvement mechanism of the mechanical properties could be ascribed to the internal curing effect, filler effect and lower local water to cement ratio with the incorporation biochar. The addition of biochar with fine particles decreased the width of micro-cracks, micropores and capillary pores. Because fine pores were filled by capillary action during the first 6 hours, the coefficient of initial sorptivity was greater than the coefficient of secondary sorptivity. With the inclusion of biochar, the overall sorptivity of MPC was substantially decreased. Besides, the biochar incorporation decreased the permeable porosity and total porosity. When compared to the plain sample, the total volume of air-voids and permeable air-voids with 1.5 % biochar addition was reduced by 30% and 31%, respectively. The scanning electron microscopy (SEM) results showed new products might be formed after the biochar addition, whereas no hydration products could be found from the X-ray diffraction (XRD) and Fourier-transform infrared spectroscopy (FTIR) analysis. Therefore, further chemical analysis on the combination of biochar and the MPC was necessary.

2.4 Different application biochar cement composite

2.4.1 Application of biochar in cement-based stabilization/solidification of wastes

Contaminated wastes are highly associated with agriculture or industrial activities (Trinh et al., 2019; Tombesi et al., 2017). The contaminants including heavy metals, organic matters, chlorides, and sulfates cause severe damages to the environment and human society (Yang et al., 2020). Cement-based S/S is one of the most cost-effective approaches with the advantages of high compatibility to treat various wastes (Wang et al., 2022). Cement-based S/S is a physical and chemical treatment approach for contaminants. Solidification means entrapping the contaminants in the solid matrix and stabilization means complexing/binding the toxic elements into the stable materials (Wang et al., 2022). OPC is one of the most reliable and cost-effective binders for S/S. The cement hydrates including CH, C-S-H can immobilize contaminants by adsorption, fixation and precipitation (Zhang et al., 2021). However, the production of OPC would cause high CO_2 emissions due to the high temperature calcination process at 1450 °C (Lehne et al., 2018). Therefore, developing a low-carbon and high efficiency cement-based S/S method is imperative for the sake of carbon neutrality and a circular economy. Biochar is considered as a reliable stabilizing agent in wastewater treatment with many advantages, including cost-effective, high adsorption capability and high availability of raw material (Shen et al., 2021). In addition, recent studies showed that the biochar incorporation enhances the S/S efficiency of organic pollutants and potentially toxic elements. Besides, the addition of biochar improved the cement hydration but introduce capillary pores and caused strength reduction. As a result, the contaminated sediment was successfully recycled into different sustainable construction products (i.e., fill material and pedestrian/vehicle paving blocks) with the addition of biochar and different green additives (Wang et al., 2019b). However, the contaminated wastes with different toxic elements would cause significantly different changes in the setting, S/S efficiency and mechanical properties of the biochar cement-based composites. Other parameters of wastes, such as the pore size distribution, moisture content and mechanical strength are also important. For example, Wang et al., (2019b) found that the particle size distribution of sediment was the key factor that determined the mechanical strength of the products. And the introduction of silt and clay with micro-pores would cause microcracks and further reduction of the compressive strength. Therefore, the S/S mechanism of various wastes by the biochar cement composites should be further assessed.

2.4.2 Development of different biochar construction products

Cement particleboard is another ideal application for biochar cement composite. Wood cement particleboard has been widely used in noise barriers, ceilings, partition walls, roofs and floors due to the advantages in thermal/noise insulation, lightweight and cost-effective (Karade, 2010). Because the porous structure can effectively break the transformation of heat and noise, biochar also exhibits low thermal conductivity and noise insulation.

Research found that biochar incorporation at the dosage of 4 wt.% can reduce the thermal conductivity of cement-biochar composites by 25%. The biochar cement composite has been found to have outstanding acoustic performance at the range of 200-2000 Hz. Therefore, there is great potential to use biochar to replace wood to develop biochar cement particleboard with multi-functional properties.

Pervious concrete is a porous product that has been widely applied in pavements. The pervious concrete has high water permeability that could facilitate the stormwater run-off, purify water quality and mitigate urban heat island effect. Biochar pervious concrete has been developed by replacing cement with pulverized biochar (Qin et al., 2021). Compare to the conventional pervious concrete, the biochar pervious concrete could achieve comparable porosity and water permeability and higher mechanical performance at relatively low biochar content (< 6 wt.%). Researcher claimed that the filler effect and water adsorption property of biochar contributed to the strength improvement of biochar pervious concrete. Due to the higher surface area of biochar, the biochar pervious concrete was expected to have better water purification and microbial degradation performance. Moreover, Tan et al., reported that the biochar addition could improve the absorption of solar radiation and keep cool through water evaporation (Tan et al., 2021). Therefore, biochar with high porosity could be a value-added material when applied in the right position of construction materials and more application of biochar cement composites should be investigated.

CHAPTER 3. Biochar cement-composite and its application in stabilization/solidification of municipal solid waste incineration fly ash

3.1 Introduction

This chapter presents the roles of rise husk and yard waste biochar in cement system and proposes the application of biochar cement composite for S/S of MSWI fly ash. Incineration is a prevailing and time-efficient technique for municipal solid waste treatment, which can convert waste into heat and electricity and significantly reduce the waste volume by 90% (Wang and Fan, 2020, Zhang et al., 2021). However, municipal solid waste incineration fly ash (MSWIFA) and bottom ash are inevitably generated as by-products after the incineration process (Xue et al., 2021). For instance, the generation of MSWIFA in China exceeds 10 million tonnes in 2020 (NBSC 2020). Different from bottom ash with low toxicity, MSWIFA is categorized as hazardous waste due to its high concentrations of potentially toxic elements (PTEs) (e.g., Cr, As, Pb, Zn), and organic pollutants (Li et al., 2019). Therefore, effective treatment of MSWIFA is essential to control the potential impacts on the environment and human health.

In China, the properly treated MSWIFA could be categorized as general waste or even recyclable resource for further application (HJ 1134), when it satisfies the specific requirements (GB 34330). OPC-based S/S is a prevalent and robust technique for the treatment of MSWIFA (Fan et al., 2018; Wang et al., 2019a; Chen et al., 2019). The hydration products of OPC (e.g., C-S-H and CH) can immobilize the PTEs and organic pollutants via physical encapsulation and chemical stabilization (Sun et al., 2022; Guo et al., 2021). However, most of the PTEs (e.g., Zn and Pb) in MSWIFA would interfere with cement hydration, resulting in lower compressive strength and unsatisfactory immobilization efficiency (Yakubu et al., 2018; Wang et al., 2018a). Moreover, cement production was associated with high carbon emission (Geng et al., 2019). Therefore, faced with the increasing treatment demand of MSWIFA, the development of low-carbon and cost-effective technique is highly important for achieving long-term targets of “zero-waste cities” and “carbon neutrality” (MEE 2020; BBC 2021).

Compared to the limited supply of commonly used supplementary cementitious materials in many countries or regions (Scrivener et al., 2018), the application of biochar as supplementary cementitious materials in the cement system can significantly reduce carbon footprint and make a great contribution to carbon neutrality. Recent studies found that biochar incorporation could improve cement hydration and mechanical performance due to the internal curing effect (Wang et al., 2019b). More importantly, biochar has a mesoporous structure, relatively high surface area, and abundant functional groups, which has a proven adsorption capacity for organic and inorganic contaminants (Gupta et al., 2019). Therefore, biochar is potentially a promising additive in the cement-based binder for the treatment of MSWIFA.

The performance of biochar is highly associated with the feedstock selection and production approaches. Rice husk biochar (RBC) is a Si-rich material that may facilitate the generation of C-S-H through pozzolanic reaction (Ataie et al., 2016; Salem et al., 2018). The yard waste biochar (YBC) is a porous material that has a high water-holding capacity and may provide nucleation sites for hydration products (Gupta et al., 2018b). In this study, it is hypothesized that the incorporation of different biochars may improve cement hydration via different mechanisms, while biochar can also enhance the S/S efficiency of PTEs because of its high adsorption capacity for pollutants in MSWIFA.

In this study, rice husk biochar and yard waste biochar were incorporated in the cement system to improve the cement hydration and S/S efficiency for MSWIFA. This study aimed to: (i) explore the mechanisms of two biochars on the cement hydration, microstructure, and mechanical performance of the biochar cement system; and (ii) unlock the roles of two biochars on the cement-based stabilization/solidification of MSWIFA.

3.2 Materials and methods

3.2.1 Materials

The primary binder used to S/S MSWIFA was CEM I 52.5 N ordinary Portland cement from Green Island cement company in Hong Kong. The rice husk biochar obtained from Shengsheng agriculture company (Guangdong Province, China) was pyrolyzed from rice husk at 500 °C for 1 h with a heating rate of 10 ℃ min^{-1} by using a furnace. The yard waste biochar was produced by pyrolysis of woody yard waste (mainly masson pines) collected from the Ecopark in Hong Kong. The yard waste was shredded into less than 20 mm and oven-dried at 60 °C for 24 h before pyrolysis. Yard waste was pyrolyzed at 750°C for 1 h with a heating rate of 10 °C min^{-1}. The chemical compositions of the raw materials detected by X-ray fluorescence (XRF) are illustrated in Table S3.1. SEM images of two kinds of biochar at different magnifications are shown in Figure S3.1. Biochar served as the internal curing material was sieved to 0.1-1 mm.

Basic information on biochar is presented in Table 3.1. The Brunauer-Emmett-Teller (BET) surface area, average pore diameter and pore volume of the biochar were analyzed by nitrogen adsorption-desorption isotherm measurements (ASAP 2020) using a gas sorption analyzer at -196 °C. The BET surface area of the RBC was less than that of YBC (30.9 m^2 g^{-1} vs. 47.4 m^2 g^{-1}), whilst the total pore volumes of RBC and YBC were 0.02 m^3 g^{-1} and 0.04 m^3 g^{-1}, respectively. Before application, biochar was pre-soaked in deionized water and attained the saturated surface dry (SSD) status by vacuum filtration. It is noted that the water absorption of pre-wetted lightweight aggregate was higher than 5% (ASTM C1761), whereas the water absorption of SSD status RBC and YBC reached 67.8% and 70.8%, respectively, suggesting that they can be applied as internal curing materials due to the remarkable water absorption capacity.

Table 3.1 Basic information of biochar.

	RBC	**YBC**
Surface Area (m^2 g^{-1})	30.89	47.40
Total Pore Volume (cm^3 g^{-1})	0.02	0.04
Average Pore Diameter (nm)	5.54	7.71
Water Absorption Capacity (%)	67.79	70.77

MSWIFA was obtained from a municipal solid waste incineration plant in Shenzhen, China. The waste incinerator burning proceeded at the temperature of 900–1100 °C for 8–10 s. Figure S3.2 shows the particle size distributions of the MSWIFA, which was analyzed by using the laser diffraction analyzer (Malvern Mastersizer 3000E). The MSWIFA contained high concentration of PTEs, such as 997 mg kg^{-1} of Pb, 5467 mg kg^{-1} of Zn, 1424 mg kg^{-1} of Cu, 67 mg kg^{-1} of Cr and 60 mg kg^{-1} of As. After the toxicity characteristic leaching procedure (TCLP) (US EPA, 1992), 18.87 mg L^{-1} of Pb, 2.15 mg L^{-1} of Zn, 1.98 mg L^{-1} of Cu, 2.97 mg L^{-1} of Cr and 0.20 mg L^{-1} As were detected in the MSWIFA leachate by using an inductively coupled plasma atomic emission spectrometry (ICP-OES, Optima 8300, Perkin Elmer).

3.2.2 Sample preparation

The mixture designs of biochar modified pastes and MSWIFA S/S blocks are provided in Table 3.2. For the production of biochar modified pastes, the water-to-cement ratio was adopted at 0.3. RBC and YBC were employed to replace 2%, 5%, and 10% of cement by mass. To investigate the performance of biochar-cement system for S/S of MSWIFA, the biochar-cement binder was mixed with MSWIFA at a mass ratio of 90%, 80%, and 70% to produce MSWIFA S/S blocks. To achieve sufficient workability, the water-to-cement ratio and water-to-MSWIFA ratio were kept at 0.3 and 0.55, respectively. During the production process, all materials were mixed for 5 min to achieve a homogeneous mixture and then poured into 20 mm × 20 mm × 20 mm cubic steel molds. All demolded samples after 1-d hardening were covered with a waterproof membrane and cured at room temperature (23 ± 2 °C) for 7 and 28 days before subsequent analytical tests.

Table 3.2 Mixture design (wt.%) of biochar modified pastes and MSWI fly ash S/S blocks.

(a) Biochar modified paste	Cement	RBC	YBC	MSWI fly ash	Water
Control	100	0	0	0	30.0[a]
RBC-2	98	2	0	0	29.4
RBC-5	95	5	0	0	28.5
RBC-10	90	10	0	0	27.0
YBC-2	98	0	2	0	29.4
YBC-5	95	0	5	0	28.5
YBC-10	90	0	10	0	27.0
(b) MSWI fly ash S/S block					
C-70FA	30	0	0	70	47.5[b]
C-80FA	20	0	0	80	50.0
C-90FA	10	0	0	90	52.5
R-70FA	27	3	0	70	46.6
R-80FA	18	2	0	80	49.4
R-90FA	9	1	0	90	52.2
Y-70FA	27	0	3	70	46.6
Y-80FA	18	0	2	80	49.4
Y-90FA	9	0	1	90	52.2

RBC: SSD rice husk biochar; YBC: SSD yard waste biochar; MSWI fly ash: municipal solid waste incinerator fly ash;

[a]: Water in pastes = cement × 0.3;

---

[b]: Water in MSWI fly ash S/S blocks = cement × 0.3 + MSWI fly ash × 0.55.

3.2.3 Characterization methods

The uniaxial compressive strength of 7-d and 28-d samples was determined by using a mechanical testing machine (Testometric CXM 500-50 KN) at a loading rate of 0.3 MPa s^{-1}(BS EN 12390-3). To halt the cement hydration and remove the free water inside the pores, the crushed samples were immersed in isopropanol for 7 days and then placed in a vacuum glass dryer (with silica gel) to dry for 2 days. After TCLP tests, the concentrations of PTEs in the leachates of S/S samples were identified by using ICP-OES.

Hydration heat of the biochar modified pastes was analyzed by isothermal conduction calorimetry (ICC, Calmetrix I-CAL 4000) for 48 h. The thermal decomposition behavior of the specimens was examined by thermogravimetric analysis (TGA, Rigaku Thermo Plus). Approximately 10 mg of powder sample was placed in a corundum crucible and heated from 40 to 1000 °C in the Ar stripping gas atmosphere. The mineralogy of powder samples was determined by using an X-ray diffractometer (XRD, Smart Lab) with a scanning range (2θ) between 15° and 45°. The analytical grade corundum (Al_2O_3) at the dosage of 20 wt.% was homogeneously mixed with powder samples as the internal standard to calculate the content of the respective phases by using quantitative X-ray diffraction (Q-XRD) analysis with the Rietveld refinement method. The phases, references, and criteria of refinement fitting results for Rietveld refinement in Q-XRD analysis are provided in Table S3.2 and Table S3.3 (Supplementary Information). Note that Q-XRD is regarded as a semi-quantitative analysis in view of the likelihood of methodical error (approximately 5%). The morphology and elemental mapping of the particle samples around 0-1 mm were observed by scanning electron microscopy with energy-dispersive X-ray spectroscopy (SEM-EDX, TESCAN VEGA3) at 20 kV operating voltage. The particle samples were gold-coated for 30 s before SEM analysis. Back scattering electron (BSE) imaging of samples was also conducted. Samples for the BSE analysis were prepared by resin impregnation, grinding with 320, 600, and 1200 grits of papers and polishing with 9 μm, 3 μm, and 0.5 μm grades abrasive agents, respectively.

The structures of the biochar cement pastes were further evaluated by using a 500MHz solid-state magic angle spinning nuclear magnetic resonance spectrometer (MAS NMR, GEOL500). ^{29}Si MAS NMR measurement was conducted on a 99.368 MHz NMR spectrometer using a 7 mm CP/MAS probe. A relaxation delay of 30 s and a rotation rate of 4500 Hz were applied to attain full relaxation of the resonating signal for the fractions of silicate tetrahedra with different connectivity. The deconvolution of the overlapped peaks in the ^{29}Si MAS NMR spectra was run by using the Gaussian model in the software Origin Pro 2021. The pore size distribution of the biochar modified pastes was assessed by using mercury intrusion porosimetry (MIP, Micromeritics Autopore IV). Crushed samples were screened into 2.36–5.00 mm size and Hg was intruded into the voids at the applied pressure from 0.007 MPa to 207 MPa.

3.3 Results and discussion

3.3.1 Effect of biochar on the cement hydration, micro-structure and mechanical strength

Heat evolution curves (Figure 3.1 a&b) illustrate that the addition of biochar increased the cumulative hydration heat per cement during 48-h curing, and the cumulative hydration heat increased with the increasing proportion of biochar. When 10 wt.% cement was replaced by RBC-10 and YBC-10, the cumulative hydration heat increased by 2.78% and 3.04% compared to the control sample. This could be attributed to the larger amount of effective water for cement hydration and the internal curing effect of biochar (Wang et al., 2020b). This result was in agreement with a recent study that porous biochar could store water in its pores and slowly release the water along with curing time (Gupta et al., 2018c). It is worth noting that as the adsorbed water in biochar would release slowly, the improvement of cement hydration by the internal curing effect would be more obvious in the later age. Between RBC and YBC incorporated pastes, there was no significant difference in the hydration heat. Although the RBC has pozzolanic reactivity, the pozzolanic reaction occurs at the later stage of cement hydration. Therefore, the similar water absorption capacity of RBC and YBC (67.8% vs. 70.8%) resulted in a similar hydration process of the biochar modified pastes. The curves of the hydration heat rate (Figure 3.1c&d) show that the slope increased with increasing biochar incorporation, which indicated that a high proportion of tricalcium silicate (C_3S) was transformed into C-S-H and CH during the acceleratory period. Moreover, the incorporation of biochar significantly increased the heat release in the initial reaction period before 30 min (Figure 3.1c&d). This was associated with the faster dissolution of cement particles and hydration of tricalcium aluminate (C_3A) in the biochar modified pastes. Therefore, biochar could serve a supplementary binder for improving the cement hydration process.

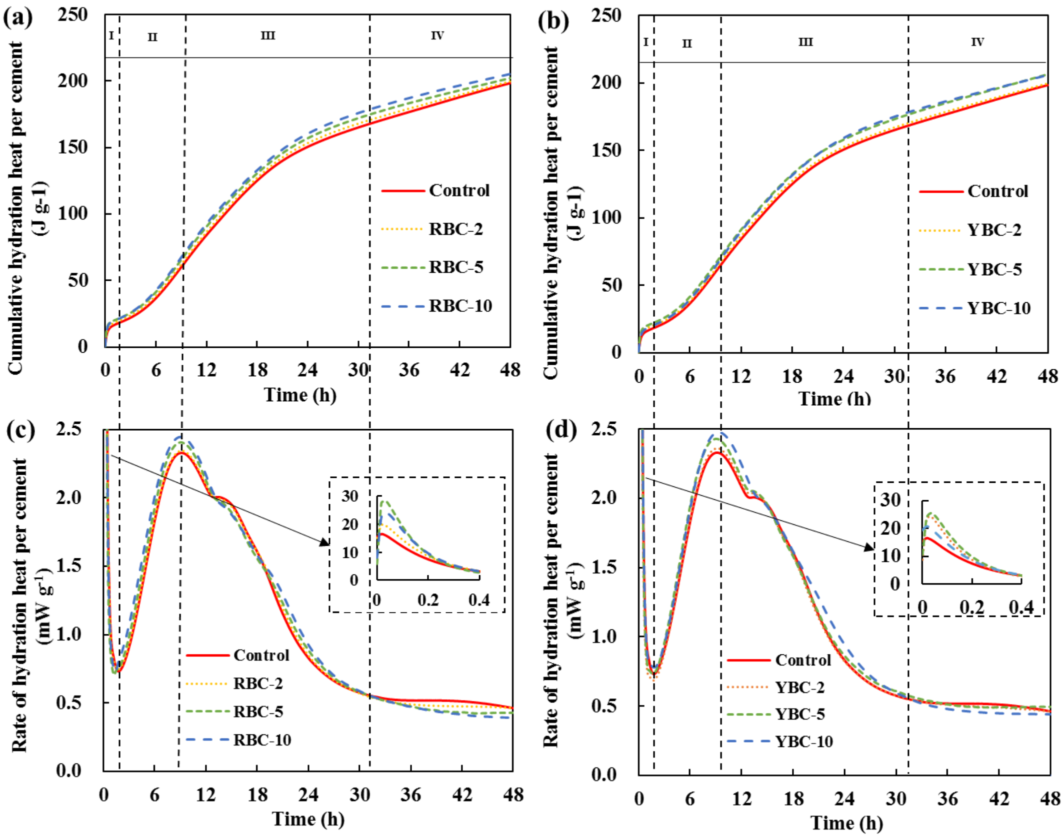

Figure 3.1. Isothermal conduction calorimetry results of pastes with/without biochar (a) & (b) cumulative hydration heat per cement; (c) & (d) rate of hydration heat per cement (Stage I: initial period; Sage II: acceleration period; Stage III: deceleration period; Stage IV: slow reaction period).

The DTG curves of 28-d biochar modified pastes (Figure 3.2a&b) indicate that the replacement of 10 wt.% biochar significantly increased the hydration degree of cement. The DTG curves of the control sample showed remarkable decomposition peaks of C-S-H gel (30–200 °C), CH (380–450 °C), and CC (480–700 °C). The incorporation of biochar promoted the formation of C-S-H and CH, which were the major cement hydration products. The additional peaks at approximately 600 ℃ and 900 ℃ in the biochar modified pastes were due to the decomposition of refractory organic-C (poly-condensed forms of lipids and aromatic-C) and inorganic-C in biochar, respectively (Leng et al., 2019).The mass loss corresponding to the dehydration of C-S-H and CH increased with the increasing proportion of biochar replacement (Figure 3.2c). With 10 wt.% YBC replacement, the mass loss due to the CH dehydration increased from 3.12 wt.% (equivalent to 12.8 wt.% CH) to 3.77 wt.% (equivalent to 15.5 wt.% CH). For the 10 wt.% RBC replacement, the mass loss corresponding to the CH dehydration only increased to 3.36 wt.% (equivalent to 13.8 wt.% CH). Compared to the control sample, the mass loss from the dehydration of C-S-H in the RBC-10 sample significantly increased by 30.4% while the YBC-10 sample only increased by 17.0 %. The RBC incorporated sample generated less content of CH but more content of C-S-H than the YBC incorporated sample (with higher water absorption capacity), which indicated that abundant activated-Si in RBC reacted with part of CH to generate C-S-H via pozzolanic reaction. More importantly, the additional generation of C-S-H compensated for the decrease of 10 wt.% cement. These results confirmed that the biochar incorporation could facilitate the cement hydration due to the internal curing effect, and in particular, the cement substitution by RBC could significantly promote the generation of additional C-S-H via pozzolanic reaction.

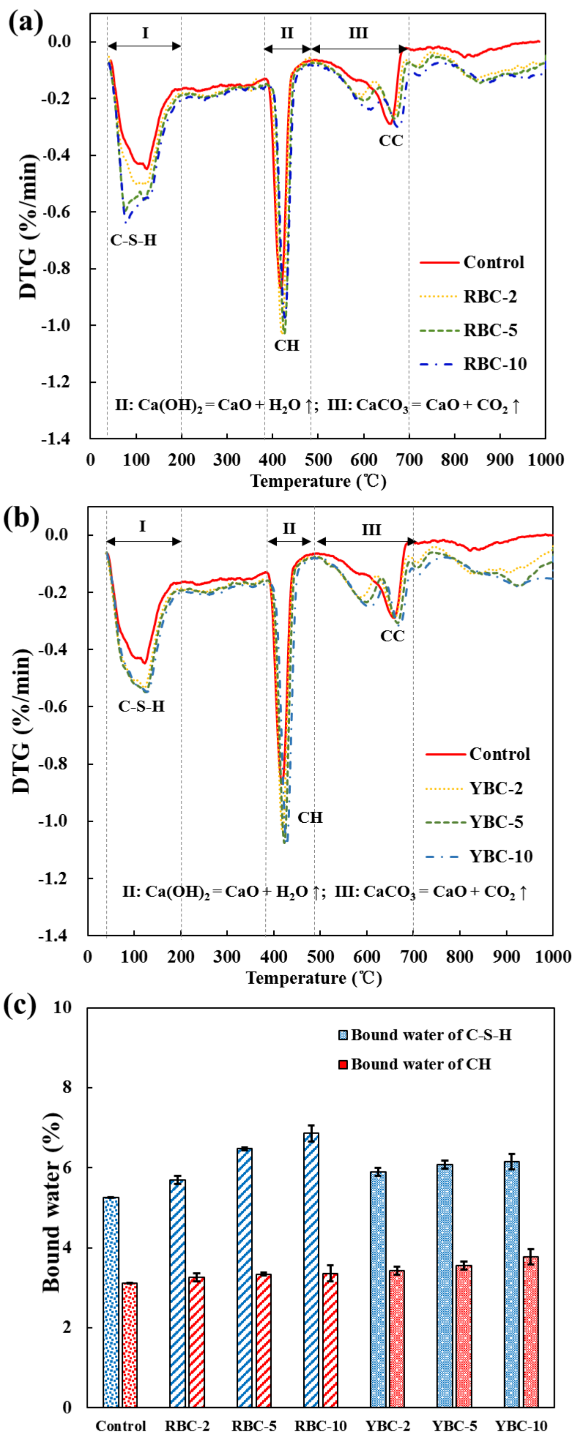

Figure 3.2. (a) & (b) DTG curves of the 28-d pastes with/without biochar and (c) corresponding bound water of C-S-H and CH (Peak I: dehydration of C-S-H; Peak II: dehydroxylation of CH; Peak III: decarbonation of CC).

The XRD diffractograms (Figure 3.3a&b) showed that no new phase was introduced when RBC and YBC were used to partially replace cement. The goodness of fit for Q-

XRD analysis (Table S3.3) suggested that the fitting results were reliable. The Q-XRD results (Figure 3.3c) showed a gradual decrease of clinker content (C_3S and dicalcium silicate (C_2S)) by increasing the proportion of biochar substitution, compared to the control sample. It is noted that the amorphous phases in Q-XRD included C-S-H and biochar. The calculated C-S-H content (Figure 3.3d) in the dried sample (without free water) was obtained by subtracting the amount of biochar from the total amount of amorphous phases (Table S3.4). As shown in Figure 3.3d, the increasing substitution of biochar gradually increased the content of C-S-H, which was in line with the above discussion. Especially for the RBC, 10 wt.% replacement of RBC significantly increased the C-S-H content from 41.6 wt.% (control sample) to 52.0 wt.%. The increase in the formation of C-S-H in YBC-10 sample was slightly less (49.5 wt.% C-S-H), because YBC only provided an internal curing effect during the hydration process. Therefore, comparing the two selected biochar, RBC-incorporated samples could provide a higher C-S-H content and possibly dense microstructure.

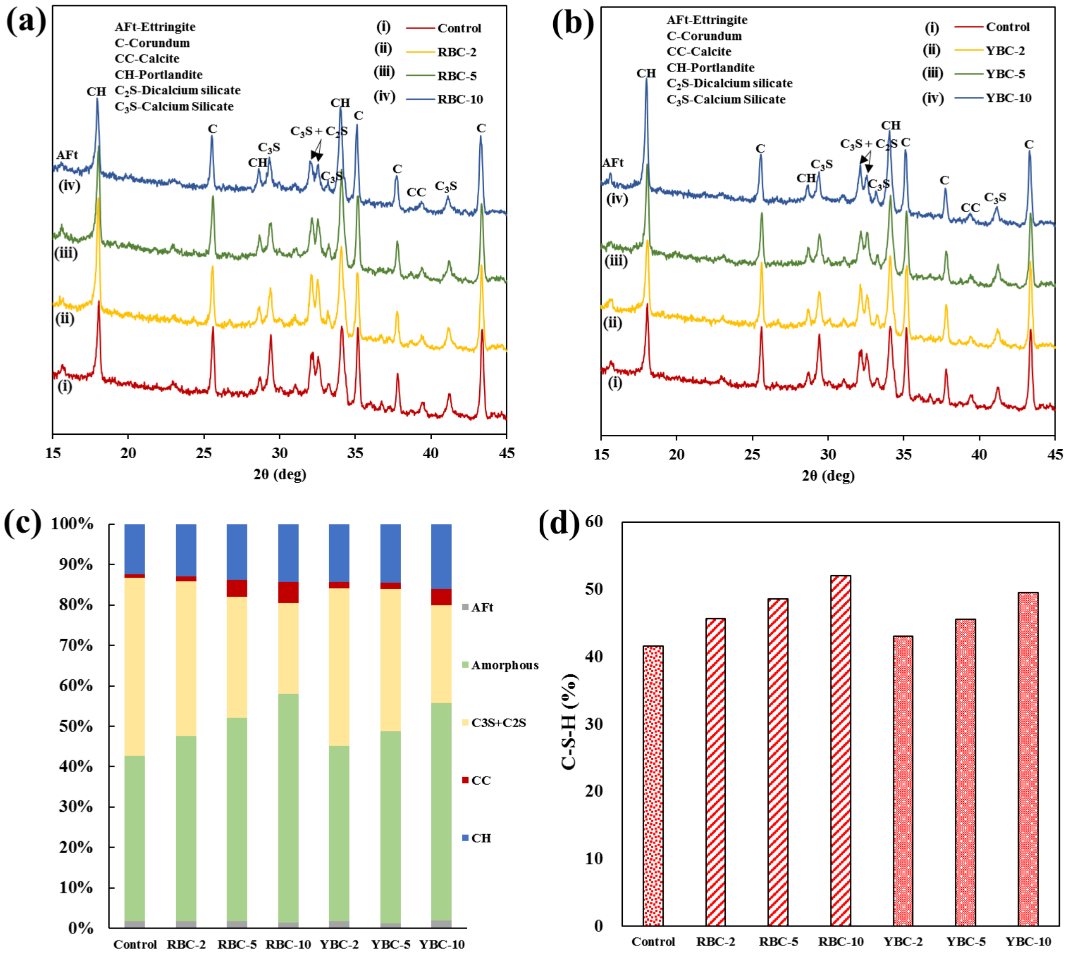

Figure 3.3. Results of analytical investigation of the 28-d pastes with/without biochar: (a) & (b) XRD patterns; (c) Q-XRD analysis; (d) C-S-H content calculation from Q-XRD analysis.

The ^{29}Si MAS NMR analysis (Figure 3.4) illustrates that incorporation of both RBC and YBC increased the proportion of C-S-H. The ^{29}Si NMR spectrum of OPC (Figure S3.4) presents a major peak at chemical shift of 71.8 ppm, corresponding to the Q^0 site. The chemical shift peaks and corresponding numbers indicate the silicate polymerization types of Q^n and its relative integral areas (%). Q^0 (isolated connectivity) represents the unreacted cement clinker including C_3S and C_2S (Jeong et al., 2018). After 28-d curing, the spectrum of control sample exhibited two resolvable peaks at chemical shifts of –79.4 and –84.5 ppm, corresponding to the Q^1 (end-chain groups) in the C-S-H, and the bridging sites Q^2 (middle-chain groups) of the silicate chains (Wang and pang, 2019). The replacement of 10 wt.% RBC and YBC reduced the fraction of Q^0 (by 14.1% in RBC-10 and 10.0% in YBC-10) but increased the integral areas of Q^1 (by 6.3% in RBC-10 and 6.4% in YBC-10) and Q^2 (by 4.9% in RBC-10 and 3.6% in YBC-10). These results further proved that the replacement of biochar enhanced cement hydration. The silicate polymerization in the biochar modified pastes can be represented by the average degree of connectivity (D_c) as shown in equation (1). The higher value of D_c indicates the higher polymerization degree of C-S-H (Moon et al., 2016; Saout et al., 2006).

$$D_c = \frac{Q^1+2Q^2+3Q^3}{Q^1+Q^2+Q^3} \qquad (1)$$

The D_c value of the control sample was 1.43 and the RBC incorporation increased to 1.52 D_c value. Approximately 2.9% Q^3 level of polymerization was detected in RBC-10, indicating the existence of the denser and stronger C-S-H structure, as Q^3 is a cross-linking group in tobermorite like C-S-H (Krakowiak et al., 2015; Jeong et al., 2018). These results indicated that the incorporation of 10 wt.% RBC and YBC could facilitate the generation of C-S-H.

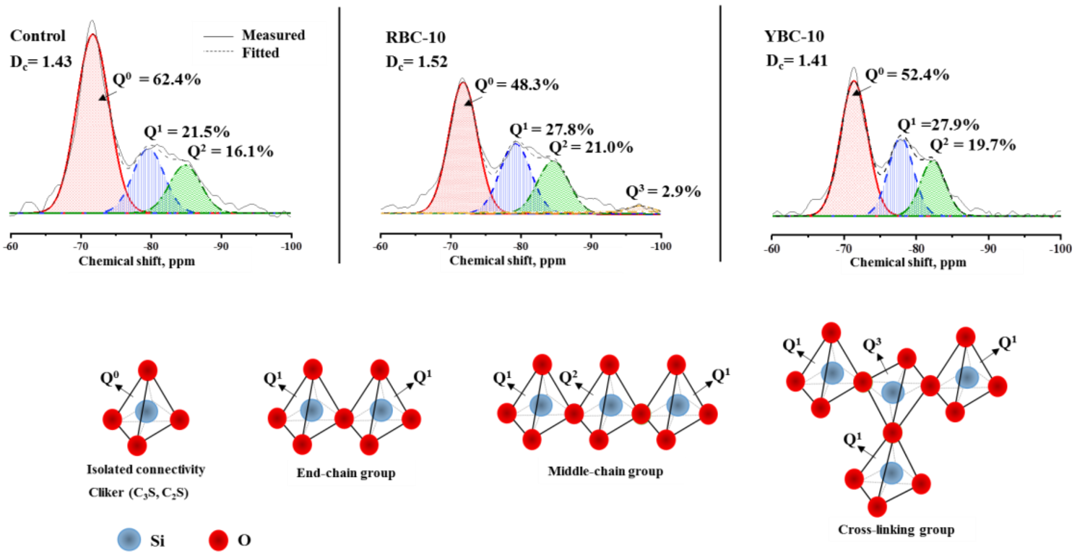

Figure 3.4. ^{29}Si NMR spectra for the 28-d pastes with/without biochar.

The BSE/SEM images illustrate that the biochar incorporation might introduce pores although cement hydration could be improved. As shown in Figure 3.5a, the bright grey area represented the unreacted clinkers including C_3S and C_2S, whereas the dark grey area was composed of Ca and Si, representing the C-S-H phase. It is generally believed that the square shape of unreacted clinkers is C_3S and the more rounded shape is C_2S. In the 28-d control sample, a high proportion of unreacted clinker (mainly C_2S) was observed because of the incomplete hydration, which corresponded to the 44.9 wt.% unreacted clinker content (C_3S and C_2S) by Q-XRD analysis. The 10 wt.% RBC replacement significantly reduced the unreacted clinker area, whereas increased the C-S-H area, which also corresponded to the low content of unreacted clinker (C_3S and C_2S) in the RBC-10 sample as indicated by Q-XRD analysis. Interestingly, favorable hydration and denser surface could be observed surrounding the biochar. This suggested that the water release from biochar could promote the hydration reaction of nearby cement particles. However, small pores in the cement matrix and relatively large pores in biochar were introduced, which would adversely affect the mechanical strength of the biochar modified pastes. The SEM images of biochar modified pastes (Figure 3.5b) shows that biochar and cement were blended and some of the pores were filled by the hydration products. The elemental mapping (Figure 3.5c&d) verified that the hydration products were composed of Ca and Si in the biochar pores, which might mitigate the negative effect of the introduction of porous biochar.

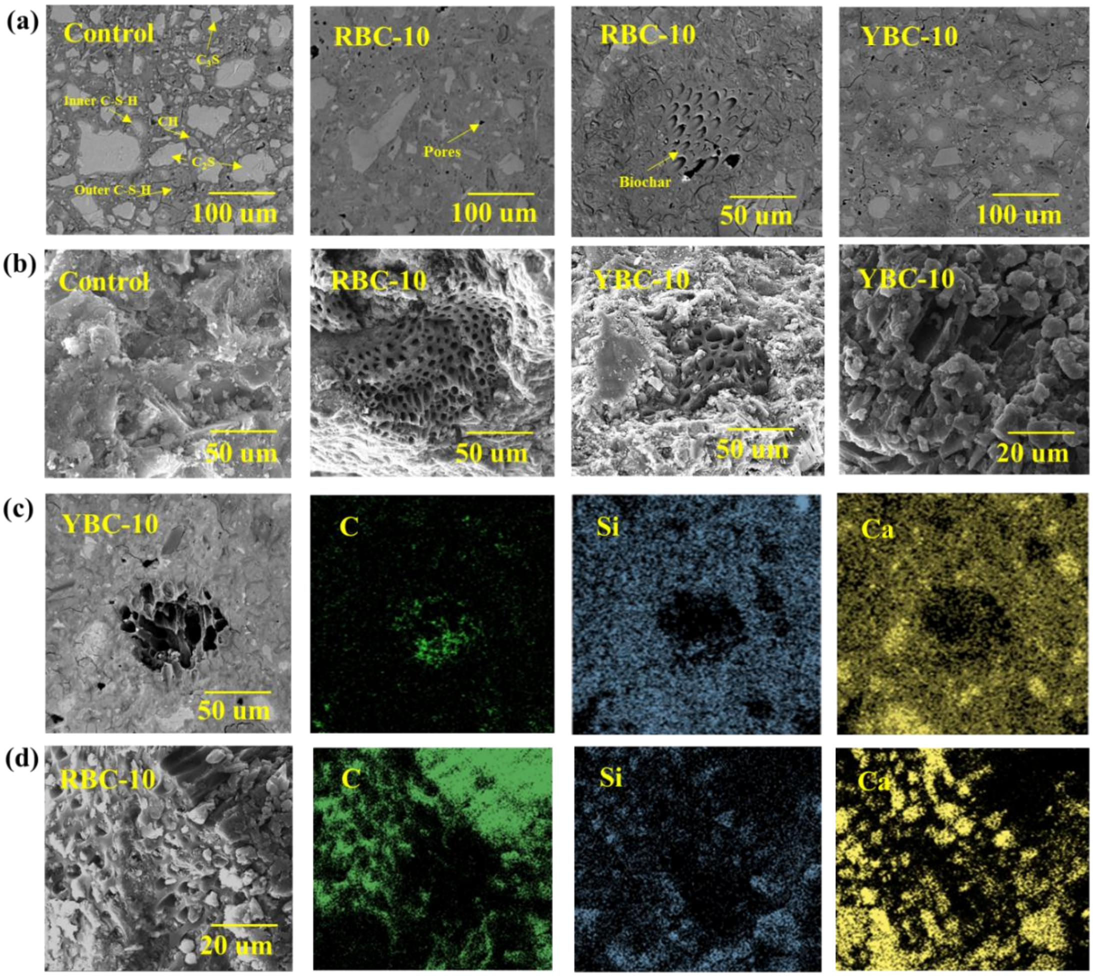

Figure 3.5. BSE/SEM images and elemental mapping of 28-d pastes with/without biochar: (a) BSE images; (b) SEM images; (c) elemental mapping of YBC-10; (d) elemental mapping of RBC-10.

The MIP results (Figure S3.5a&b) indicate that the incorporation of biochar slightly increased the cumulative pore volume. The pore structure plays an important role in the mechanical properties of cement-based materials. Biochar incorporation shifted the major peak of pore diameter from 91 nm to 66 nm, but the RBC-2 sample (Figure S3.5a) showed a comparable cumulative intrusion volume (0.0908 mL g^{-1}) to that of the control sample (0.0914 mL g^{-1}). This indicate that the additional cement hydration products partially filled the original pores ~91 nm in the cement paste. With the substitution of 10 wt.% OPC by RBC and YBC, the cumulative intrusion volume increased from 0.0908 mL g^{-1} to 0.0969 mL g^{-1} and 0.1022 mL g^{-1}, respectively, which was attributed to the introduction of biochar pores. The capillary pores are often responsible for triggering the growth and spread of micro-crack. More importantly, compared with 18.2% porosity in the control sample (Table S3.5), the incorporation of 10 wt.% YBC (with larger amount of pores) slightly increased the porosity to 19.0%, whereas the incorporation of 10 wt.% RBC (with pozzolanic reactivity but less amount of pores) contrastingly decreased the porosity to 17.7%, which may result in the differences in mechanical strength.

Compressive strength results (Figure 3.6) show that 2 wt.% biochar replacement increased the 7-d and 28-d strength of pastes, whereas 5 wt.% and 10 wt.% biochar replacement had a minor negative effect. Compared to the control sample, the improvement of 28-d compressive strength in the RBC-2 sample (increased by 11.0%) was more significant than that of the YBC-2 sample (increased by 4.1%). This was because both samples with biochar incorporation facilitated a higher degree of cement hydration and there was additional C-S-H generation via pozzolanic reaction and higher polymerization degree in RBC incorporated sample, which were in good agreement with the above discussion based on the results from TGA, Q-XRD and NMR analyses. Compared to the control sample, the incorporation of 5 wt.% and 10 wt.% RBC reduced the 28-d compressive strengths by 6.7% and 16.1%, while YBC reduced the strength by 10.8% and 17.3%, respectively. The decrease in compressive strength was mainly ascribed to the increased amount of capillary pores as evidenced by MIP and the brittle nature of biochar. It is noted that the strength of RBC samples was higher than that of YBC samples due to the higher polymerization degree of C-S-H. Hence, it is important to select a biochar with more suitable physicochemical properties and balance the strength improvement or reduction with the environmental advantages of increasing biochar dosage. Considering the satisfactory strength, high carbon sequestration and contaminant adsorption properties, the cement binder with 10 wt.% biochar was adopted for the S/S of MSWIFA.

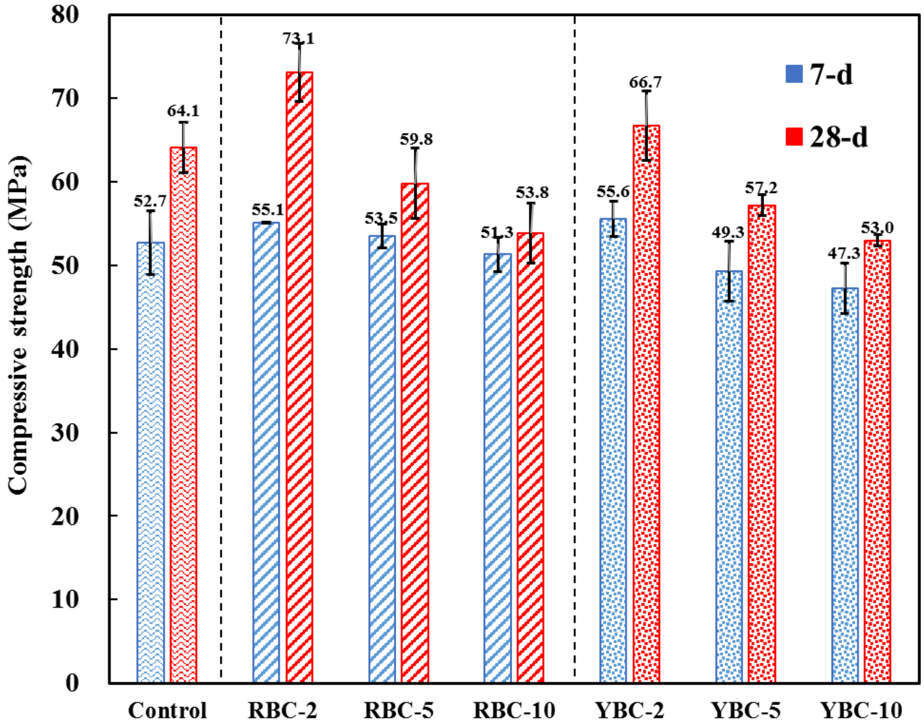

Figure 3.6. Compressive strength of 7-d and 28-d pastes with/without biochar.

3.3.2 Biochar cement composite for stabilization/solidification of MSWI FA

The DTG curves (Figure 3.7a) indicate that the incorporation of biochar improved the hydration of MSWIFA S/S products. With 70 wt.% MSWIFA incorporation, the peak of CH could not be detected, because PTEs in MSWIFA significantly hindered the cement hydration. The largest peak corresponded to the decarbonization of $CaCO_3$ originally contained in the MSWIFA. Due to the variation of PTEs concentrations and the strict environmental standards for the flue gas emissions of incineration, excessive lime solution is often sprayed in the air pollution control system to neutralize acid gases such as SO_x and HCl (Chen et al., 2021). A large content of $Ca(OH)_2$ was naturally transformed into $CaCO_3$ in the MSWIFA in the CO_2-rich atmosphere. The mass loss after 800°C corresponded to the evaporation of low-boiling point salts originally from the MSWIFA. The dehydration peak of C-S-H slightly increased after biochar incorporation, corroborating that the presence of biochar improved the cement hydration. Moreover, a small peak of CH (18.1°, Table S3.2) was observed in the XRD pattern (Figure 3.7b). Compared to the C-70FA and R-70FA samples, slightly stronger peaks of CH and CC were found in the YBC incorporated sampled probably because YBC had larger pore volume and water holding capacity, which was consistent with the TGA results of the biochar modified pastes (Fig 2).

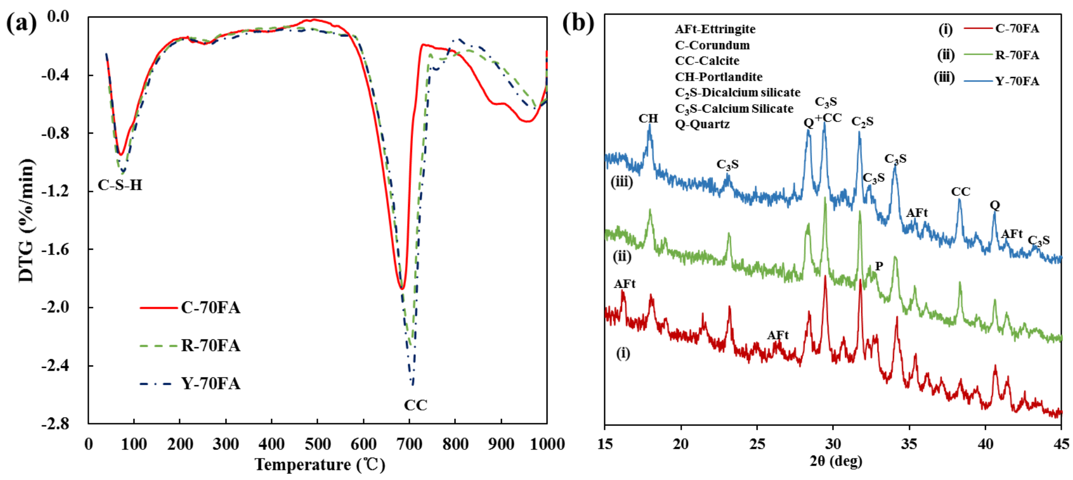

Figure 3.7. Results of analytical investigation of the 28-d MSWI fly ash S/S blocks: (a) DTG curves; (b) XRD patterns.

The SEM images (Figure 3.8) show that MSWIFA S/S samples (90 wt.% MSWIFA) were relatively loose and heterogeneous, compared to the images of paste samples without MSWIFA (Figure 3.5), due to insufficient cement hydration products in the MSWIFA S/S samples. No remarkable difference was observed from the SEM images among the MSWIFA S/S samples with or without biochar (1 wt.%), while biochar particle attaching with MSWIFA particle was observed in the R-90FA sample (Figure 3.8b). The EDX analysis and elemental mapping show that there was a positive correlation between C (57.1 wt.%) and O (29.2 wt.%), Si (1.25 wt.%), Ca (10.8 wt.%), and Pb (1.66 wt.%) on the surface.

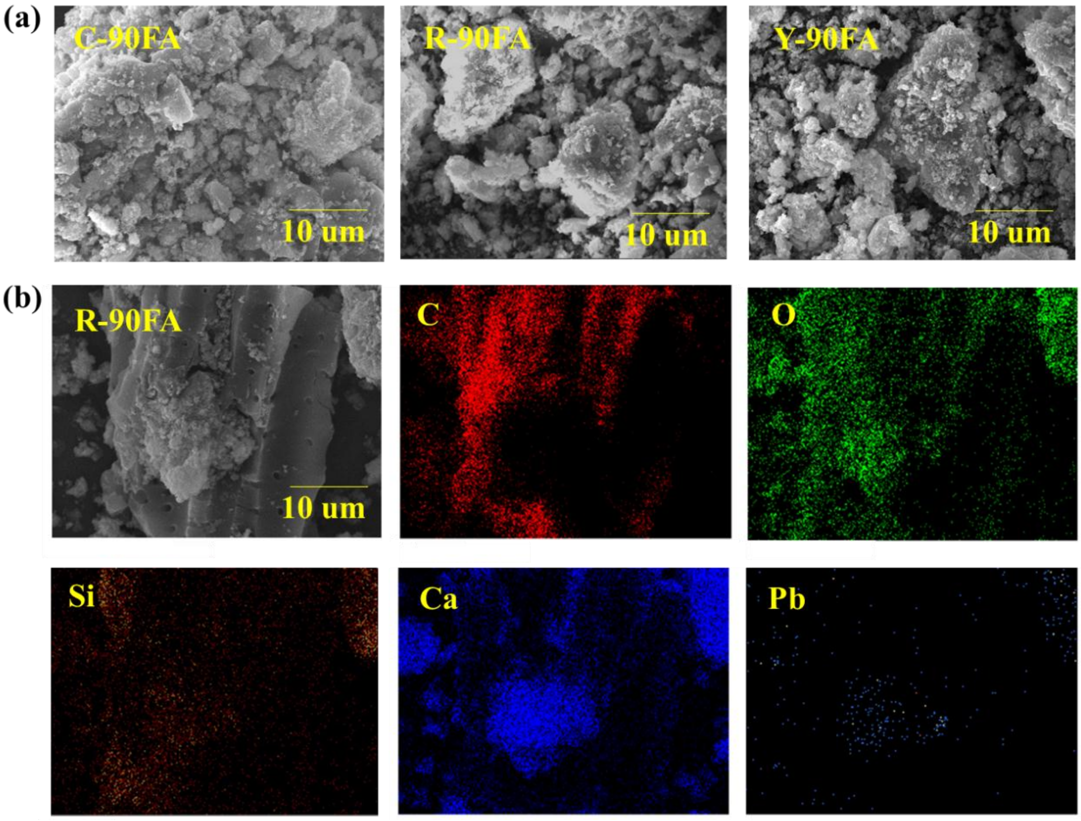

Figure 3.8. SEM images and elemental mapping of 28-d MSWI fly ash S/S blocks: (a) SEM images; (b) elemental mapping of R-90FA.

The results of TCLP leachability (Figure 3.9a) confirm that the incorporation of biochar enhanced the immobilization efficiency of PTEs in MSWIFA. The TCLP leachability of Pb (18.9 mg L^{-1}) in untreated MSWIFA exceeded the leachability limit of MSWIFA for on-site reuse (0.75 mg L^{-1}) (HK EPD, 2011). With 10 wt.% and 20 wt.% binder treatment, the Pb leachability significantly decreased to 4.75 mg L^{-1} (i.e., 74.8% immobilization) and 0.83 mg L^{-1} (95.6% immobilization), respectively. All the PTEs leachability including Pb, Cr, Cu, Zn, and As of the biochar-enhanced S/S samples met the criteria with the use of 30 wt.% binder. Such immobilization performance could be attributed to the physical encapsulation of PTEs in abundant cement hydrates and dense matrix, as well as chemical immobilization via the generation of precipitates (e.g., PbO, $Pb(OH)_2$ and $Pb_2O(OH)_2$) under an alkaline environment (Wang et al., 2018b). The biochar incorporation further reduced the leachability of PTEs owing to abundant hydration products and high adsorption ability of biochar. In R-80FA and Y-80FA samples (namely, 20 wt.% binder dosage, in which RBC or YBC accounted for 10 wt.% of binder), the Pb leaching was further reduced from 0.83 mg L^{-1} to 0.74 mg L^{-1} and 0.71 mg L^{-1} (complying with the criteria of 0.75 mg L^{-1}), respectively. The biochar incorporated binder also showed higher efficiencies than the plain cement binder for immobilizing the other PTEs such as Cr, Cu, and Zn, especially for the case with a lower binder dosage. Therefore, the addition of biochar in cement binder could enhance the immobilization efficiency of PTEs in the MSWIFA S/S process.

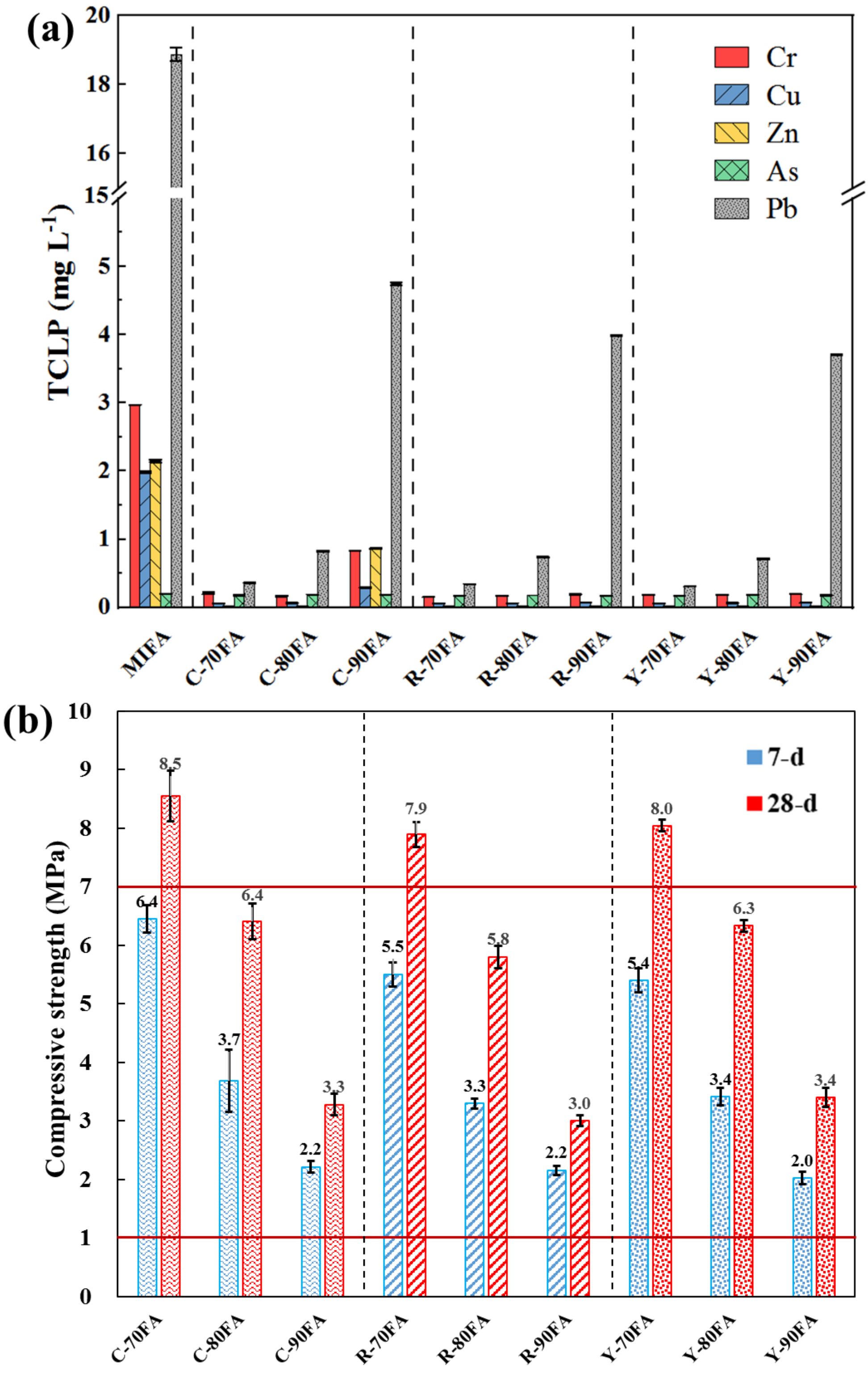

Figure 3.9. (a) TCLP leachability and (b) compressive strength of MSWI fly ash S/S blocks (Leachability limits of trace elements: 0.6 mg L^{-1} of Cr, 0.2 mg L^{-1} of Cu, 4.3 mg L^{-1} Zn, 5 mg L^{-1} of As, 0.75 mg L^{-1} of Pb; red line at 1 MPa: minimum required strength for fill materials; red line at 7 MPa: minimum required strength for partition blocks).

As shown in Figure 3.9b, biochar-modified MSWIFA S/S blocks presented comparable strength to the cement MSWIFA S/S blocks. The mechanical strength of MSWIFA S/S samples decreased with an increase in the MSWIFA dosage. With the incorporation of 10–30 wt.% binder, all the compressive strength fulfilled the strength requirement (1 MPa) of S/S products for on-site reuse (HK EPD, 2011). The MSWIFA S/S blocks with 30 wt.% binder achieved 7.9–8.5 MPa, which can also be applied as non-load-bearing blocks (7 MPa) (BS EN 771-3). The compressive strength was associated with the contents of cement hydrates and microstructures of S/S matrixes. The YBC and RBC-modified samples showed similar compressive strength regardless of the binder dosage, possibly because the advantage of pozzolanic reaction in RBC could not fully exploit due to complexation by the PTEs in MSWIFA.

3.4. Conclusions

This study assessed the distinctive roles of rice husk-derived and yard waste-derived biochar in cement system and evaluated the effects of biochar on the S/S of MSWIFA. Experimental results indicated that the incorporation of biochar facilitated the cement hydration and promoted the formation of hydration products, due to the internal curing effect of biochar. Comparing the two types of biochars, RBC was more effective for promoting the generation of C-S-H than YBC, because activated-Si in RBC could react with CH to form additional C-S-H via pozzolanic reaction. The 2 wt.% biochar addition enhanced the compressive strength, whereas the addition of 5 wt.% and 10 wt.% biochar slightly decreased the compressive strength due to the high porosity of biochar, especially for more porous YBC. The S/S process of MSWIFA confirmed that both RBC and YBC addition improved the immobilization of PTEs in MSWIFA. The 20 or 30 wt.% biochar-enhanced binders could effectively stabilize/solidify MSWIFA, and S/S products fulfilled the requirements for reuse as fill material or non-load-bearing block, respectively. In summary, this research demonstrated that biochar could be a promising additive for S/S of MSWIFA and reduction of carbon footprint. In future studies, the effects of biochar with different characteristics on different cement binders for S/S of MSWIFA should be further investigated. The durability (long-time strength degradation, leachability of PTEs, chloride permeability, etc.) of S/S products should be assessed before practical applications.

CHAPTER 4. Roles of biochar in sustainable magnesia cement- based composites under air curing and CO_2 curing

4.1 Introduction

Gasification is a field-scale approach of biochar production (Dissanayake et al., 2020).CO_2 gasification is an advanced and green technology that can further increase carbon utilization and generate CO_2 gasification biochar with a relatively high surface area and favorable pore structure (Shen et al., 2019). To further reduce the carbon footprint, gasification biochar will be incorporated into low-carbon magnesia cement (MC) in this study. MC is an alternative cementitious material that is produced from calcination of magnesite or the mixture of dolomite and serpentine tailings at a relatively low temperature (Mo et al., 2012; Cao et al., 2021), and the recovery of MgO from brine water (e.g., $MgCl_2$) can be a greener approach for the MC production (Dong et al., 2018). Compared to the OPC system, MC requires more water for the hydration process (Guo et al., 2020; Hay et al., 2020). Therefore, pre-wet biochar could be an additive with slow water release to promote the MC reaction.

In addition, CO_2 curing (i.e., accelerated carbonation) could further reduce the global warming potential of MC composites, because the major hydration product (i.e., $Mg(OH)_2$) of MC can be further transformed into stable magnesium carbonate ($MgCO_3$) and hydrated magnesium carbonates (HMCs) (Al-Tabbaa et al., 2013; Walling et al., 2016; Zhang et al., 2020). Our latest study showed that the carbonation degree of MC after 7-day CO_2 curing (10% CO_2) was comparable to the value of MC after 1-day CO_2 curing (100% CO_2) (Wang et al., 2020c). The carbonation products could densify the pore structure, enhancing the mechanical strength and durability of MC-based composites (Lu et al., 2018; Shi et al., 2018). However, the carbonation products newly formed during CO_2 curing may cover the uncarbonated zone and hinder the CO_2 diffusion and further carbonation of cement particles situated further in the interior, possibly restricting the carbonation efficiency of MC-based composites (Bertos et al., 2004). We hypothesize that the incorporation of biochar in MC system may be a promising method to accelerate the carbonation process, because mesoporous biochar may provide pores and channels for CO_2 diffusion. In return, the subsequently formed carbonates may fill in the air pores of biochar and strengthen the interfacial bonding in biochar-incorporated composites (Zhan et al., 2020). Therefore, this study proposes innovative designs of green composites that integrate carbon-negative biochar with low-carbon MC and CO_2 curing, and accordingly elucidates the roles of biochar in hydration reaction and microstructure development.

Gasification biochar was introduced to promote the hydration and accelerated carbonation of MC-based composites. This research aims to: (i) elucidate the mechanisms of biochar with different properties in changing the hydration progress, microstructure, and mechanical strength of the MC-based composites, and (ii) unravel the interplay between biochar and CO_2 curing for the accelerated carbonation of MC-based composites.

4.2 Materials and methods

4.2.1 Materials

Two types of cement were used as primary cementitious materials in this study, namely MC and OPC. The MC was purchased from Renheng Magnesium Company, Liaoning Province, China, whereas OPC was CEM I 52.5 N ordinary Portland cement, obtained from Green Island Cement Limited, Hong Kong. MC and OPC had a comparable particle size distribution between 45 μm to 80 μm. MC was composed of 90.5% MgO, 5.80% SiO_2, and 2.20% CaO, while OPC consisted of 65.7% CaO, 19.0% SiO_2, and 4.79% Al_2O_3 (Table S4.1, Supplementary Information).

Two types of gasification biochar were used as additives in cement-based pastes. *Pinus massoniana* (masson pine softwood) from a sawmill was used as the sole feedstock for the two types of biochar. Air gasification biochar (Air BC) is one biochar that was produced in a pilot-scale autothermal gasifier with 100% air atmosphere, whereas CO_2 gasification biochar (CO_2 BC) was produced in the gasifier with 85% air and 15% CO_2 atmosphere. The BET surface area of the CO_2 BC was larger than that of Air BC (358 $m^2 \cdot g^{-1}$ vs 326 $m^2 \cdot g^{-1}$). The Air BC contained 72.4% carbon and the CO_2 BC contained 74.3% carbon. The detailed information of the biochar is presented in Table 4.1. Biochar was sieved to fine particles with a size between 45 μm to 80 μm, which was similar to the particle size of MC and OPC. Biochar was pre-soaked in hot water for 30 min and separated by vacuum filtration to attain the SSD status before subsequent use as an internal curing material.

Table 4.1 Basic information of air and CO_2 gasification biochar.

	Surface	Pore	Water	Elemental analysis (wt.%)

	Area $(m^2 g^{-1})$	volume $(cm^3 g^{-1})$	Adsorption rate (%)	C	H	Ca	Fe	Mg	Na	P	K
Air BC	326	0.047	135	72.37	0.64	3.54	0.04	1.23	0.41	0.25	4.91
CO_2 BC	358	0.051	143	74.33	0.51	2.94	0.03	1.01	0.53	0.19	5.43

Air BC: biochar gasification with 100% air atmosphere; CO_2 BC: biochar gasification with 85% air and 15% CO_2 atmosphere; Pore volume: BJH Adsorption cumulative volume of pores between 1.7 nm and 300 nm diameter.

4.2.2 Sample preparation

The mixture formations of biochar-incorporated pastes are shown in Table S4.2. The biochar was employed to replace 2 wt.% of cement based on our previous study (Wang et al., 2020b). The water-to-cement ratio was kept at 0.24 to achieve zero slump paste mixture, which was feasible for block production and CO_2 curing. For block manufacture, cement and pre-wetted biochar were dry mixed for 2 min by a planetary mixer, and then water was added into the dry mixture for another 3 min mixing. For each sample, 280 g fresh mixture was filled into a cylinder steel mold (55 mm diameter) and then was compressed to 55 mm height with 70 MPa pressure for 0.5 min by using Forney Testing Machine. The samples were demolded immediately and transferred to air curing chamber or CO_2 curing chamber. By applying the dry mix and pressure molding method, the fresh samples could be demolded immediately. Then, the OPC and MC samples would have a significant hydration reaction within first 24-h and could adsorb relatively more CO_2. The air cured samples were sealed by plastic membranes to maintain moisture and storage at 23 ± 1 °C chamber for 7-d or 28-d before subsequent analyses. Eight samples for CO_2 curing were placed in a 33 L curing chamber with 100% CO_2 at 1.1 bar atmosphere pressure. To prevent excessive moisture release into the CO_2 curing chamber during the carbonation process that would otherwise impede CO_2 diffusion, approximately 350 g of silica gel was placed in the CO_2 curing chamber to keep constant humidity of 85% ± 5%. After 1-d CO_2

curing, four samples were tested directly and the other four samples were transferred to air curing chamber for additional 6-d air curing. For quality assurance, all the samples were made in quadruplicate.

4.2.3 Characterization methods

The surface area and pore volume of the biochar were measured by nitrogen adsorption-desorption isotherm measurements (ASAP 2020) using a gas sorption analyzer at −196 °C. The uniaxial compressive strength of the blocks was measured by means of standard testing equipment (Testometric CXM 500-50 kN) at a loading rate of 0.6 MPa s^{-1} (BS EN 12390). Statistical analysis of compressive strength results was conducted by using one-way analysis of variance (ANOVA, Fisher's Least Significant Difference test, $p < 0.05$). The letters (a-f) denote statistically significant differences of the experimental results. To indicate the carbonation fronts, the surface of freshly fractured samples were sprayed with phenolphthalein.

For quality assurance, all the samples were crushed into the specified size and homogeneously mixed (including surface and internal parts). Approximately 30 g powder samples were collected for different analytical tests. To terminate the reaction of cement hydration, the samples were soaked in isopropanol (liquid/solid=10:1 by volume) and then placed in a vacuum glass dryer (with dried silica gel) for 2 days to remove the free water from the samples. The thermal decomposition behavior of the powder samples was measured by TGA (Rigaku Thermo Plus) from 30 to 1000 °C at 10 °C min^{-1} with argon purge gas. The crystalline phases of powder samples were examined by using XRD (SmartLab) with a high sensitivity 2D detector (HyPix-3000) with CuKα radiation (λ = 1.54 Å) operating at 45 kV and 200 mA. The scanning range was between 10° and 60° 2θ at a rate of 50° min^{-1} with a step size of 0.02 °. For Q-XRD analysis, the analytical grade corundum (Al_2O_3) at a dosage of 20 wt.% was added into powder samples as the internal standard to calculate the content of the amorphous phase. Phase identification and Rietveld quantitative phase analysis were carried out by a WPPF method in the integrated X-ray powder diffraction software (PDXL). The fitting model and the references for the structural database are shown in Table S4.3 and Table S4.4. The Q-XRD analysis was regarded as a semi-quantitative method because of the likelihood of methodical errors. The changes in bound water and bound CO_2 in the samples would slightly affect the comparisons of the Q-XRD results. To minimize the errors caused by the change of bound water, the Q-XRD results were only used qualitatively for verifying the TGA results and inferring the roles of biochar in the same cement system with the same curing condition. The content calculation and the calculation procedures for TG and Q-XRD analysis are summarized in Table S4.5 and S4.6. The microstructural features and elemental distribution of gold-coated sample were characterized by SEM) with EDX (TESCAN VEGA3 XM). The pore size distribution of the biochar blocks was evaluated by a MIP (Micromeritics Autopore IV). Hg was intruded into the voids of the crushed samples (2.36–5.00 mm) at the applied pressure from 0.007 MPa to 207 MPa.

4.3 Results and discussion

4.3.1 Different biochar in magnesia cement systems under air curing

Incorporation of Air BC in the magnesia cement system slightly facilitated the formation of cement hydrates. The curves of derivative thermogravimetric analysis (DTG) of MC samples air-cured for 28 days are shown in Figure 4.1a. Sharp mass loss peaks at 370°C could be attributed to the dehydration of $Mg(OH)_2$ (Zhu et al., 2017), whereas the mass loss peaks at 560°C and 640°C could be ascribed to the decomposition of poorly crystallized and well-crystallized $MgCO_3$, respectively (Zhang et al., 2018). In the MC sample (without biochar) (Figure S4.1a), 13.2 wt.% mass loss at 370°C was equivalent to 42.4 wt.% $Mg(OH)_2$ content, which is an important indicator of the hydration degree of MC determining the mechanical strength of MC-based blocks (Zhang et al., 2020; Chen et al., 2020). The 10.9 wt.% $MgCO_3$ in the MC sample resulted from the carbonation of $Mg(OH)_2$ and the non-calcined $MgCO_3$ in raw cement (Zhang et al., 2018). After the incorporation of Air BC (2 wt.% of binder), the content of $Mg(OH)_2$ increased from 42.4 to 44.0 wt.%. This suggested that the Air BC slightly promoted the MC hydration process, which could be attributed to the internal curing effect of biochar. Figure S4.2 shows the schematic diagram of internal curing effect of biochar in the cement system. The adsorbed water in pre-soaked biochar would be released to promote continual hydration of the unreacted cement particles. The XRD (Figure 4.1b) and Q-XRD (Figure S4.1b) results evidenced that the incorporation of Air BC promoted the generation of brucite (crystalline $Mg(OH)_2$) and amorphous phases (namely, poorly-crystalline products).[35] The additional hydrates are favorable for the strength enhancement of MC-blocks.

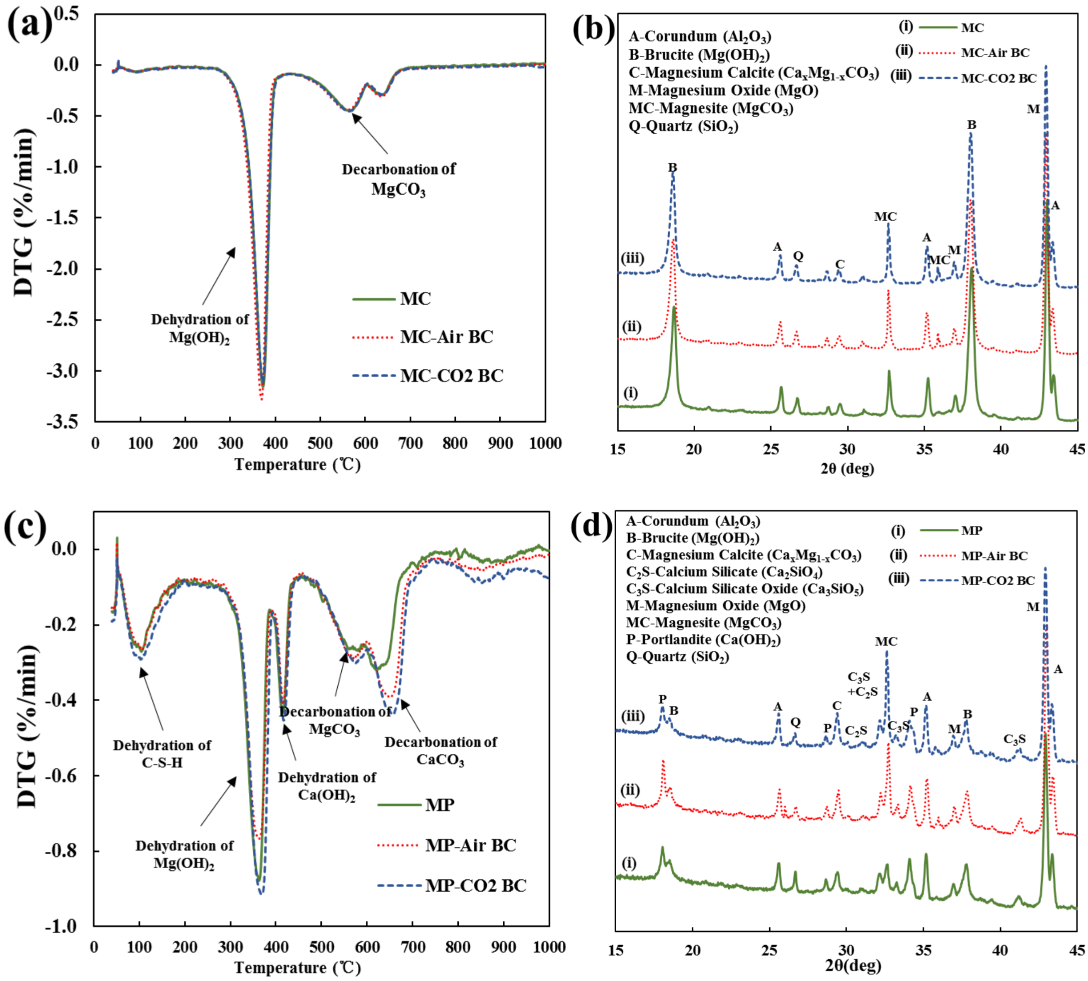

Figure 4.1. DTG curves and XRD diffractograms of 28-d air cured MC and MP pastes with biochar addition: (a) DTG of MC pastes; (b) XRD diffractograms of MC pastes; (c) DTG of MP pastes; (d) XRD diffractograms of MP pastes.

Incorporation of CO_2 BC facilitated the carbonation of magnesia cement system even during normal air curing. As shown in Figure S4.1a, compared to the MC sample, the MC-CO_2 BC sample did not increase $Mg(OH)_2$ content but slightly increased the content of $MgCO_3$ (10.9 wt.% vs 11.6 wt.%) (Figure 4.1a), indicating that $Mg(OH)_2$ partially transformed into $MgCO_3$ with the help of CO_2 BC. The Q-XRD results corroborated that the contents of $MgCO_3$ and $MgCO_3·3H_2O$ increased along with the addition of CO_2 BC. Such accelerated carbonation suggested that the CO_2 was adsorbed in the CO_2 BC and reacted with $Mg(OH)_2$. SEM images of Air BC and CO_2

BC (Figure S4.3) show that the pores in CO_2 BC are larger than that in Air BC. This was because CO_2 gasification could increase the carbon conversion through Boudouard reaction and enhance the release of volatile organic compounds (Shen at al., 2019). Therefore, CO_2 BC were found to be more efficient for facilitating the CO_2 diffusion and carbonation of MC in the curing process.

Addition of Air BC significantly promoted the hydration and carbonation of MP-based pastes. The DTG and TG curves of the MP pastes air-cured for 28 days are given in Figure 4.1c and S1c. From Figure 4.1c, a mass loss peak from 60°C to 200°C in MP samples was ascribed to the dehydration of HMCs and C-S-H gels. The mass loss peaks at 370°C, 410°C, 570°C and 680°C corresponded to the dehydration of $Mg(OH)_2$, dehydration of $Ca(OH)_2$, decarbonation of $MgCO_3$, and decarbonation of $CaCO_3$, respectively (Tu et al., 2016; Xuan et al., 2018). The incorporation of 2 wt.% Air BC in the MP system reduced the content of $Mg(OH)_2$ and $Ca(OH)_2$ by 5.50% and 19.7%, but increased the content of $MgCO_3$ and $CaCO_3$ by 3.70% and 25.9%, respectively, indicating that Ca^{2+} was preferentially carbonated in the MP system. This could be attributed to the fact that the dissolution and hydration of tricalcium silicate (C_3S) in Portland cement was much faster than that of MgO in magnesia cement, and the $CaCO_3$ could be relatively easy generated compared to $MgCO_3$ (ΔG of $CaCO_3$ at -73.0 kJ mol^{-1} vs ΔG of $MgCO_3$ at -30.2 kJ mol^{-1}) (Wang et al., 2020; Zhu et al., 2017). The Q-XRD results (Figure S4.1d) also showed that the addition of Air BC in the MP system increased the generation of carbonates. The effect of Air BC on the MP system was more effective than that on the MC system in terms of the change of hydration and carbonation products. This is probably attributed to the relatively high solubility and reactivity of Ca-based materials in the MP system (Zhu et al., 2017).

Compared to Air BC, CO_2 BC had a more remarkable effect on the promotion of hydration and carbonation of the MP system. From Figure 4.1c, the incorporation of 2 wt.% CO_2 BC increased the contents of all hydration and carbonation products, e.g., $Mg(OH)_2$, $Ca(OH)_2$, $MgCO_3$, and $CaCO_3$ by 13.7%, 1.60%, 34.1% and 48.4%, respectively, compared to the values in the pure MP samples. Similar to MP-Air BC samples, CO_2 BC preferentially promoted the carbonation of Ca-based materials in the MP system. However, the total mass loss of MP-CO_2 BC samples (19.4 wt.%) was much larger than those of MP samples (15.6 wt.%) and MP-Air BC samples (16.4 wt.%) (Figure S4.1c), suggesting the presence of abundant hydration and carbonation products in MP-CO_2 BC samples. The Q-XRD data supported that MP-CO_2 BC samples contained higher contents of hydrates and carbonates in comparison to MP-Air BC samples. As shown in Table S4.2, the BET surface areas of the Air BC and CO_2 BC were 326 m^2 g^{-1} and 358 m^2 g^{-1}, the pore volumes (BJH method) of Air BC and CO_2 BC between 1.7 nm and 300 nm were 0.047 cm^3 g^{-1} and 0.051 cm^3 g^{-1}, and the water adsorption of Air BC and CO_2 BC was 135% and 143%, respectively. The larger surface area and porosity in CO_2 BC could hold more water and quickly release for cement hydration, and favorable porous structure could facilitate CO_2 diffusion for the accelerated carbonation. Therefore, CO_2 BC was more conducive to promoting the hydration and carbonation of the MP-based pastes.

Incorporation of gasification biochar, especially CO_2 BC, significantly enhanced the strength of MP-based blocks while slightly improving the compressive strength of MC-based blocks. In Figure 4.2, the incorporation of 2 wt.% Air BC and CO_2 BC caused a reduction in compressive strength for 7-d cured MC samples but led to an increase in compressive strength for 7-d cured MP samples. The reduction in compressive strength for 7-d cured MC samples might be attributed to the brittle structures and large volume of pores in the biochar (Figure S4.5). However, in MP samples, the positive effects of biochar (e.g., facilitating the generation of C-S-H gel) overcame the negative effects of biochar (e.g., introducing the brittle structures and large volume of pores). After 28-d curing, the compressive strength of MC-Air BC and MC-CO_2 BC blocks were 3.10% and 10.2% higher than that of the MC samples, which was associated with their relatively high contents of hydration and carbonation products as illustrated in TGA and XRD results. MIP results (Figure S4.5) verified that the incorporation of CO_2 BC introduced capillary pores but the abundant reaction products could fill the mesopores. Besides, all the MP samples yielded higher compressive strength than the MC samples (Figure 4.2), owing to the higher strength of C-S-H gel from Portland cement hydration in the MP samples, compared to the $Mg(OH)_2$ from hydration of magnesia cement in MC samples (Guo et al., 2020). In the MP system, the 7-d and 28-d compressive strengths of biochar-incorporated samples were higher than that of pure MP samples. In particular, the incorporation of 2 wt.% CO_2 BC effectively increased the 28-d compressive strength by 43.1% due to the generation of abundant hydration and carbonation products as evidenced by TGA and XRD results. These results verified that the addition of gasification biochar promoted the hydration and carbonation process in both MC and MP systems, and significantly enhanced the compressive strength of cement-based blocks, especially for MP-based blocks.

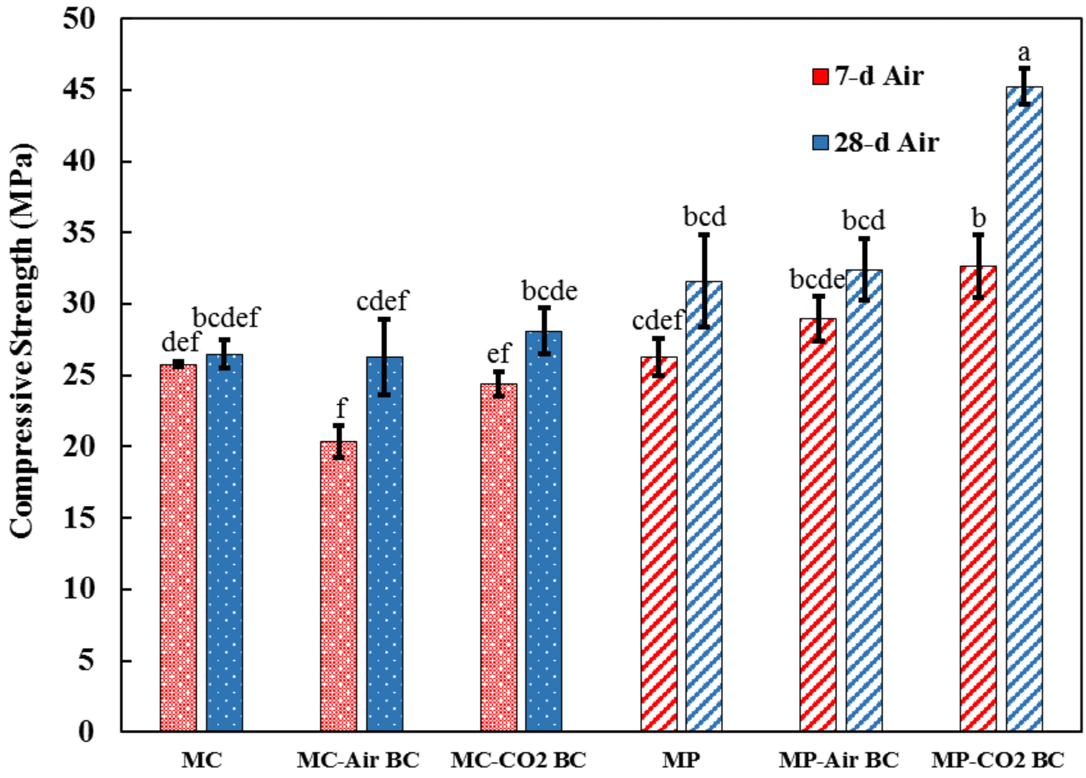

Figure 4.2. Compressive strength of air cured MC and MP blocks with biochar addition (the letters (a-f) denote statistically significant differences of the experimental results).

4.3.2 Synergistic effects of biochar and CO_2 curing on the cement systems

CO_2 curing accelerated the carbonation of MC-based pastes, and the incorporation of biochar facilitated the formation of hydrated magnesium carbonates. As shown in Figure S4.4, the overall mass loss (25.2%) of MC samples after 1-d CO_2 plus 6-d air curing was larger than that (20.9%) of MC samples after 28-d air curing (Figure S4.1a), suggesting a larger amount of hydration and carbonation products in CO_2 cured samples. From Figure 4.3a, new mass loss peaks appeared at 120°C and 420°C in the MC samples after CO_2 curing, which were attributed to the dehydration and decarbonation of HMCs, respectively. The mass losses of HMCs in biochar-incorporated MC samples, especially in MC-CO_2 BC samples, were larger than that in pure MC samples. The Q-XRD results show that the incorporation of 2 wt.% CO_2

BC resulted in an increase of carbonate content. This reinforced that the porous structure of biochar, especially in CO_2 BC, could facilitate CO_2 diffusion and accelerated carbonation.

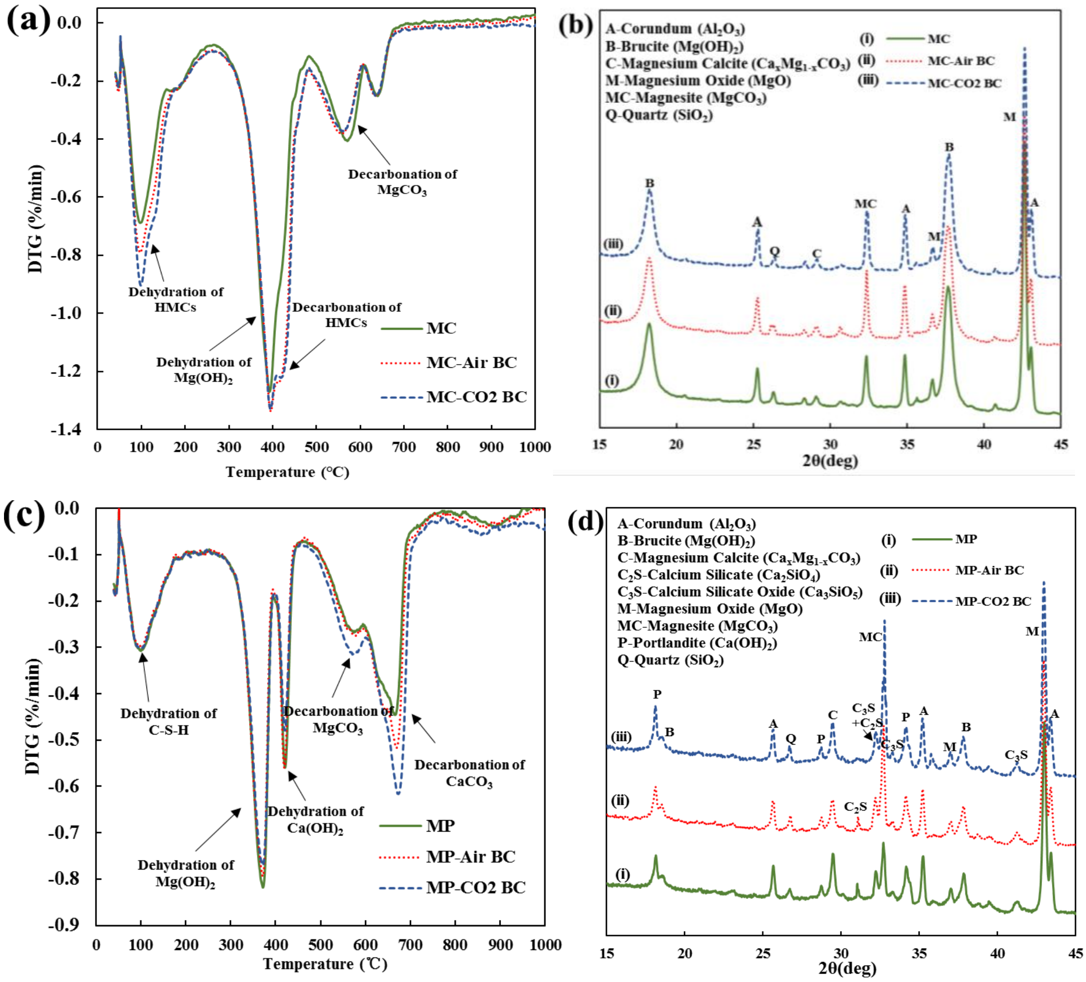

Figure 4.3. DTG curves and XRD diffractograms of biochar-incorporated MC and MP pastes after 1-d CO_2 plus 6-d air curing: (a) DTG of CO_2 cured MC pastes; (b) XRD diffractograms of CO_2 cured MC pastes; (c) DTG of CO_2 cured MP pastes; (d) XRD diffractograms of CO_2 cured MP pastes.

As illustrated in SEM imaging (Figure 4.4), CO_2 cured MC samples had a large amount of unreacted MgO particles on the rough surface, which was mainly $Mg(OH)_2$ (Wang et al., 2019c). By comparison, dense hydration and carbonation products were observed on the surface of porous biochar in the CO_2 cured MC-Air BC samples, while some reaction products even filled in the pores of biochar in CO_2 cured MC-CO_2 BC samples. Elemental mapping (Figure 4.4b) showed that Mg and O were the predominant elements in the MC samples with negligible C detection. In contrast, the C content for $MgCO_3$ or HMCs was evenly distributed in the MC-CO_2 BC samples (Figure 4.4c). This clearly shows that biochar enhanced the carbonation degree of MC-based pastes during CO_2 curing.

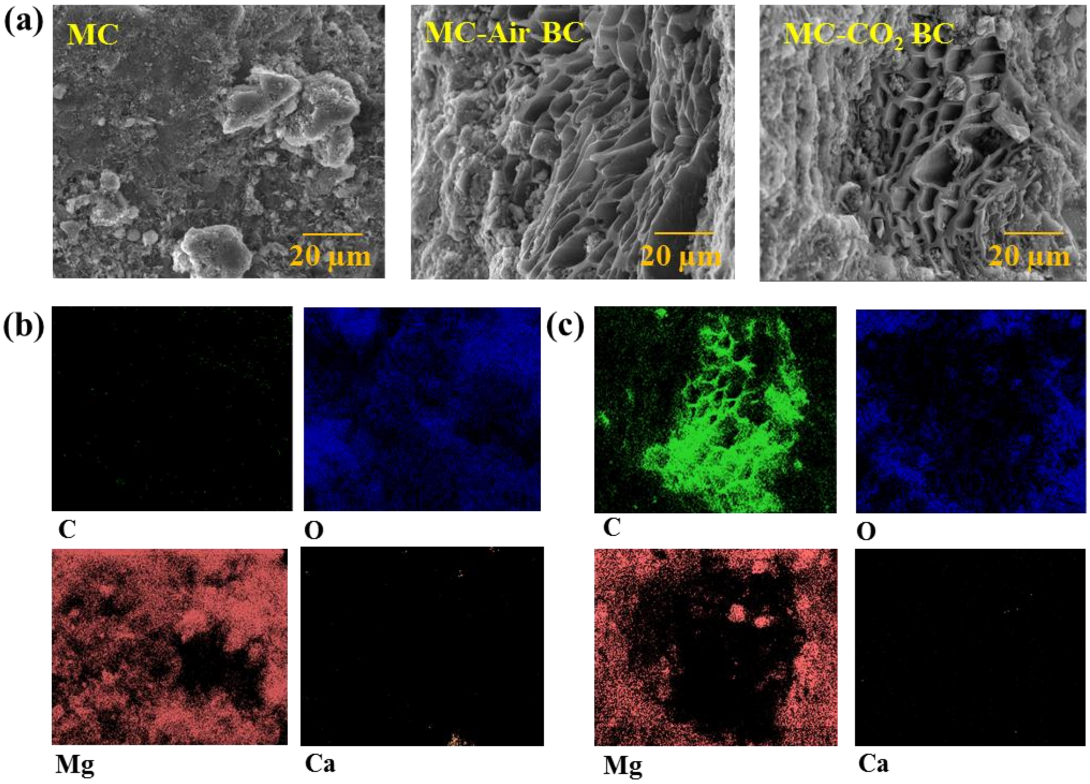

Figure 4.4. SEM images and elemental mapping of biochar-incorporated MC pastes after 1-d CO_2 plus 6-d air curing: (a) SEM images of MC, MC-Air BC and MC-CO_2 BC samples; (b) Element mapping of MC sample; and (c) Element mapping of MC-CO_2 BC sample.

After 1-d CO_2 plus 6-d air curing, the contents of HMCs, $MgCO_3$, and $CaCO_3$ in the MP samples significantly increased, $CaCO_3$ increased by 55.4% in particular (Figure 4.3c), in comparison to the air cured MP samples (Figure 4.1c). This confirmed that the Ca-rich hydrates in the MP system were preferentially carbonated due to the higher solubility of $Ca(OH)_2$ and lower formation energy of $CaCO_3$ (Wang et al., 2020d). After the addition of biochar (Figure 4.3c, d), the contents of unreacted cement, $Ca(OH)_2$ and $Mg(OH)_2$ further decreased, whereas the contents of $CaCO_3$, HMCs, and $MgCO_3$ increased. The CO_2 BC was more effective than the Air BC. It is noted that the molar volume of $CaCO_3$ is 10.1% larger than $Ca(OH)_2$, while the molar volume of $MgCO_3$ is 15.2% larger than $Mg(OH)_2$. Therefore, the accelerated carbonation with the aid of biochar would densify the microstructure and improve the mechanical strength as well as dimensional stability of the MP-based pastes (Chen et al., 2020).

Figure 4.5 shows that the compressive strength of MC blocks after 1-d CO_2 curing increased to 38.3 MPa, i.e., 1.5 times of that of the MC samples air-cured for 28 days (Figure 4.2). The incorporation of Air BC and CO_2 BC further increased the compressive strength by 5.80% and 13.9%, respectively, which was attributed to higher contents of carbonation products (mainly HMCs) in the biochar-augmented composites as indicated by the TGA and XRD results (Figure 4.3 and S4.3). As for the MP system, the compressive strength of MP blocks after 1-d CO_2 curing achieved 93.6% of that measured for the samples after 7-d air curing or 77.8% for the samples subject to 28-d air curing. This reflected the efficient transformation from $Mg(OH)_2$ to HMCs. The strength of MP samples increased by 75.2% during the additional 6-d air curing, due to the rehydration of unreacted cement. Compared to the MP samples, the MP-Air BC samples and MP-CO_2 BC showed 1.09% and 16.9% enhancement of 1-d CO_2 plus 6-d air curing compressive strength, respectively, indicating that CO_2 BC could provide channels for CO_2 diffusion during the 1-d CO_2 curing and also release water for rehydration of unreacted cement during the subsequent 6-d air curing. Therefore, the innovative, combined use of porous biochar and CO_2 curing is an effective approach for reducing carbon footprint and enhancing the properties of cement-based blocks.

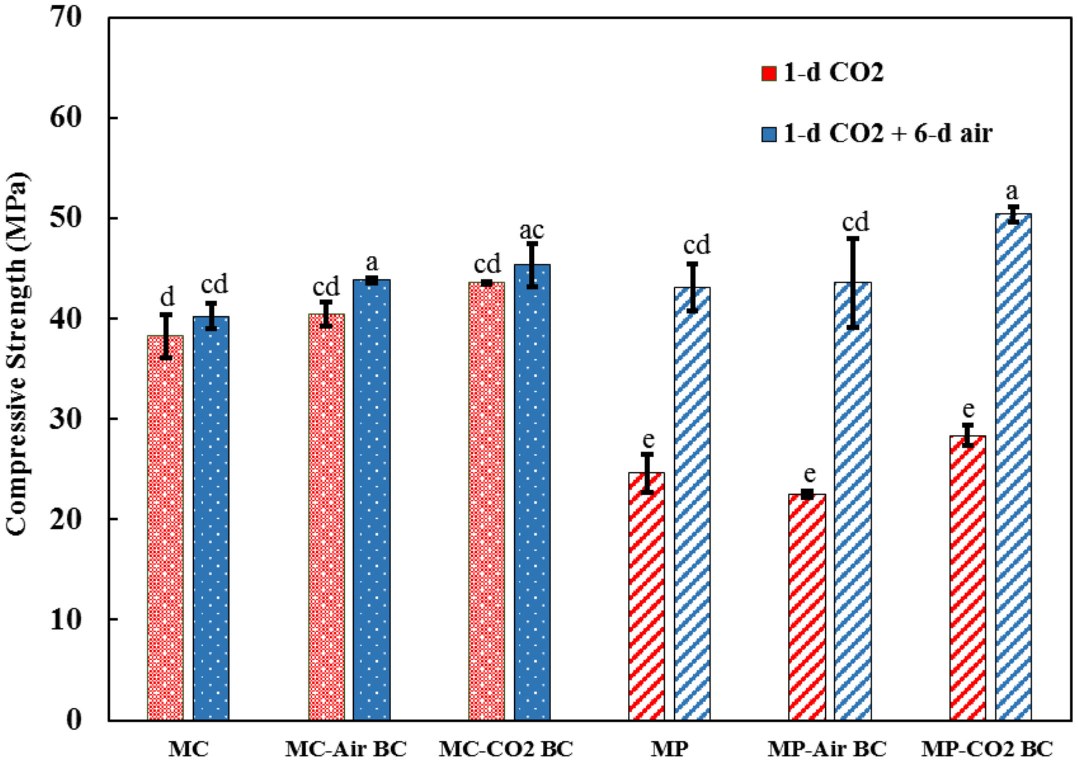

Figure 4.5. Compressive strength of CO_2 cured MC and MP blocks with biochar addition (the letters (a-f) denote statistically significant differences of the experimental results).

4.4. Conclusions

This study articulated the roles of biochar in cement-based pastes and evaluated the synergistic effect of biochar and CO_2 curing on promoting the hydration and carbonation of magnesia cement (MC) and magnesia cement-Portland cement (MP) systems. According to the XRD and TGA results, the incorporation of 2 wt.% biochar slightly facilitated hydration of MC system during air curing, whereas it could significantly promote the hydration and carbonation of MP-based pastes. In this study, CO_2 gasification biochar (CO_2 BC) was more effective than air gasification biochar (Air BC), possibly due to the larger water storage capacity in CO_2 BC for internal curing and rehydration of unreacted cement. Moreover, CO_2 curing accelerated the carbonation of MC and MP pastes, and the incorporation of biochar, especially CO_2 BC, displayed a synergism for the accelerated carbonation, because porous biochar could provide channels for CO_2 diffusion and intensive carbonation. Therefore, porous biochar together with CO_2 curing could be a promising and green approach for reducing carbon footprint and enhancing properties of cement-based composites.

CHAPTER 5. Development of biochar-augmented carbon-negative concrete

5.1 Introduction

In recent literatures, to achieve a comparable mechanical strength, only up to 5 wt.% substitution of cement by biochar has been adopted in the cement system, because strength degradation would be inevitable due to the introduction of excessive porosity (Wang et al., 2020b). In this study, innovative use of biochar as the aggregate and employment of dry-mix and mechanical pressure molding methods are proposed to increase the dosage of biochar application in concrete production. To further reduce carbon footprint and regulate the cement reaction of biochar-augmented concrete, low-carbon SCMs were selected and evaluated in biochar-augmented systems. For example, GGBS, an industrial waste from iron and steel production, can generate secondary C-S-H gel through spontaneous hydration reaction (Li et al., 2016; Chen et al., 2020). SF is a by-product of silicon and ferrosilicon alloy production with high content of activated silicon dioxide, which can react with CH via pozzolanic reaction and produce additional C-S-H gel (Goodarzi et al., 2016). Class-F PFA, an industrial waste from coal-fired power plants, can partially replace cement and achieve comparable mechanical properties because of additional hydration products (Chen et al., 2019). Metakaolin (MK), obtained from the calcination of kaolinite, is also a pozzolanic material due to the presence of activated silicon dioxide and aluminum oxide with partially disordered structures (Rahla et al., 2019). The interactions between these SCMs and biochar in a low-carbon cement system are not yet understood and need to be further investigated. Moreover, life cycle assessment (LCA) and cost-benefit analysis (CBA) of biochar-augmented construction materials should be conducted to quantify the environmental benefits and economic feasibility.

The primary objective of this study was to pioneer the innovative design of biochar-augmented carbon-negative concrete by incorporating biochar as the aggregate in concrete. We aimed to: (i) elaborate the roles of waste-derived biochar as aggregate in the cement hydration, microstructure, and strength development of biochar-augmented concrete by advanced characterization techniques; (ii) explore the effects of various widely available SCMs on the cement chemistry and mechanical properties of biochar-augmented concrete; and (iii) quantify and justify the total CO_2 emissions and economic value of biochar-augmented concrete by means of LCA and CBA.

5.2 Materials and methods

5.2.1 Materials

The primary cementitious material was CEM I 52.5 N OPC from Green Island cement company in Hong Kong. The chemical compositions of OPC measured by XRF are given in Table 5.1. The biochar was produced from pyrolysis of waste wood (*Acacia confusa* and *Celtis sinensis*) at 700 °C in Kadoorie Farm in Hong Kong. Figure S5.1 (a)&(b) shows the photo and microscopy image of biochar assessed by SEM at 20 kV operating voltage. The surface area and mean pore diameter were 142 m^2 g^{-1} and 2.01 nm, respectively**,** based on BET analysis using nitrogen adsorption-desorption isotherm method (ASAP 2020) at -196 °C. Biochar was screened to the size of 0-5 mm for the substitution of fine aggregate in concrete. The apparent density of biochar was 1.13 g cm^{-3} determined by using a Helium based gas Pycnometer (BELPYCNO L, MICROTRAC). Basic information on biochar is shown in Table 5.2. Biochar was pre-soaked in water for 24 h and then was vacuum filtrated to achieve SSD status. To further reduce the CO_2 emissions of biochar-augmented concrete, SCMs including GBBS, SF, PFA, and MK were used to partially replace cement. The chemical compositions of the raw materials are also summarized in Table 5.1. The particle size distributions of raw materials were analyzed by a laser diffraction particle size analyzer (Malvern Mastersizer 3000E) (Figure S5.2). Recycled fine aggregate (0–5 mm) and recycled coarse aggregate (5–10 mm) from Hong Kong EcoPark were employed in the production of the biochar-augmented concrete. The recycled aggregate was recycled from the construction and demolition wastes. The apparent density and the water absorption of the recycled aggregate were 2.53 g cm^{-3} and 3.55%, respectively.

Table 5.1 Chemical composition of raw materials (wt.%).

	Na_2O	MgO	Al_2O_3	SiO_2	SO_3	K_2O	CaO	Fe_2O_3
OPC	0.17	1.38	4.79	18.99	4.52	0.79	65.70	3.10
GGBS	0.00	6.19	15.35	35.34	2.37	0.85	38.33	0.31
SF	0.71	1.13	0.41	85.61	0.84	7.98	1.50	0.43
PFA	1.07	2.92	25.80	50.10	0.92	1.39	7.04	8.39
MK	0.00	0.00	48.20	49.1	0.00	0.23	0.24	0.52

OPC: ordinary Portland cement; GGBS: ground granulated blast furnace slag; SF: silica fume; PFA: pulverized fly ash; MK: metakaolin.

Table 5.2 Basic information of biochar.

	Biochar
Surface Area (m^2 g^{-1})	142
Total Pore Volume (cm^3 g^{-1})	0.08

Average Pore Diameter (nm)	2.01
Water Absorption Capacity (%)	83.57
Apparent Density (g cm^{-3})	1.13

5.2.2 Sample preparation

The mixture designs of biochar mortar and biochar blocks are shown in Table 5.3. Biochar blocks were produced as biochar-augmented concrete to determine the mechanical strength, life cycle assessment and cost-benefit analysis, whereas biochar mortar (without coarse aggregate) was made for characterizing the roles of biochar in the cement hydration and microstructure of biochar concrete. For the production of biochar blocks, dry-mix and mechanical pressure molding methods were applied, which is a widely used and high-efficiency method for the production of precast concrete (e.g., paving blocks and partition blocks). The water-to-binder ratio, applied pressure, biochar water content, and compaction duration were the key factors and were adjusted based on our preliminary trials and previous study (Wang et al., 2018c). SSD biochar was employed to replace the fine aggregate at the dosage of 10%, 20%, 30% by weight and the extra water-to-binder ratio was adopted at 0.18. In the production process, all materials were mixed for 5-min to achieve homogeneous mixing. The fresh mixture was cast in steel cylindrical molds (55-mm internal diameter) and compacted with 30 MPa pressure until the height of the samples was compressed to 55 mm. After additional 1-min compaction, samples were demolded immediately. All samples were covered with a waterproof membrane to maintain the moisture and cured at room temperature (23 ± 2 °C) for 28-d curing before the tests. For the production of biochar mortar, coarse aggregate was removed from the mixtures to mitigate the interference of quartz in the characterization tests and the water-to-binder ratio was optimized to be 0.3. The mixtures of biochar mortar after mixing were transferred from the mixer into cylindrical plastic containers with dimensions of 20 mm diameter × 50 mm height and sealed for 28-d curing before subsequent characterization tests.

Table 5.3 Mixture design (wt.%) of biochar block and biochar mortar.

(a) Biochar block	Cement	SCMs	SSD BC	RF	RC	W/B
Ref	30	0	0	30	40	0.18
10BC	30	0	10	20	40	0.18
20BC	30	0	20	10	40	0.18
30BC	30	0	30	0	40	0.18
30BC-BS	21	9	30	0	40	0.18
30BC-SF	21	9	30	0	40	0.18
30BC-FA	21	9	30	0	40	0.18
30BC-MK	21	9	30	0	40	0.18
(b) Biochar mortar	Cement	SCMs	SSD BC	RF	RC	W/B
Ref	50	0	0	50	0	0.30
10BC	50	0	17	33	0	0.30
20BC	50	0	33	17	0	0.30
30BC	50	0	50	0	0	0.30
30BC-BS	35	15	50	0	0	0.30
30BC-SF	35	15	50	0	0	0.30
30BC-FA	35	15	50	0	0	0.30
30BC-MK	35	15	50	0	0	0.30

SCMs: supplementary cementitious materials; SSD BC: saturated surface dry biochar; RF: recycled fine aggregate; RC: recycled coarse aggregate; W/B: water to binder ratio.

5.2.3 Characterization methods

The uniaxial compressive strength of biochar blocks was measured by using a compression testing machine (SERVO-PLUS) at a loading rate of 0.3 MPa s^{-1} according to the standard procedure (BS EN 12390, 2009). Characterization analysis was conducted on the homogeneously mixed powder of biochar mortar for analyzing the cement hydration process, chemical phases, and pore structure. The hydration heat of mortar mixtures during the first 45-h was recorded by an isothermal calorimeter (Calmetrix I-CAL 4000) at 20 °C. The mix proportions and mixing procedures were similar to the production of biochar mortar, whereas the whole procedure finished in 2 min. The 28-d mortar samples were soaked in isopropanol for 7-d to cease cement hydration and then were freeze-dried. TGA (Rigaku Thermo Plus) was conducted from 40 °C to 1000 °C at a heating rate of 10 °C min^{-1} under N_2 stripping gas atmosphere to assess the thermal decomposition behavior of mortar samples. The crystal phase of powder samples was measured by an XRD (SmartLab) with 9 kW rotating Cu anode X-ray source ($\lambda \sim 1.54$ Å) at the scanning range between 5° and 45°. Peak identification for the XRD data was run by using the MDI Jade 6 software. The morphology of the gold-coated samples was observed by applying BSE imaging mode. The polymerization of cement hydration products was analyzed by using a 500MHz solid-state NMR spectrometer (GEOL500). The ^{29}Si NMR analysis was performed at 99.368 MHz using a 7 mm CP magic angle spinning (MAS) probe. To collect full relaxation of the resonating signal, a rotation rate of 4500 Hz and a recycle delay of 30-s were applied. The deconvolution of ^{29}Si NMR spectra was run by using the Gaussian model in the Origin Pro software. Cylindrical samples with 20 mm diameter × 50 mm height, cutting from the biochar mortar, were prepared for the 3D pore structure analysis by using a microfocus X-ray computed tomography (CT, Phoenix v

| tome | x s).

5.2.4 Life cycle assessment and cost and benefit analysis

The total CO_2 emission of 1 tonne of biochar blocks with different mixtures was analyzed from a 'cradle-to-gate' perspective, which involves the CO_2 emission related to the acquisition of raw materials to the production of biochar blocks according to the performance standard (ISO, 2006). Figure S5.3 displays the system boundary of biochar blocks preparation with different formulations. The background data were obtained from the Ecoinvent 3.0 database (developed by the Swiss Centre for Life Cycle Inventories) and the ETH-ESU database. The influence of each type of biochar block on climate change was investigated by IPCC 2013 within a timeframe of 100 years. In view of the data variability, when performing an LCA, uncertainty analyses were performed to identify any variations owing to the various inventory sources used and improve the robustness of this investigation (Guo et al., 2012). Therefore, Monte Carlo simulation was performed for a stochastic study of life cycle assessment, which was used for the quantification of the uncertainty from the ranges of inputs. In this study, the transportation distance in terms of the aggregate transportation was assumed to be 30% longer than the current data used (i.e., 30 km by truck), and the energy needed for the concrete crushing was also assumed to be 30% higher than the current value (i.e., 13.75 kwh tonne $^{-1}$), resulting from the changes in the technologies adopted.

The Monte Carlo simulation consisted of probability distribution for the highly variable information such as transportation, energy and carbon emission that reflected the knowledge and process uncertainty related to the key parameters. During this simulation, 1000 runs were performed at a significance level $\alpha = 0.05$. The CO_2

emissions of biochar blocks involving the use of OPC, biochar, recycled aggregate, SCMs were quantified. Considering that there were no existing inventories with respect to the materials as aforementioned, the key data were obtained from the literature. Biochar was produced from the pyrosis of biomass that could adsorb CO_2 from the atmosphere. A large amount of carbon in biomass would be retained in biochar, resulting in the reduction of CO_2 in the atmosphere. The application of biochar could contribute to negative carbon emissions, ranging from -2.0 to -2.6 tonne CO_2 tonne^{-1} based on the worst-, average-, and best-case models (Azzi et al., 2019). The inventories of biochar were acquired from Azzi et al. 2019, where the biochar was pyrolyzed from woodchips from forest residues at 700 °C by using slow pyrolysis with indirect flue gas heating method. The environmental inventories resulting from OPC production were extracted from Li et al. 2015. The inputs and outputs of the material processing have already been considered in the LCA. But the inputs and outputs allocated to the production of PFA, GGBS, and SF were not taken into account in this study, because these materials were industrial by-products from the power and steel-making plants. The inventories of PFA and GGBS (similar to SF) were derived from Chen et al. 2010, whereas the inputs and outputs associated with the manufacturing of MK were acquired from Abbas et al. 2020. With respect to the recycled aggregate adopted, the energy consumed to crush the raw concrete was 13.75 kWh tonne $^{-1}$ (Dong et al., 2011). Meanwhile, to produce 1 tonne of recycled aggregate, 1.05 tonnes of raw concrete was required. The transportation distance of recycled concrete was 30 km (by truck) away from the regeneration center (Cui et al., 2016). When the crushed concrete was used as the recycled aggregate, the environmental impacts associated with the transportation of the crushed concrete to a landfill site (80 km by truck) (Cui et al, 2016) and other associated activities could be avoided during the assessment (Zhao et al., 2009; He et al., 2019). The transportation distance for OPC, SCMs or biochar to the factory was assumed negligible in the analysis.

The CBA of the biochar blocks was calculated based on the field data of the local brick factory and quotations from the largest e-commerce platform in the region (Alibaba et al., 2021). An example of CBA is provided in Table S5.1 to show the calculation details. The product benefit, disposal fee saving, carbon tax/credit, and overall benefit for each mixture are summarized in Table S5.2.

5.3 Results and Discussion

5.3.1 Hydration reaction of biochar mortar

Heat evolution curves (Figure 5.1a&b) illustrate that the addition of biochar increased the cumulative hydration heat per cement and accelerated the cement hydration process during 45-h curing. When 30 wt.% aggregate was replaced by biochar, the cumulative hydration heat increased by 18.9% compared to that of the control without biochar. The improvement of cumulative hydration heat started at Stage I and was further enhanced at Stage II and III. This improvement was because of the higher effective water-to-cement ratio for cement hydration in biochar-augmented samples. The pre-soaked SSD biochar could store water in pores and slowly release water during the cement hydration (Wang et al., 2021a). From the curves of hydration heat rate (Figure 5.1b), the peak at 9.8-h in the control corresponded to the hydration of C_3S. The deceleration period after 9.8-h was because unhydrated cement was wrapped by hydration products and the hydration rate became diffusion-controlled. The shoulder peak around 20 h was attributed to the formation of ettringite (AFt) from the hydration reaction between C_3A and gypsum (Hewlett et al., 2017), as shown in the following formula (1).

$$3CaO\cdot Al_2O_3 + 3(CaSO_4\cdot 2H_2O) + 26H_2O \rightarrow 3CaO\cdot Al_2O_3\cdot 3CaSO_4\cdot 32H_2O \qquad (1)$$

With the addition of biochar, the start of the acceleration period occurred slightly later but the duration could be prolonged, and the slope of the acceleration period in 20BC and 30BC samples was steeper due to higher effective water-to-cement ratio in biochar-augmented samples. The AFt formation peak in 10BC sample was comparable to the control sample. Moreover, the 10BC sample showed higher cumulative hydration heat than the control sample during the 45-h hydration process (Figure 5.1a), indicating that the biochar incorporation improved the hydration in the mortar system. Interestingly, the shoulder peak of 20BC and 30BC samples was observed earlier and enlarged significantly. Especially for the 30BC sample, the first peak was shifted to a later time at approximately 11.6-h and the shoulder peak even became larger than the first peak. It is noted that cement hydration and aluminum phase hydration have a competitive relationship for the limited availability of water. The formation of 1-mol AFt ($3CaO\cdot Al_2O_3\cdot 3CaSO_4\cdot 32H_2O$) consumed 32-mol water. Thus, the formation of AFt was incomplete in the low water-to-cement system but could proceed to a greater extent in the high water-to-cement system when 30 wt.% biochar was used to substitute virgin aggregate material. Furthermore, the AFt would expand during its formation, hence the early-age autogenous shrinkage could be reduced, and the early strength could be improved in the biochar-augmented concrete.

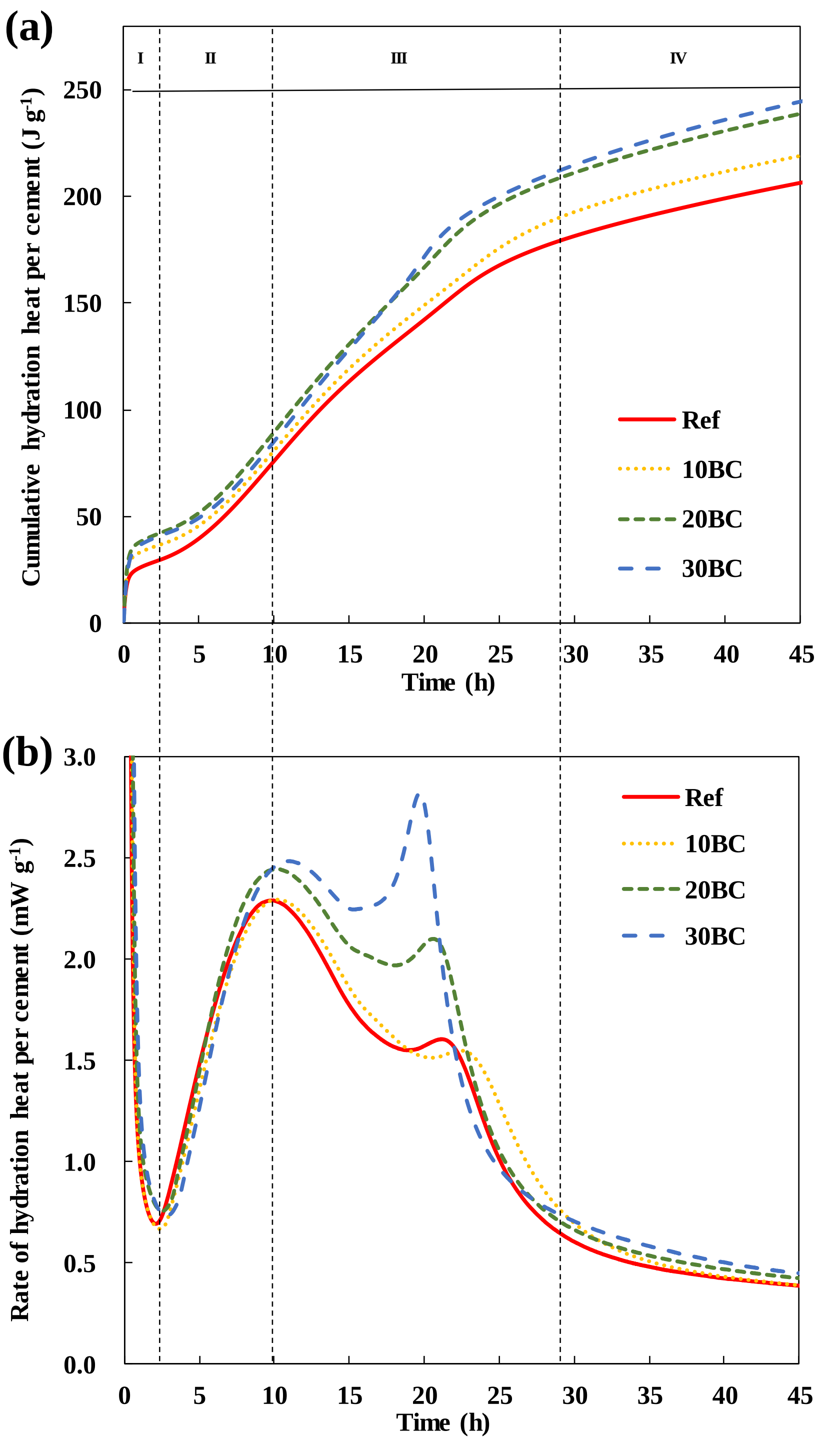

Figure 5.1. Isothermal conduction calorimetry results of biochar mortar: (a) cumulative hydration heat per cement and (b) rate of hydration heat per cement (Stage I: initial period; Stage II: acceleratory period; Stage III: deceleration period; Stage IV: slow reaction period).

The DTG curves of 28-d biochar mortar (Figure 5.2) indicate that the substitution by biochar facilitated the formation of cement hydration products. The DTG curves of the control show remarkable decomposition peaks of C-S-H gel, AFt and alumina ferric oxide mono (AFm) phases (50–200 °C), CH (380–480 °C) and $CaCO_3$ (CC) (500–800 °C) (Wang et al., 2020b). The presence of biochar significantly promoted the formation of C-S-H gel and AFt. The amount of bound water in C-S-H gel could not be quantified from the change of mass loss from 50 to 200 °C, but the variation of CH could serve as an important indicator of cement hydration degree. With 30 wt.% biochar replacement, the mass loss corresponding to the CH dehydration increased from 1.79 wt.% (equivalent to 7.35 wt.% CH) in the control to 3.46 wt.% (equivalent to 14.21 wt.% CH). The additional weight loss in the biochar-augmented samples between 500 ℃ and 1000 ℃ was attributed to the decomposition of refractory organic-C and inorganic-C in the biochar (Leng et al., 2019). In the Ref mortar system (with recycled fine aggregate), the hydration products were composed of the old hydration products originally from recycled fine aggregate and the newly formed hydration products from cement hydration. By contrast, in the biochar-augmented mortar, all the hydration products were newly formed from cement hydration. The content of hydration products in the biochar-augmented mortar was much higher than that in the Ref mortar, further corroborating that the biochar incorporation improved the generation of hydration products in the mortar system. In the XRD patterns (Figure 5.2b), only small AFt peaks at 9.1° could be observed, probably because the conversion to AFm phases and the sample grinding processing led to partial dehydration of AFt. Compared to the control, the C_3S peaks at 32.8° in the 30BC sample decreased while the CH peaks at 18.2° and 34.2° increased, confirming that the biochar facilitated the cement hydration.

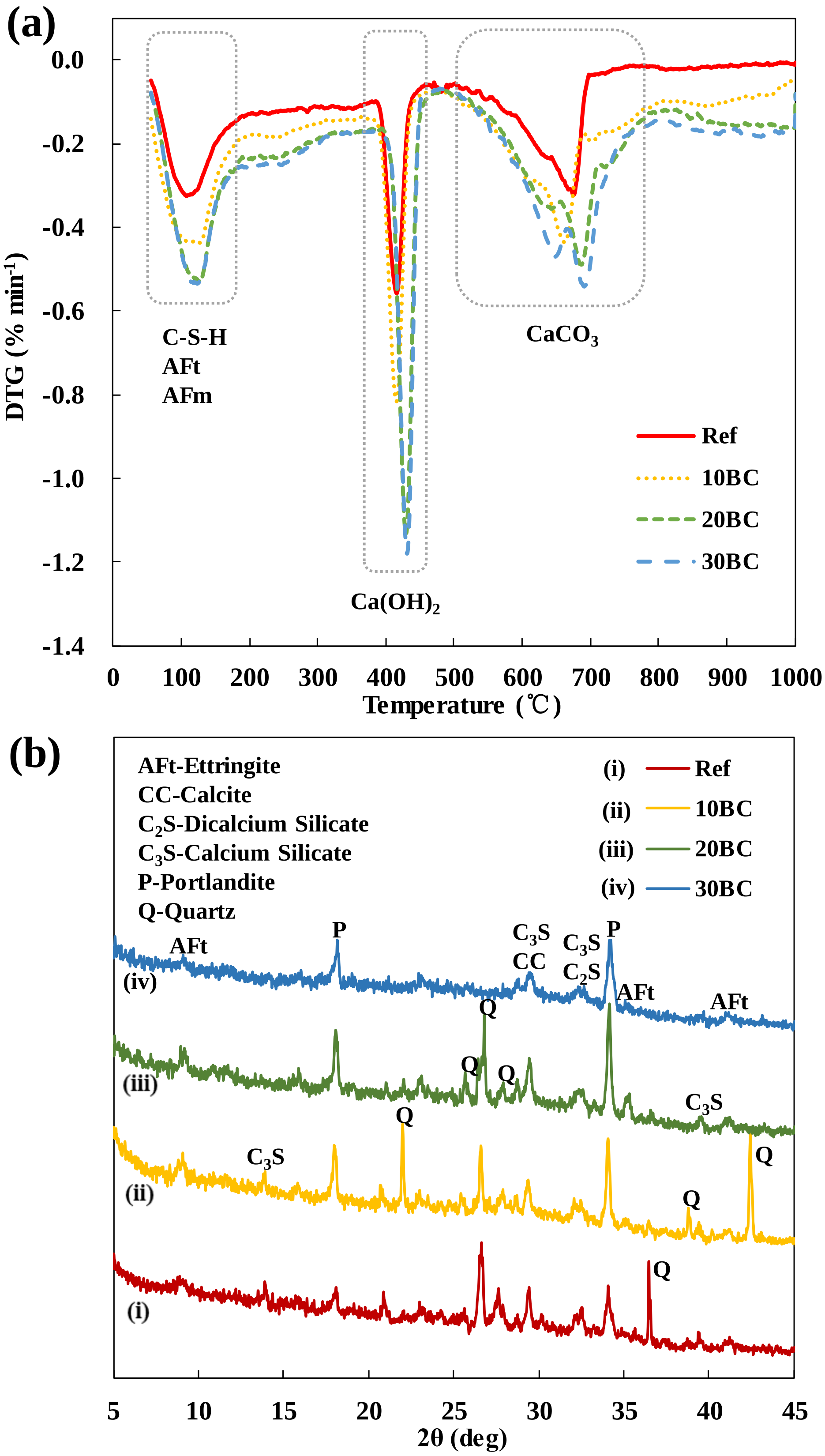

Figure 5.2. (a) DTG curves and (b) XRD patterns of the 28-d biochar mortar.

The results of ^{29}Si MAS NMR (Figure 5.3) illustrate that the biochar addition not only facilitated the formation of C-S-H gel but also increased the polymerization of C-S-H gel. The Q^0 peak at chemical shift of 70 ppm corresponded to the unreacted cement clinkers (C_2S and C_3S) (Krakowiak et al., 2015; Jeong et al., 2018). The Q^1 peak at the chemical shift of 79 ppm and the Q^2 peak at the chemical shift of 83 ppm could be identified as the end-chain unit and middle-chain unit, respectively, in the layered structure of C-S-H gel (Kim et al., 2012; Wang et al., 2021b). The quantification of different fractions of C-S-H gel in the mortar systems and the related parameters are shown in Table 5.4. The Q^3 peak (corresponding to the cross-linking unit of C-S-H gel in carbonated cement) and Q^4 peak (corresponding to the quartz) from recycled aggregate were detected in the control and 10BC samples. The Q^3 and Q^4 fractions decreased with the increasing substitution of aggregate by biochar, and eventually disappeared in the 30BC sample. To investigate the effect of biochar on the formation and structure of C-S-H gel in the cement hydration process, the fractions of Q^3 and Q^4 from recycled aggregate were deducted and the remaining proportions were adjusted. With the increasing substitution of recycled fine aggregate by biochar, the Q^0 fraction also decreased whereas the Q^1 and Q^2 fractions increased, which evidenced that the biochar replacement promoted the formation of C-S-H gel. This was because biochar can store water in pores and slowly release it to promote the transformation from Q^0 species into Q^1 and Q^2 species. The relatively high surface area of biochar may also promote cement hydration by providing additional nucleation sites for the generation of C-S-H gel, namely the nucleation effect. Yet the influence of surface functional groups and dissolved organic matter of biochar on the cement hydration should be further investigated in future studies. Compared to the control, the degree of hydration (DoH) of the silicate phase significantly increased by 44.3% when 30 wt.% recycled aggregate was substituted by biochar. The connectivity value D_c, representing the polymerization degree in the C-S-H gel and the mean chain length (MCL) of silicate chain, also increased with the increasing proportion of biochar substitution, suggesting the formation of the dense and stable C-S-H gel.

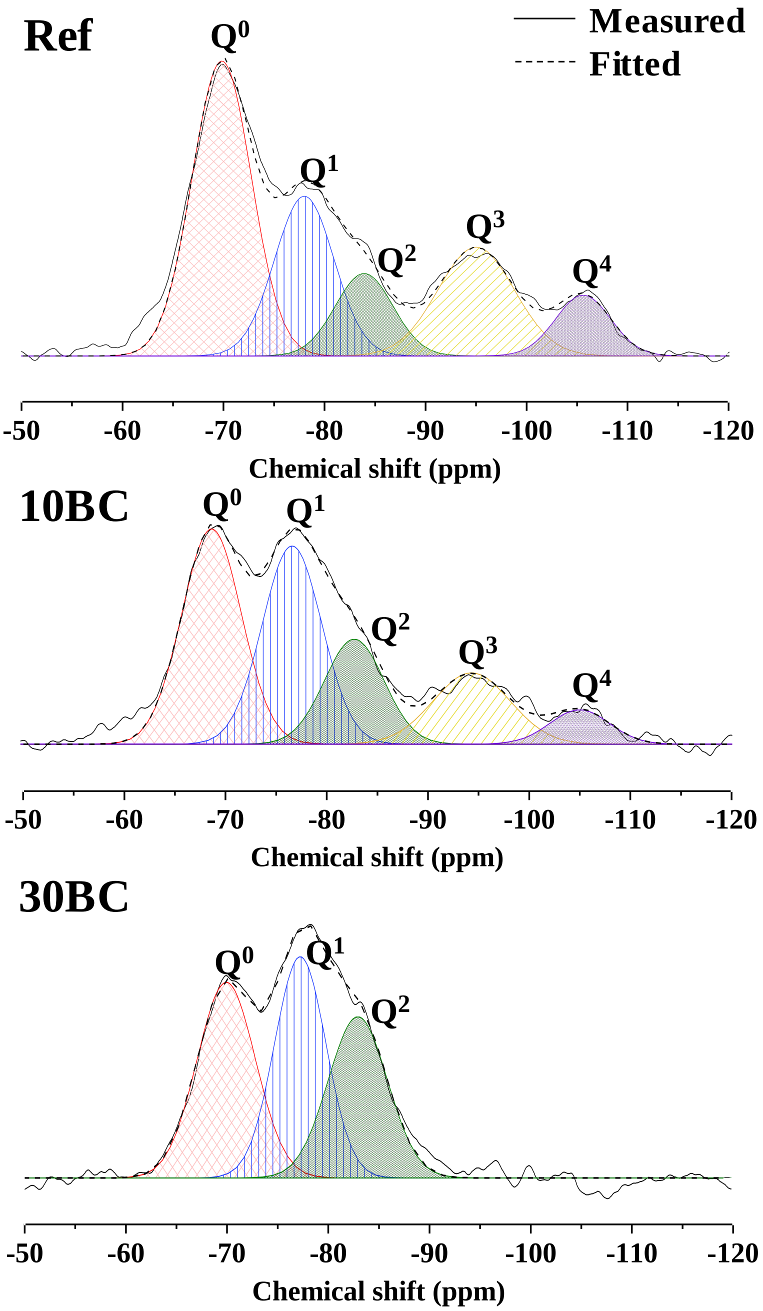

Figure 5.3. ^{29}Si NMR spectra for the 28-d biochar mortar.

Table 5.4. Calculation results of ^{29}Si NMR spectra.

	Q^0 (%)	Q^1 (%)	Q^2 (%)	DoH (%)	Dc	MCL
Ref	55.2	29.9	15.0	44.8	1.33	3.00
10BC	41.5	38.2	20.3	58.5	1.35	3.06
30BC	35.3	35.2	29.5	64.7	1.46	3.68
30BC-BS	28.3	46.5	25.3	71.7	1.35	3.09
30BC-SF	20.8	43.3	35.8	79.2	1.45	3.65
30BC-FA	41.1	37.4	21.6	58.7	1.37	3.15
30BC-MK	36.4	41.3	22.4	63.6	1.35	3.08

DoH: degree of hydration of silicate phase; DoH = $100 - Q^0$;

D_c: connectivity value; $D_c = Q^1 + 2 \times Q^2 / (Q^1 + Q^2)$;

MCL: mean chain length of the silicate chain; $MCL = 2 \times (Q^1 + Q^2) / Q^1$;

Note: the Q^3, Q^4 (mAl) fractions in recycled concrete, unreacted SF, MK and PFA were deducted, and the remaining proportions were adjusted.

5.3.2 Efficacy of SCMs on biochar-augmented concrete

Heat evolution curves (Figure 5.4a&b) demonstrate that the incorporation of SCMs slightly decreased the cumulative hydration heat per binder and changed the cement hydration process. The incorporation of SF and MK accelerated the hydration process and increased the cumulative hydration heat during the first 20-h curing. The aluminate reaction peak (as illustrated in formula 1) was accelerated and overlapped with the silicate reaction peak in the 30BC-MK sample. This significant acceleration of aluminate (i.e., C_3A) reaction process was attributed to the high content of ultra-fine activated aluminum phase in MK (48.2 wt.% Al_2O_3). The hydration heat rate of the 30BC-MK sample soared to 7.83 mW g^{-1} due to the heat released from the intense reaction of the activated aluminum phase. Such intense hydration heat rate could not be observed in the ordinary cement-MK system, while intense hydration of the aluminum phase occurred in the biochar-augmented system. This was only made possible by the sufficient amount of water released from biochar. The small particle sizes of SF and MK (Figure S5.2) were also necessary for this acceleration. The pozzolanic and hydraulic activity of SCMs were highly associated with the rate of hydration heat evolution. In contrast, the replacement of 30 wt.% cement by GGBS and PFA prematurely ended the accelerated period and reduced the hydration heat rate. This was because the hydration heat of GGBS and PFA with mild pozzolanic and hydraulic activity could not compensate for the reduced content of cement. Compared to the 30BC-BS sample, the PFA replacement reached a higher aluminate reaction peak due to its higher Al_2O_3 content (25.8 wt.% vs 15.4 wt.%). These results clearly indicate that the selection of different SCMs has distinctive interactions with biochar and influences the biochar-augmented cement hydration process.

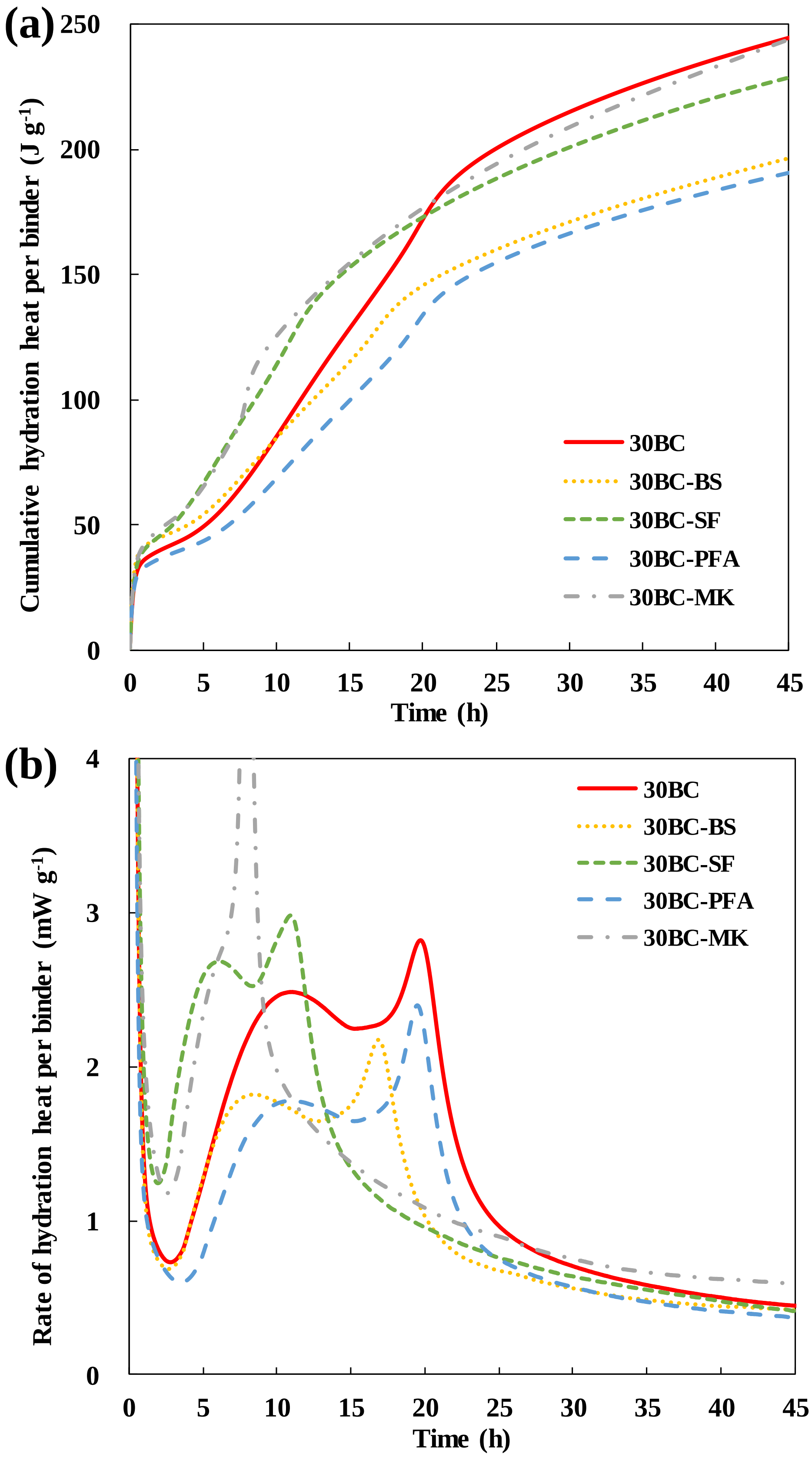

Figure 5.4. Isothermal conduction calorimetry results of biochar mortar with SCMs incorporation (a) cumulative hydration heat per binder and (b) rate of hydration heat

per binder.

The TGA and XRD results (Figure 5.5a) indicate that except for the PFA, the SCMs incorporation increased the formation of cement hydration products. In 30BC-BS, 30BC-SF and 30BC-MK samples, CH was consumed to form additional C-S-H gel and C-A-S-H gel via pozzolanic and hydraulic reaction. The additional AFt and AFm were also generated due to the abundant Al phase and water supply from biochar. The replacement of cement by GGBS successfully compensated the 30 wt.% lower cement content and generated additional C-S-H gel through the spontaneous hydration reaction in 28 d. The mass loss due to CH dehydration decreased from 3.5% (corresponding to 14.2% CH) in 30BC to 1.7% (corresponding to 6.9% CH) for 30BC-SF and 1.8% (corresponding to 7.3% CH) for 30BC-MK, verifying the robust pozzolanic activity of SF and MK in 28-d curing. Due to the diluted effect, the replacement of PFA that had a relatively low activity slightly decreased the content of hydration products. From the XRD patterns (Figure 5.5b), additional peaks of hemicarboaluminate (Hc) and monocarboaluminate (Mc) could be observed with the incorporation of GGBS, PFA and MK, indicating that the specific AFm phases were Hc and Mc. The strongest peaks of AFt and Hc were shown in the 30BC-MK sample, corresponding to the highest content of aluminum phase (48.2 wt.% Al_2O_3) in MK. The formation of additional AFt and Hc might reduce the porosity and improve the mechanical strength of the biochar block.

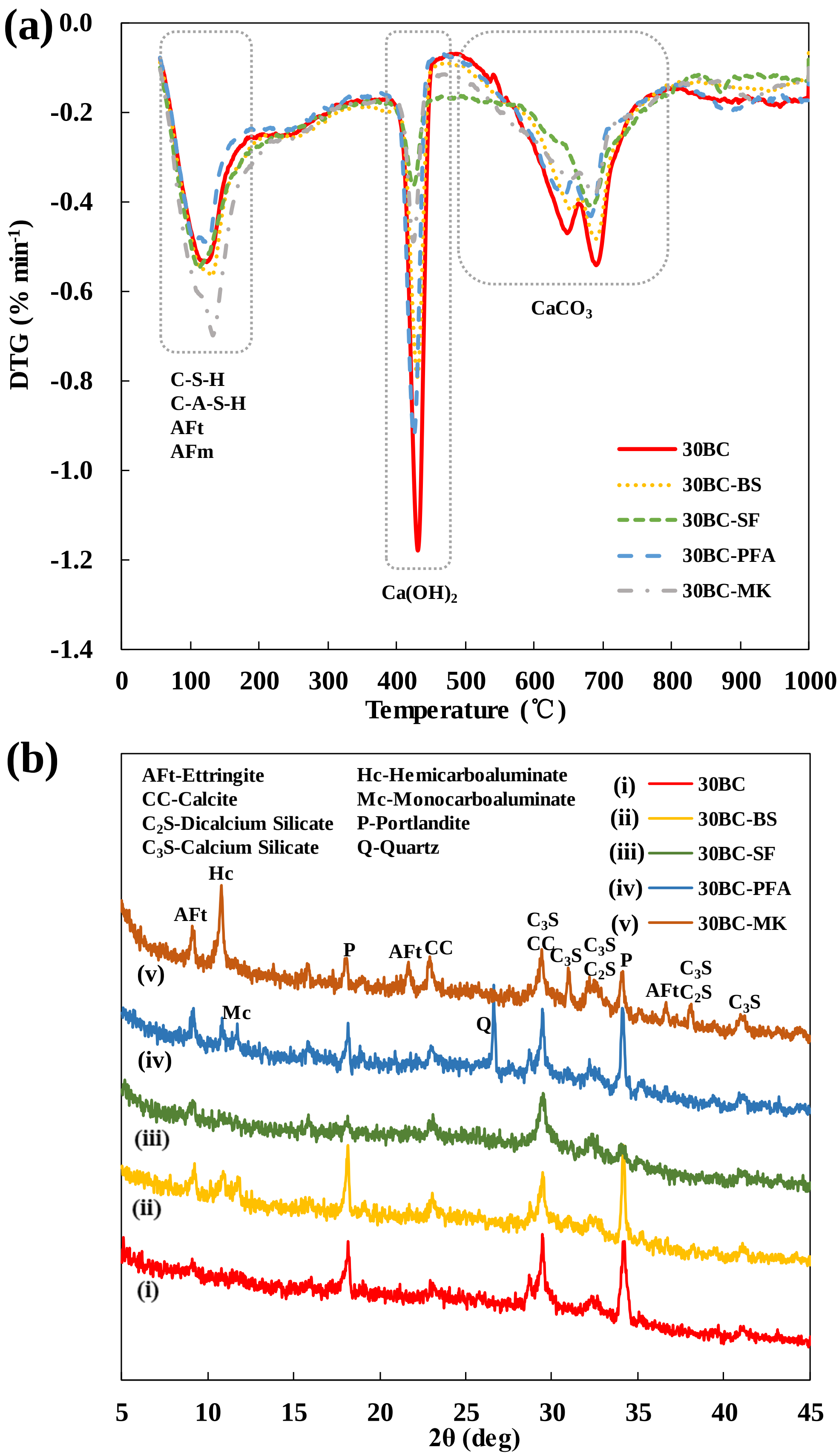

Figure 5.5. (a) DTG curves and (b) XRD patterns of the 28-d biochar mortar with SCMs incorporation.

From Figure 5.6, ^{29}Si MAS NMR results demonstrate that the incorporation of SCMs further modified the silicate phase of C-S-H/C-A-S-H gel. The GGBS mainly consists of small amounts of low-crystallinity phases and the depolymerized calcium silicate glasses within the melilite group (Skibsted et al., 2013). The peaks of unreacted silicate phase (i.e., C_3S and C_2S) in cement and unreacted GGBS were overlapping, thus their fractions were both included in the Q^0 fraction. Compared to the 30BC sample (Figure 5.4), the GGBS incorporation further decreased Q^0 phase but increased Q^1 and Q^2 phase (Figure 5.6) due to the secondary formation of C-S-H, resulting in a relatively higher DoH of silicate phase (Table 5.4). The incorporation of SF achieved the highest DoH (79.2%) of the silicate phase. The D_c and MCL values of the silicate chain were comparable to the 30BC sample, indicating the similar structure of C-S-H gel. The MK-incorporated sample showed comparable Q^1 and Q^2 fractions to 30BC, corroborating that the secondary C-S-H/C-A-S-H gel via pozzolanic reaction fully compensated the 30 wt.% reduction of cement content. The 58.7% DoH of the PFA samples was lower than that of 30 BC samples because of the relatively low pozzolanic activity of PFA. Base on the heat evolution, TGA, XRD, and NMR results, the addition of MK exhibited the highest improvement in the biochar-augmented cement hydration among the four studied SCMs.

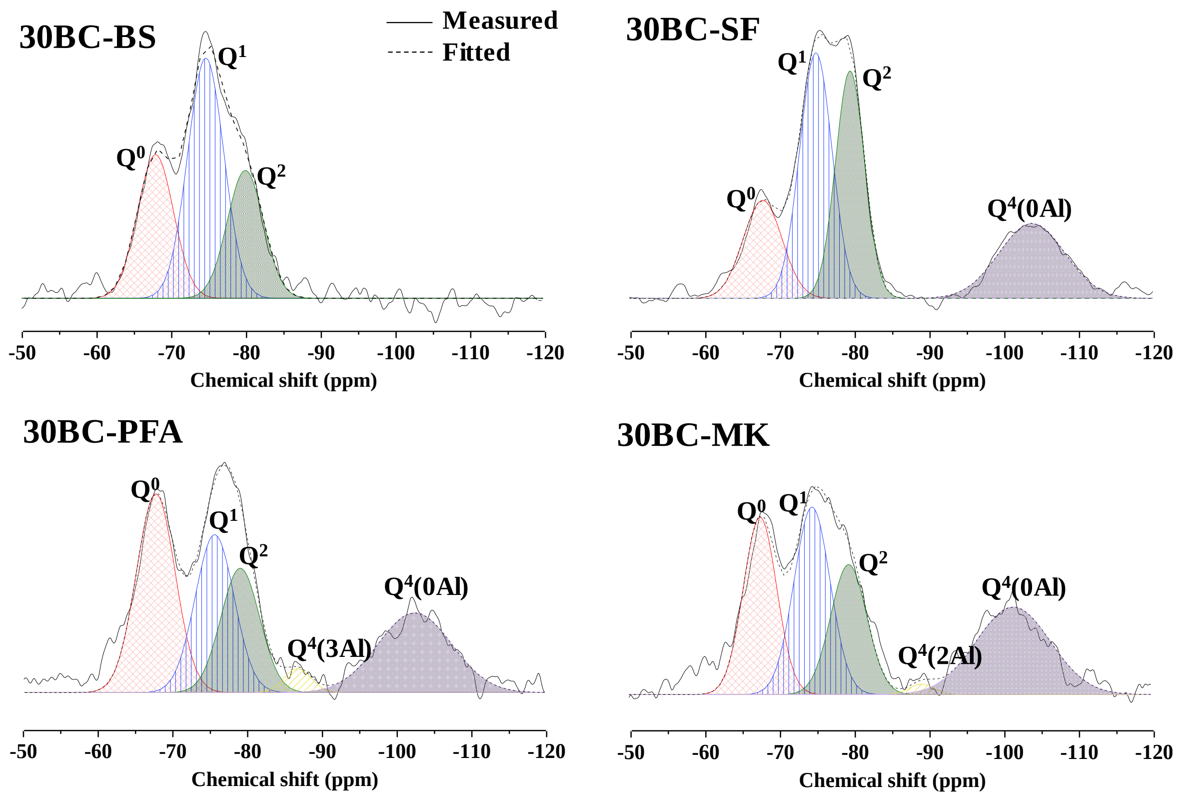

Figure 5.6. ^{29}Si NMR spectra for the 28-d biochar mortar with SCMs incorporation.

5.3.3 Microstructure and mechanical properties of the biochar mortar

BSE images (Figure 5.7) show that the biochar replacement facilitated the cement hydration but unavoidably introduced certain amount of microcracks and pores. In the control, the bright grey area (high density) occupying the majority of the image corresponded to unreacted C_2S and C_3S. The dark grey area in the control represented C-S-H gel, whereas the honeycombed phase in 10BC sample represented biochar pores. The bright grey area decreased with increasing substitution of aggregate by biochar (Figure 5.7a), reflecting that the presence of biochar facilitated the transformation from unreacted clinker to cement hydrates. However, some microcracks and pores might cause a negative effect on mechanical strength. As shown in Figure 5.7b, the light grey particles with corner angles were GGBS and the round particles were PFA. The dark grey area in the 30BC-SF and 30BC-MK samples were the mixtures of hydrates and unreacted SF or MK particles. After the SCMs incorporation, the surface became denser, which might benefit the mechanical properties.

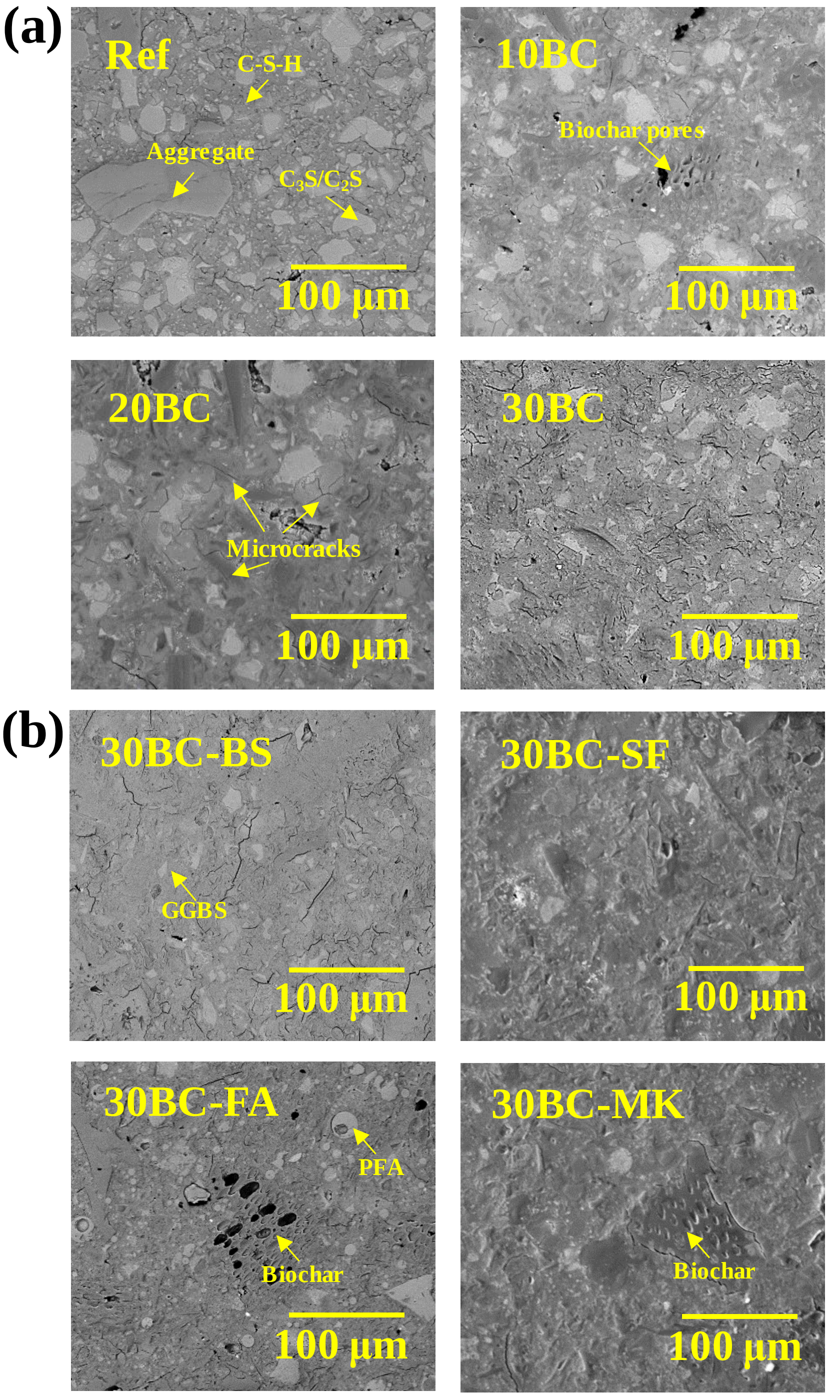

Figure 5.7. BSE images of the 28-d biochar mortar.

X-ray CT scan images (Figure 5.8) indicate that the biochar incorporation decreased the content of unreacted clinker but increased the porosity of the mortar. As shown in Figure 5.8, the unreacted cement clinker (including C_2S, C_3S and C_3A), aggregate, biochar, air pore, and interfacial transition zone (ITZ) could be observed in the horizontal slice and side images. Compared to the control, the presence of biochar significantly reduced the quantity of unreacted cement clinkers (highlighted in yellow). The unreacted cement clinker contents of the control, 30BC, and 30BC-MK were 16.0%, 2.5%, and 2.8%, respectively, which again echoed the higher cement hydration degree of the biochar-augmented samples. Furthermore, the porous ITZ could be easily observed in the control but not in the biochar-augmented samples. This suggests that biochar facilitated the formation of hydration products that could fill in the porous ITZ. Therefore, the wall effect between the cement and aggregate was reduced, and a densified microstructure could be developed in the biochar-augmented mortar. As shown in the pore distribution figures, most of the connected pores of the control were 13.08-16.34 mm in diameter. It is noted that the connected pores would be considered as one pore in the X-ray CT scan and the connected pores with different pore diameters were highlighted in different colors. After the biochar incorporation, the blue parts (in a range of 0.02-3.24 mm) increased remarkably, reflecting that the pore diameter in biochar-augmented mortar was reduced. With the increased formation of cement hydration products, part of the connected pores became disconnected. But the introduction of biochar with average pore diameter of 5.24 nm (Table 5.2) inevitably increased the porosity and the content of capillary pores. Compared to the 30BC sample (35.7% porosity), the porosity of 30BC-MK was reduced to 26.1% and the maximum pore diameter of the connected pores was reduced to 11.27 mm, suggesting the importance of pore structure densification by promoting the formation of additional hydration products with the support of selected SCMs (e.g., MK).

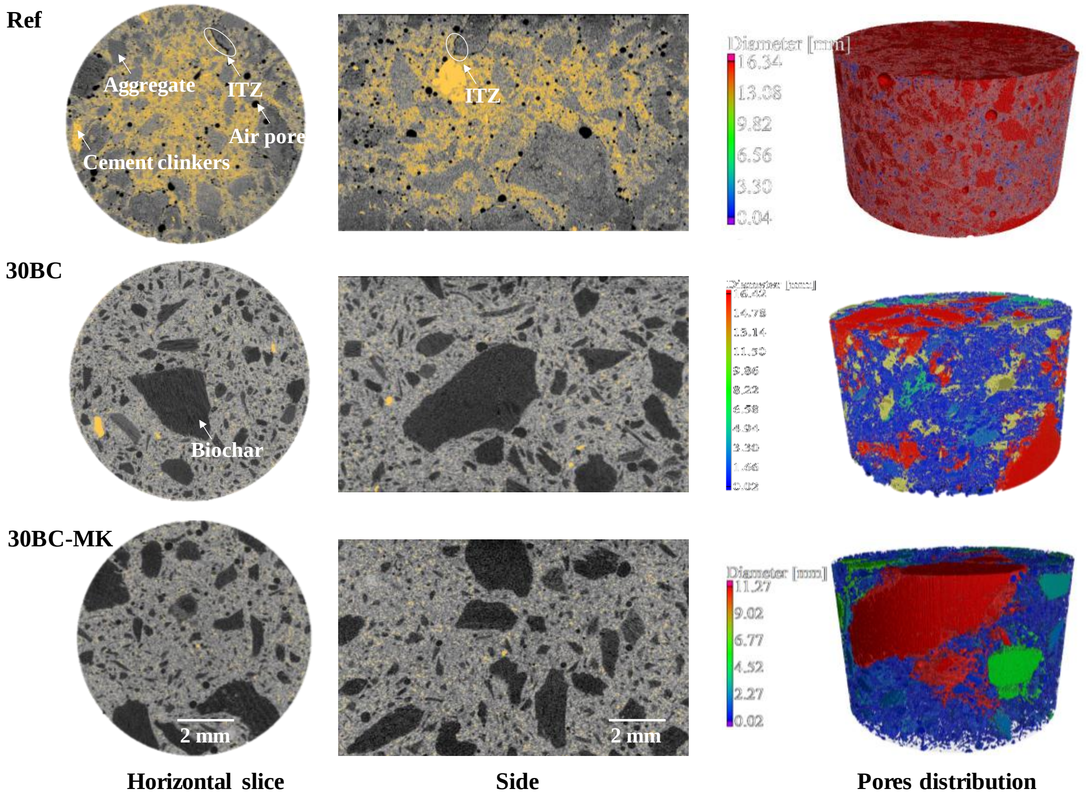

Figure 5.8. X-ray CT scan images of the 28-d biochar mortar (cement clinkers were highlighted in yellow color).

Compressive strength results (Figure 5.9) demonstrate that the incorporation of SCMs enhanced the strength of the biochar block, but excessive addition of biochar had negative effect on the strength of the biochar block. All the mixtures successfully fulfilled the strength requirement of 7 MPa for partition block (BS EN 771-3, 2011), and the compressive strength of 30BC (10.3 MPa) was 28.3% higher than the requirement. The compressive strength decreased with the increasing addition of biochar, which was attributed to the increase in the total porosity although biochar incorporation improved cement hydration. With the incorporation of SF and MK, the 28-d strength could increase by 17.9% and 27.5%, respectively, compared to the 30BC samples. This important strength enhancement was a result of the additional formation of cement hydrates including C-S-H gel, C-A-S-H gel, AFt, AFm phases, as evidenced earlier by the TGA, XRD, and NMR analyses. In comparison, with the replacement of 30 wt.% cement by GGBS and PFA, the 3-d strength was lower than the 30BC samples due to relatively low hydration at the early age, but the 28-d strength achieved comparable values owing to pozzolanic reaction in the later stage. Among these SCMs, the incorporation of SF and MK exhibited notable improvement in the mechanical strength of the biochar-augmented concrete.

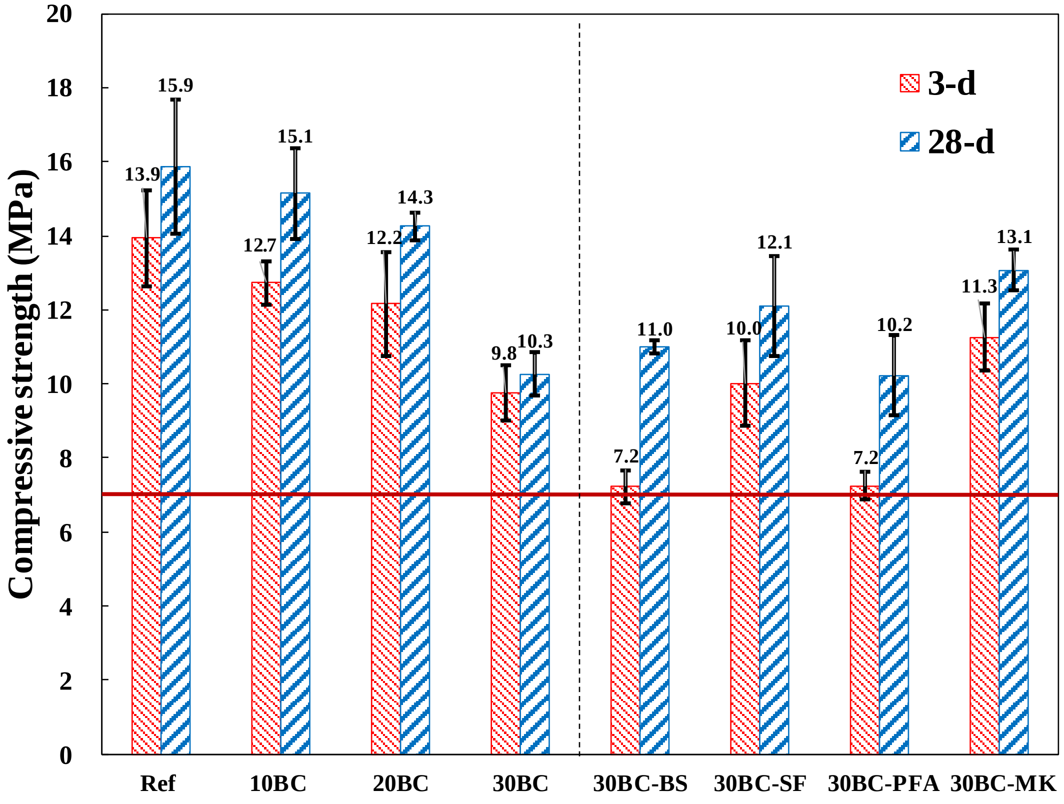

Figure 5.9. Compressive strength of the 3-d and 28-d biochar blocks (red line at 7 MPa: the required strength for partition blocks).

5.3.4. LCA and CBA of the biochar blocks

The LCA results show that the biochar incorporation significantly reduced CO_2

emissions and the combined use of SCMs further achieved carbon-negative concrete production. The results indicate that OPC was responsible for the largest part of CO_2 emissions (i.e., 30 wt.% OPC emitted 408.0 kg CO_2 $tonne^{-1}$ due to direct CO_2 emissions (decomposition of limestone) and indirect CO_2 emissions (burning of fossil fuels) (Zhang et al., 2014). Biochar contributed to the majority of carbon sequestration that 10 wt.% dosage of biochar could sequester 119.1 kg CO_2 $tonne^{-1}$. The use of recycled aggregate also eliminated the landfill disposal of construction waste (concrete) (Cui et al., 2016) and hence its total carbon footprint was relatively low. Compared to the overall CO_2 emissions of the control (421 kg CO_2 $tonne^{-1}$), the value of the 30BC sample was only 58.1 kg CO_2 $tonne^{-1}$ (i.e., 86.2% reduction). Furthermore, when 30 wt.% cement was replaced by the selected SCMs, the biochar blocks could successfully become carbon negative. The type of SCMs did not significantly influence the final carbon footprint, ranging from -59 to -65 kg CO_2 $tonne^{-1}$, which was ascribed to the comparable inputs and outputs for the SCMs application (Chen et al., 2010; Ruan et al., 2017). Therefore, the 30BC-MK sample with the best mechanical properties could sequester 59 kg CO_2 $tonne^{-1}$ of biochar block production.

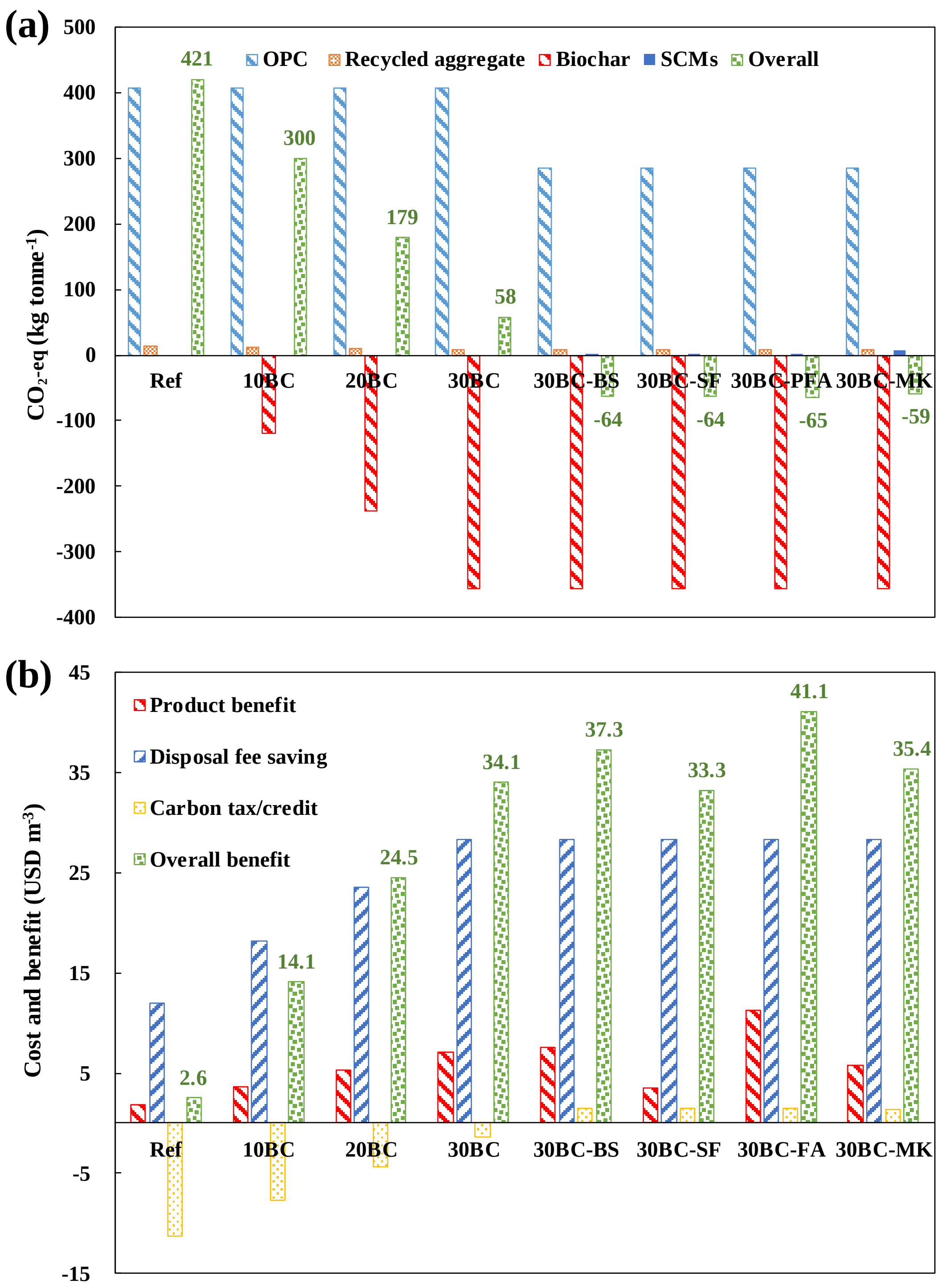

Figure 5.10. (a) carbon footprint and (b) cost and benefit of biochar blocks.

The CBA of the biochar blocks (Figure 5.10b) was calculated based on the local market price and quotation from the regional largest e-commerce platform (Alibaba et al., 2021). Calculation details and each component of the cost, benefit, disposal fee saving, and carbon tax/credit are shown in Table S5.1 and S5.2. The product benefit, even without accounting for the disposal fee saving, was positive; and the material cost of OPC was the predominant cost. Due to CO_2 emissions from the production of the control mixture, a substantial amount of carbon tax was incurred and 81.3% of the overall profits would be consumed. In contrast, the application of biochar could substantially reduce CO_2 emissions and save a great amount of carbon tax, the increasing substitution of aggregate by biochar could significantly increase the overall benefit. Compared to the control, the incorporation of 30 wt.% BC reduced the carbon tax by 88.5% and the carbon-negative mixtures could even generate additional profits from the carbon credit. More importantly, compared to the carbon price ~50 USD tonne^{-1} in the US and the carbon price ~70 USD tonne^{-1} in Europe, the current carbon price in China (i.e., 13.5 USD tonne^{-1}) still has a tremendous upside in the coming years (Carbon trading et al., 2021; USBI 2021). The carbon price range of 40 to 80 USD tonne^{-1} would be needed to meet the target of limiting the global temperature increase to 2 °C goal of the Paris Agreement, , and the carbon price would rise further to achieve the 1.5 °C goal (World Bank 2021). The critical impact of carbon tax/credit for the overall benefit is increasing with the worldwide implementation of carbon neutrality policies.

In addition, the application of yard waste-derived biochar could save a significant amount of the landfill disposal fee of yard waste (for example, 25.6 USD tonne^{-1} of construction waste in Hong Kong) (HK EPD 2021), which also represents a major contribution to the overall benefit. The replacement of cement by SCMs could further increase the overall benefit. For instance, the overall benefit of 30BC-MK sample reached 35.4 USD m^{-3}, which concurrently produced the best mechanical properties and environmental performance. The overall benefit of 30BC-FA achieved 41.1 USD m^{-3}, which was the highest value among these mixtures as the cost of PFA (including transportation fee) was only 33.8% of OPC. These results show that the application of biochar in partition block could not only reduce the carbon footprint but also save a great amount of material cost, carbon tax, and waste disposal fee, thereby yielding a high economic profit in the new era of carbon neutrality.

5.4 Conclusions

This study developed an innovative approach to extend the use of yard waste-derived biochar as the aggregate for producing biochar-augmented carbon-negative concrete. The results demonstrated that the replacement of recycled aggregate by biochar improved the cement hydration via internal curing of biochar-regulated water release. The increasing proportion of biochar substitution promoted the degree of cement hydration and enhanced the polymerization degree of C-S-H gel, whereas it also increased the porosity of cement composites. The compressive strength of concrete with 30 wt.% biochar achieved 10.3 MPa, fulfilling the strength requirement of the partition block (7 MPa). Further substitution of 30 wt.% cement by different SCMs displayed distinctive influences on the cement hydration process of biochar-augmented concrete. In particular, MK could further increase the mechanical properties of biochar-augmented concrete via the time-dependent pozzolanic reaction. The life cycle assessment confirmed that every 10 wt.% of biochar incorporation significantly reduced the total CO_2 emissions, and the biochar block with 30 wt.% biochar and SCMs could be successfully transformed into a carbon-negative product, sequestering 59 to 65 kg CO_2 $tonne^{-1}$. The cost-benefit analysis demonstrated that the production of biochar block could generate notable overall economic profit. It is noteworthy that our biochar-augmented carbon-negative concrete will become increasingly competitive, as the carbon tax around the world still has a huge upside potential after the implementation of carbon neutrality policies. In view of the comprehensive performance, the 30BC-MK can be the recommended design for biochar-augmented carbon-negative concrete. In the future studies, the influence of various biochar properties, durability in field-relevant environmental conditions, as well as sustainability metrics and value-added features of biochar-augmented concrete products should be further substantiated.

CHAPTER 6. Conclusions and perspectives

This study proposed the application of biochar in sustainable cement composite and carbon-negative concrete. The roles of biochar in OPC, low-carbon magnesium oxide cement systems were elucidated. Moreover, accelerated CO_2 curing and incorporation of supplementary cementitious materials were also applied to improve the properties of biochar cement composite. The reaction mechanisms of different cement composites were unraveled by conducting cement chemistry and microstructure characterization. Furthermore, life cycle assessment, cost and benefit analysis were conducted to confirm the environmental and economic benefits of biochar cement composite. The major conclusions of this study are recapped as follows:

1. Chapter 3 elaborated the roles of rice husk-derived and yard waste-derived biochar in cement system and evaluated the application of biochar in the cement-based S/S of MSWIFA. Experimental results indicated that the incorporation of biochar facilitated the cement hydration and promoted the formation of hydration products, due to the internal curing effect of biochar. Comparing the two types of biochars, RBC was more effective for promoting the generation of C-S-H than YBC, because activated-Si in RBC could react with CH to form additional C-S-H via pozzolanic reaction. The 2 wt.% biochar addition enhanced the compressive strength, whereas the addition of 5 wt.% and 10 wt.% biochar slightly decreased the compressive strength due to the high porosity of biochar, especially for more porous YBC. The S/S process of MSWIFA confirmed that both RBC and YBC addition improved the immobilization of PTEs in MSWIFA. The 20 or 30 wt.% biochar-enhanced cement binders could effectively stabilize/solidify MSWIFA, and S/S products fulfilled the

requirements for reuse as fill material or non-load-bearing block, respectively. In summary, this research demonstrated that biochar could be a promising additive for cement-based S/S of MSWIFA and reduction of carbon footprint.

2. Chapter 4 articulated the roles of biochar in MC-based pastes and evaluated the synergistic effect of biochar and CO_2 curing on promoting the hydration and carbonation of MC and MP systems. According to the results of XRD and TGA analyses, the incorporation of 2 wt.% biochar slightly facilitated hydration of MC system during air curing, whereas it could significantly promote the hydration and carbonation of MP-based pastes. In this study, CO_2 gasification biochar (CO_2 BC) was more effective than air gasification biochar (Air BC), possibly due to the larger water storage capacity in CO_2 BC for internal curing and rehydration of unreacted cement. Moreover, CO_2 curing accelerated the carbonation of MC and MP pastes, and the incorporation of biochar, especially CO_2 BC, displayed a synergism for the accelerated carbonation, because porous biochar could provide channels for CO_2 diffusion and intensive carbonation. Therefore, porous biochar together with CO_2 curing could be a promising and green approach for reducing carbon footprint and enhancing the properties of cement-based composites.

4. Chapter 6 developed an innovative approach to extend the use of yard waste-derived biochar as the aggregate for producing biochar-augmented carbon-negative concrete. The results demonstrated that the replacement of recycled aggregate by biochar improved the cement hydration via internal curing of biochar-regulated water release. The increasing proportion of biochar substitution promoted the degree of cement hydration and enhanced the polymerization degree of C-S-H gel,

whereas it also increased the porosity of cement composites. The compressive strength of concrete with 30 wt.% SSD biochar achieved 10.3 MPa, fulfilling the strength requirement of the partition block (7 MPa). Further substitution of 30 wt.% cement by different SCMs displayed distinctive influences on the cement hydration process of biochar-augmented concrete. In particular, MK could further increase the mechanical properties of biochar-augmented concrete via the time-dependent pozzolanic reaction. The life cycle assessment confirmed that every 10 wt.% of SSD biochar incorporation significantly reduced the total CO_2 emissions, and the biochar block with 30 wt.% SSD biochar and SCMs could be successfully transformed into a carbon-negative product, sequestering 59 to 65 kg CO_2 tonne^{-1}. The cost-benefit analysis demonstrated that the production of biochar block could generate notable overall economic profit. It is noteworthy that our biochar-augmented carbon-negative concrete will become increasingly competitive, as the carbon tax around the world still has a huge upside potential after the implementation of carbon neutrality policies. In view of the comprehensive performance, the 30BC-MK can be the recommended design for biochar-augmented carbon-negative concrete.

In future studies, the effects of biochar with different characteristics (surface area, pore size distributions, element composition, etc.) on different cement binders (e.g., MC, MPC, Alkali activated cement) should be systematically assessed. More value-added features can be developed to expand the application of biochar-cement composite. In addition, the durability in field-relevant environmental conditions (long-time strength degradation, chloride permeability, etc.), as well as sustainability metrics of biochar cement composites should be further substantiated.

References

Abbas, R., Khereby, M.A., Ghorab, H.Y., Elkhoshkhany, N., 2020. Preparation of geopolymer concrete using Egyptian kaolin clay and the study of its environmental effects and economic cost. Clean Technol. Environ. Policy 22, 669–687. doi:10.1007/s10098-020-01811-4

Ahmad, M.R., Chen, B., Duan, H., 2020. Improvement effect of pyrolyzed agro-food biochar on the properties of magnesium phosphate cement. Sci. Total Environ. 718. https://doi.org/10.1016/j.scitotenv.2020.137422.

Akhtar, A., Sarmah, A.K., 2018. Novel biochar-concrete composites: Manufacturing, characterization and evaluation of the mechanical properties. Sci. Total Environ. 616–617. https://doi.org/10.1016/j.scitotenv.2017.10.319.

Alibaba, 2021. https://www.alibaba.com (Accessed: 08. Sep. 2021).

Al-Tabbaa, A. Reactive magnesia cement. In: Eco-efficient Concrete; 2013, 523-543.

ASTM C1761/C1761M-17, Standard specification for lightweight aggregate for internal curing of concrete, ASTM International, West Conshohocken, PA, 2017.

Ataie, F.F., Riding, K.A., 2016. Influence of agricultural residue ash on early cement hydration and chemical admixtures adsorption. Constr. Build. Mater. 106, 274–281. doi:10.1016/j.conbuildmat.2015.12.091

Azzi, E.S., Karltun, E., Sundberg, C., 2019. Prospective life cycle assessment of large-scale biochar production and use for negative emissions in stockholm. Environ. Sci. Technol. 53, 8466–8476. doi:10.1021/acs.est.9b01615.

BBC, Climate change: China aims for carbon neutrality by 2060. 2020a, Retrieved from https://www.bbc.com/news/science-environment-54256826 (Accessed: 22. June. 2021).

BBC. Climate change: EU leaders set 55% target for CO_2 emissions cut. 2020b, Retrieved from https://www.bbc.com/news/world-europe-55273004 (Accessed: 11. Dec. 2020)

Bertos, M.F., Simons, S.J.R., Hills, C.D., Carey, P.J. A review of accelerated carbonation technology in the treatment of cement-based materials and sequestration of CO_2. J. Hazard Mater. 2004, 112, 193-205, doi.org/10.1016/j.jhazmat.2004.04.019.

Brewer, C.E., Chuang, V.J., Masiello, C.A., Gonnermann, H., Gao, X., Dugan, B., Driver, L.E., Panzacchi, P., Zygourakis, K., Davies, C.A., 2014. New approaches to measuring biochar density and porosity. Biomass and Bioenergy. Res. 66, 176-185. https://doi.org/10.1016/j.biombioe.2014.03.059

BS EN 12390, Testing hardened concrete compressive strength of test specimens, British Standards Institution, London, UK, 2009.

BS EN 771-3, Specification for masonry units. Aggregate concrete masonry units (dense and light-weight aggregates), British Standards Institution, London, UK, 2011.

Cao, F.; Liu, Y.; Yan, P. Properties and Mechanism of the Compound MgO Expansive agent (CMEA) Produced by Calcining the Mixture of Dolomite and Serpentine Tailings. Constr. Build. Mater. 2021, 277, 122331, doi.org/10.1016/j.conbuildmat.2021.122331.

Carbon trading, Retrieved from http://www.tanpaifang.com/tanjiaoyi/2021/0918/79691.html (Accessed: 20. Sep. 2021).

Cheah, C.B., Chung, K.Y., Ramli, M., Lim, G.K., 2016. The engineering properties and microstructure development of cement mortar containing high volume of inter-grinded GGBS and PFA cured at ambient temperature. Constr. Build. Mater.

Res. 122, 683-693. https://doi.org/10.1016/j.conbuildmat.2016.06.105

Chen, C., Habert, G., Bouzidi, Y., Jullien, A., Ventura, A., 2010. LCA allocation procedure used as an incitative method for waste recycling: An application to mineral additions in concrete. Resour. Conserv. Recycl. 54, 1231–1240. doi:10.1016/j.resconrec.2010.04.001.

Chen, L., Wang, L., Cho, D.W., Tsang, D.C.W., Tong, L., Zhou, Y., Yang, J., Hu, Q., Poon, C.S., 2019. Sustainable stabilization/solidification of municipal solid waste incinerator fly ash by incorporation of green materials. J. Clean. Prod. 222, 335–343. doi:10.1016/j.jclepro.2019.03.057.

Chen, L., Wang, L., Tsang, D.C.W., Mechtcherine, V., Poon, C.S., 2020. Efficacy of green alternatives and carbon dioxide curing in reactive magnesia cement-bonded particleboards. J. Clean. Prod. 258. doi:10.1016/j.jclepro.2020.120997.

Chen, L., Wang, L., Zhang, Y., Ruan, S., Mechtcherine, V., Tsang, D.C.W., 2022. Roles of biochar in cement-based stabilization/solidification of municipal solid waste incineration fly ash. Chem. Eng. J. 430. doi:10.1016/j.cej.2021.132972.

Chen, L., Wang, Y.S., Wang, L., Zhang, Y., Li, J., Tong, L., Hu, Q., Dai, J.G., Tsang, D.C.W., 2021. Stabilisation/solidification of municipal solid waste incineration fly ash by phosphate-enhanced calcium aluminate cement. J. Hazard. Mater. 408. doi:10.1016/j.jhazmat.2020.124404.

Cosentino, I., Restuccia, L., Ferro, G.A., Tulliani, J.M., 2019. Type of materials, pyrolysis conditions, carbon content and size dimensions: The parameters that influence the mechanical properties of biochar cement-based composites. Theor. Appl. Fract. Mech. 103. https://doi.org/10.1016/j.tafmec.2019.102261.

Cui, D, Research on optimization of environmental load of concrete and its waste treatment based on LCA, Beijing University of Technology, 2016.

Das, O., Sarmah, A.K., Bhattacharyya, D., 2015. Structure-mechanics property relationship of waste derived biochars. Sci. Total Environ. Res. 538, 611-620. https://doi.org/10.1016/j.scitotenv.2015.08.073.

Dissanayake, P. D.; Choi, S. W.; Igalavithana, A. D.; Yang, X.; Tsang, D. C. W.; Wang, C. H.; Kua, H. W.; Lee, K. B.; Ok, Y. S. Sustainable gasification biochar as a high efficiency adsorbent for CO_2 capture: a facile method to designer biochar fabrication. Renew. Sustain. Energy Rev. 2020, 124, 109785, doi.org/10.1016/j.rser.2020.109785.

Dissanayake, P.D.; You, S.; Igalavithana, A.D.; Xia, Y.; Bhatnagar, A.; Gupta, S.; Kua, H.W.; Kim, S.; Kwon, J.H.; Tsang, D.C.W.; Ok, Y.S. Biochar-based adsorbents for carbon dioxide capture: A critical review. Renew. Sust. Energ. Rev., 2020, 119, 109582, doi.org/10.1016/j.rser.2019.109582.

Dixit, A., Gupta, S., Pang, S.D., Kua, H.W., 2019. Waste Valorisation using biochar for cement replacement and internal curing in ultra-high performance concrete. J. Clean. Prod. 238. https://doi.org/10.1016/j.jclepro.2019.117876.

Dixit, A., Verma, A., Pang, S.D., 2021. Dual waste utilization in ultra-high performance concrete using biochar and marine clay. Cem. Concr. Compos. 120, 104049. https://doi.org/10.1016/j.cemconcomp.2021.104049.

Dong, H.; Yang, E. H.; Unluer, C.; Jin, F.; Al-Tabbaa, A. Investigation of the properties of MgO recovered from reject brine obtained from Desalination Plants. J. Clean. Prod. 2018, 196, 100–108, doi.org/10.1016/j.jclepro.2018.06.032.

Dong, X, Analysis of environmental performance related to the recycling of construction waste (In Chinese), Shandong University of Science and Technology, 2011.

Fan, C., Wang, B., Zhang, T., 2018. Review on cement stabilization/solidification of municipal solid waste incineration fly ash. Adv. Mater. Sci. Eng. doi:10.1155/2018/5120649.

GB 34330, Identification standards for solid wastes-general rules. Ministry of Ecology and Environment, China, 2017.

Geng, Y., Wang, Z., Shen, L., Zhao, J., 2019. Calculating of CO 2 emission factors for Chinese cement production based on inorganic carbon and organic carbon. J. Clean. Prod. 217, 503–509. doi:10.1016/j.jclepro.2019.01.224.

Goodarzi, A.R., Akbari, H.R., Salimi, M., 2016. Enhanced stabilization of highly expansive clays by mixing cement and silica fume. Appl. Clay Sci. 132–133, 675–684. doi:10.1016/j.clay.2016.08.023.

Guo, B., Tan, Y., Wang, L., Chen, L., Wu, Z., Sasaki, K., Mechtcherine, V., Tsang, D.C.W., 2021. High-efficiency and low-carbon remediation of zinc contaminated sludge by magnesium oxysulfate cement. J. Hazard. Mater. 408. doi:10.1016/j.jhazmat.2020.124486.

Guo, M., Murphy, R.J., 2012. LCA data quality: Sensitivity and uncertainty analysis. Sci. Total Environ. 435–436, 230–243. doi:10.1016/j.scitotenv.2012.07.006.

Gupta, S., Kua, H.W., Koh, H.J., 2018a. Application of biochar from food and wood waste as green admixture for cement mortar. Sci. Total Environ. 619–620, 419–435. doi:10.1016/j.scitotenv.2017.11.044.

Gupta, S., Kua, H.W., Pang, S.D., 2018b. Biochar-mortar composite: Manufacturing, evaluation of physical properties and economic viability. Constr. Build. Mater. Res. 167, 874-889. https://doi.org/10.1016/j.conbuildmat.2018.02.104.

Gupta, S.; Kua, H. W.; Low, C. Y., 2018c. Use of biochar as carbon sequestering additive in cement mortar. Cem. Concr. Compos. 2018, 87, 110–129, doi.org/10.1016/j.cemconcomp.2017.12.009.

Gupta, S., Kua, H.W., 2019. Carbonaceous micro-filler for cement: Effect of particle size and dosage of biochar on fresh and hardened properties of cement mortar. Sci. Total Environ. Res. 662, 952-962. https://doi.org/10.1016/j.scitotenv.2019.01.269.

Gupta, S., Kua, H.W., 2020a. Application of rice husk biochar as filler in cenosphere modified mortar: Preparation, characterization and performance under elevated temperature. Constr. Build. Mater. 253. doi:10.1016/j.conbuildmat.2020.119083.

Gupta, S., Palansooriya, K.N., Dissanayake, P.D., Ok, Y.S., Kua, H.W., 2020b. Carbonaceous inserts from lignocellulosic and non-lignocellulosic sources in cement mortar: Preparation conditions and its effect on hydration kinetics and physical properties. Constr. Build. Mater. 264. https://doi.org/10.1016/j.conbuildmat.2020.120214.

Gupta, S., Krishnan, P., Kashani, A., Kua, H.W., 2020c. Application of biochar from coconut and wood waste to reduce shrinkage and improve physical properties of silica fume-cement mortar. Constr. Build. Mater. 262. doi:10.1016/j.conbuildmat.2020.120688.

Gupta, S., Tulliani, J.M., Kua, H.W., 2022. Carbonaceous admixtures in cementitious building materials: Effect of particle size blending on rheology, packing, early age properties and processing energy demand. Sci. Total Environ. 807. doi:10.1016/j.scitotenv.2021.150884

Hay, R.; Celik, K. Hydration, carbonation, strength development and corrosion resistance of reactive mgo cement-based composites. Cem. Concr. Res. 2020, 128, 105941, doi.org/10.1016/j.cemconres.2019.105941.

He, M., Xiong, X., Wang, L., Hou, D., Bolan, N.S., Ok, Y.S., Rinklebe, J., Tsang, D.C.W., 2021. A critical review on performance indicators for evaluating soil biota and soil health of biochar-amended soils. J. Hazard. Mater. 414. https://doi.org/10.1016/j.jhazmat.2021.125378

He, P., Hossain, M.U., Poon, C.S., Tsang, D.C.W., 2019. Mechanical, durability and environmental aspects of magnesium oxychloride cement boards incorporating waste wood. J. Clean. Prod. doi:10.1016/j.jclepro.2018.10.015.

Hepburn, C.; Adlen, E.; Beddington, J.; Carter, E. A.; Fuss, S.; Mac Dowell, N.; Minx, J. C.; Smith, P.; Williams, C. K. The technological and economic prospects for CO_2 utilization and removal. Nature. 2019, 575, 87-97, doi.org/10.1038/s41586-019-1681-6.

Hewlett, P.C., Liska, M., 2019. Lea's chemistry of cement and concrete, Lea's Chemistry of Cement and Concrete. doi:10.1016/C2013-0-19325-7.

HJ 1134, Technical specification for pollution control of fly-ash from municipal solid waste incineration. Ministry of Environmental Protection, China, 2020.

HK EPD 2021. Construction waste disposal charging scheme. Retrieved from https://www.bbc.com/news/world-europe-55273004 (Accessed: 08. Sep. 2021).

HK EPD, Practice guide for investigation and remediation of contaminated land, Environmental Protection Department, Hong Kong, 2011.

IPCC. Summary for Policymakers. In: Global Warming of 1.5°C; Chapter 4: Strengthening and implementing the global response. 2019, Retrieved from https://www.ipcc.ch/site/assets/uploads/sites/2/2019/05/SR15_Chapter4_Low_Res.pdf

ISO14040, Environmental management: life cycle assessment—principles and frameworkment. International Standards Organization, p. 23, Geneva, Switzerland, 2006.

J. W. Gaskin, C. Steiner, K. Harris, K. C. Das, B. Bibens, 2008. Effect of Low-

Temperature Pyrolysis Conditions on Biochar for Agricultural Use. Trans. ASABE. Res. 51, 2061-2069. https://doi.org/10.13031/2013.25409.

Jeong, Y.J., Youm, K.S., Yun, T.S., 2018. Effect of nano-silica and curing conditions on the reaction rate of class G well cement exposed to geological CO_2-sequestration conditions. Cem. Concr. Res. 109, 208–216. doi:10.1016/j.cemconres.2018.05.001.

Karade, S.R. 2010. Cement-bonded composites from lignocellulosic wastes. Constr. Build. Mater. 24, 1323-1330.

Khushnood, R.A., Ahmad, S., Restuccia, L., Spoto, C., Jagdale, P., Tulliani, J.M., Ferro, G.A., 2016. Carbonized nano/microparticles for enhanced mechanical properties and electromagnetic interference shielding of cementitious materials. Front. Struct. Civ. Eng. Res. 10, 209-213. https://doi.org/10.1007/s11709-016-0330-5.

Kim, J.J., Rahman, M.K., Reda Taha, M.M., 2012. Examining microstructural composition of hardened cement paste cured under high temperature and pressure using nanoindentation and 29Si MAS NMR. Appl. Nanosci. 2, 445–456. doi:10.1007/s13204-012-0058-z.

Krakowiak, K.J., Thomas, J.J., Musso, S., James, S., Akono, A.T., Ulm, F.J., 2015. Nano-chemo-mechanical signature of conventional oil-well cement systems: Effects of elevated temperature and curing time. Cem. Concr. Res. 67, 103–121. doi:10.1016/j.cemconres.2014.08.008.

Lapeyre, J., Kumar, A., 2018. Influence of pozzolanic additives on hydration mechanisms of tricalcium silicate. J. Am. Ceram. Soc. Res. 101, 3557-3574. https://doi.org/10.1111/jace.15518.

Le Saout, G., Lécolier, E., Rivereau, A., Zanni, H., 2006. Chemical structure of cement aged at normal and elevated temperatures and pressures: Part I. Class G oilwell cement. Cem. Concr. Res. 36, 71–78. doi:10.1016/j.cemconres.2004.09.018.

Lehne, J., Preston, F., 2018. Making Concrete Change; Innovation in Low-carbon Cement and Concrete. Chatham House Rep. Res. 1-122 .

Leng, L., Huang, H., Li, H., Li, J., Zhou, W., 2019. Biochar stability assessment methods: A review. Sci. Total Environ. doi:10.1016/j.scitotenv.2018.07.402.

Li, C., Cui, S., Nie, Z., Gong, X., Wang, Z., Itsubo, N., 2015. The LCA of portland cement production in China. Int. J. Life Cycle Assess. 20, 117–127. doi:10.1007/s11367-014-0804-4.

Li, S., 2016. Microstructure and composition characterisation of three 20-year-old GGBS-OPC blended pastes. Constr. Build. Mater. 123, 226–234. doi:10.1016/j.conbuildmat.2016.06.057.

Li, W., Sun, Y., Huang, Y., Shimaoka, T., Wang, H., Wang, Y. nan, Ma, L., Zhang, D., 2019. Evaluation of chemical speciation and environmental risk levels of heavy metals during varied acid corrosion conditions for raw and solidified/stabilized MSWI fly ash. Waste Manag. 87, 407–416. doi:10.1016/j.wasman.2019.02.033

Liu, Y., Dai, Q., Jin, X., Dong, X., Peng, J., Wu, M., Liang, N., Pan, B., Xing, B., 2018. Negative Impacts of Biochars on Urease Activity: High pH, Heavy Metals, Polycyclic Aromatic Hydrocarbons, or Free Radicals? Environ. Sci. Technol. 52, 12740–12747. doi:10.1021/acs.est.8b00672.

Liu, Y., Sun, Y., Wan, Z., Jing, F., Li, Z., Chen, J., Tsang, D.C.W., 2021. Tailored design of food waste hydrochar for efficient adsorption and catalytic degradation of refractory organic contaminant. J. Clean. Prod. 310. doi:10.1016/j.jclepro.2021.127482

Lu, B.; Shi, C.; Hou, G. Strength and microstructure of CO_2 cured low-calcium clinker.

Constr. Build. Mater. 2018, 188, 417–423, doi.org/10.1016/j.conbuildmat.2018.08.134.

MEE, No waste city. Ministry of Ecology and Environment of the people`s Republic of China. https://www.mee.gov.cn/home/ztbd/2020/wfcsjssdgz/ (Accessed: 22. June. 2021).

Merchant, I.J., Macphee, D.E., Chandler, H.W., Henderson, R.J., 2001. Toughening cement-based materials through the control of interfacial bonding. Cem. Concr. Res. 31, 1873-1880. https://doi.org/10.1016/S0008-8846(01)00500-2.

Messaoudene, I. Jauberthie, R. Marble filler: Does it retard the dissolution of cement constituents?, ISRN Mater. Sci. 2011 (2011) 1–5, https://doi.org/10.5402/2011/695123.

Mo, L., Deng, M., Tang, M., Al-Tabbaa, A., 2014. MgO expansive cement and concrete in China: Past, present and future. Cem. Concr. Res. 57, 1-2. https://doi.org/10.1016/j.cemconres.2013.12.007

Mo, L., Zhang, F., Deng, M., Panesar, D.K., 2016. Effectiveness of using CO_2 pressure to enhance the carbonation of Portland cement-fly ash-MgO mortars. Cem. Concr. Compos. Res. 70, 78-85. https://doi.org/10.1016/j.cemconcomp.2016.03.013

Mo, L.; Panesar, D. K. Effects of Accelerated Carbonation on the Microstructure of Portland Cement Pastes Containing Reactive MgO. Cem. Concr. Res. 2012, 42 (6), 769–777, Doi.org/10.1016/j.cemconres.2012.02.017.

Moon, D.H., Park, S.S., Kang, S.P., Lee, W., Park, K.T., Chun, D.H., Rhim, G.B., Hwang, S.M., Youn, M.H., Jeong, S.K., 2021. Determination of kinetic factors of CO_2 mineralization reaction for reducing CO_2 emissions in cement industry and verification using CFD modeling. Chem. Eng. J. 420. doi:10.1016/j.cej.2021.129420.

Moon, J., Reda Taha, M.M., Youm, K.S., Kim, J.J., 2016. Investigation of pozzolanic reaction in nanosilica-cement blended pastes based on solid-state kinetic models and 29SI MAS NMR. Materials (Basel). 9. doi:10.3390/ma9020099.

NBSC, China Statistical Yearbook of 2020, National Bureau of Statistics of China. Beijing, China, 2020.

Oliveira, F.R., Patel, A.K., Jaisi, D.P., Adhikari, S., Lu, H., Khanal, S.K., 2017. Environmental application of biochar: Current status and perspectives. Bioresour. Technol. Res. 246, 110-122. https://doi.org/10.1016/j.biortech.2017.08.122.

Onay, O., Gaines, A.F., Kockar, O.M., Adams, M., Tyagi, T.R., Snape, C.E., 2006. Comparison of the generation of oil by the extraction and the hydropyrolysis of biomass. Fuel. 85, 382-392. https://doi.org/10.1016/j.fuel.2005.06.014.

Pillai, R.G., Gettu, R., Santhanam, M., Rengaraju, S., Dhandapani, Y., Rathnarajan, S., Basavaraj, A.S., 2019. Service life and life cycle assessment of reinforced concrete systems with limestone calcined clay cement (LC3). Cem. Concr. Res. 118, 111–119. doi:10.1016/j.cemconres.2018.11.019.

Poppe, A.M., De Schutter, G., 2005. Cement hydration in the presence of high filler contents. Cem. Concr. Res. 35, 2290-2299. https://doi.org/10.1016/j.cemconres.2005.03.008.

Pulido-Novicio, L., Hata, T., Kurimoto, Y., Doi, S., Ishihara, S., Imamura, Y., 2001. Adsorption capacities and related characteristics of wood charcoals carbonized using a one-step or two-step process. J. Wood Sci. Res. 47, 48-57. https://doi.org/10.1007/BF00776645.

Quicker P, Biokohle Weber K. Herstellung, Eigenschaften und Verwendung von Biomassekarbonisaten. Wiesbaden: Springer Vieweg; 2016. http://dx.doi.org/10.1007/978-3-658-03689-8.

Rahla, K.M., Mateus, R., Bragança, L., 2019. Comparative sustainability assessment of binary blended concretes using Supplementary Cementitious Materials (SCMs) and Ordinary Portland Cement (OPC). J. Clean. Prod. 220, 445–459. doi:10.1016/j.jclepro.2019.02.010.

Rodier, L., Bilba, K., Onésippe, C., Arsène, M.A., 2019. Utilization of bio-chars from sugarcane bagasse pyrolysis in cement-based composites. Ind. Crops Prod. 141. doi:10.1016/j.indcrop.2019.111731Y. Qin, X. Pang, K. Tan and T. Bao, Cem. Concr. Compos., 2021, 119, 104022.

Roy, A., Stegemann, J.A., 2017. Nickel speciation in cement-stabilized/solidified metal treatment filtercakes. J. Hazard Mater. 321, 353-361.

Ruan, S., Unluer, C., 2017. Influence of supplementary cementitious materials on the performance and environmental impacts of reactive magnesia cement concrete. J. Clean. Prod. 159, 62–73. doi:10.1016/j.jclepro.2017.05.044.

Salem Al-Ahdal, B.M., Xiong, L.B., Tufail, R.F., 2018. Mechanical properties of concrete containing Fly Ash, Rice Husk Ash and Waste Glass Powder. Civ. Eng. J. 4, 1019. doi:10.28991/cej-0309153.

Samad, S., Shah, A., 2017. Role of binary cement including Supplementary Cementitious Material (SCM), in production of environmentally sustainable concrete: A critical review. Int. J. Sustain. Built Environ. Res. 6, 663-674. https://doi.org/10.1016/j.ijsbe.2017.07.003.

Sashidhar, P., Kochar, M., Singh, B., et al. (2020). Biochar for delivery of agri-inputs: current status and future perspectives. Sci. Total Environ. 703, 134892.

Scrivener, K. L.; John, V. M.; Gartner, E. M. Eco-efficient cements: potential economically viable solutions for a low-CO_2 cement-based materials industry. Cem. Concr. Res. 2018, 114, 2–26, doi.org/10.1016/j.cemconres.2018.03.015.

Scrivener, K., Martirena, F., Bishnoi, S., Maity, S., 2018. Calcined clay limestone cements (LC3). Cem. Concr. Res. doi:10.1016/j.cemconres.2017.08.017.

Shaheen, S.M., Niazi, N.K., Hassan, N.E.E., Bibi, I., Wang, H., Tsang, D.C.W., Ok, Y.S., Bolan, N., Rinklebe, J., 2019. Wood-based biochar for the removal of potentially toxic elements in water and wastewater: a critical review. Int. Mater. Rev. 64, 216–247. doi:10.1080/09506608.2018.1473096.

Shen, Y.; Li, X.; Yao, Z.; Cui, X.; Wang, C. H. CO_2 Gasification of woody biomass: experimental study from a lab-scale reactor to a small-scale autothermal Gasifier. Energy 2019, 170, 497–506, doi.org/10.1016/j.energy.2018.12.176.

Shen, Z., Zhang, Z., Zhang, M., Rinklebe, J., Ma, Y., Hou, D., 2021. Effect of production temperature and particle size of rice husk biochar on mercury immobilization and erosion prevention of a mercury contaminated soil. J. Hazard. Mater. 420. https://doi.org/10.1016/j.jhazmat.2021.126646.

Shi, C.; Wu, Z.; Cao, Z.; Ling, T. C.; Zheng, J. Performance of mortar prepared with recycled concrete aggregate enhanced by CO_2 and pozzolan slurry. Cem. Concr. Compos. 2018, 86, 130–138, doi.org/10.1016/j.cemconcomp.2017.10.013.

Skibsted, J., Andersen, M.D., 2013. The effect of alkali ions on the incorporation of aluminum in the calcium silicate hydrate (C-S-H) phase resulting from portland cement hydration studied by ^{29}Si MAS NMR. J. Am. Ceram. Soc. 96, 651–656. doi:10.1111/jace.12024.

Skibsted, J., Snellings, R., 2019. Reactivity of supplementary cementitious materials (SCMs) in cement blends. Cem. Concr. Res. 124, 105799. https://doi.org/10.1016/j.cemconres.2019.105799.

Sun, J., Wang, L., Yu, J., Guo, B., Chen, L., Zhang, Y., Wang, D., Shen, Z., Tsang, D.C.W., 2022. Cytotoxicity of stabilized/solidified municipal solid waste incineration fly ash. J. Hazard. Mater. 424. doi:10.1016/j.jhazmat.2021.127369.

Sun, Y., Xiong, X., He, M., Xu, Z., Hou, D., Zhang, W., Ok, Y.S., Rinklebe, J., Wang, L., Tsang, D.C.W., 2021. Roles of biochar-derived dissolved organic matter in soil amendment and environmental remediation: A critical review. Chem. Eng. J. https://doi.org/10.1016/j.cej.2021.130387.

Tan, K., Qin, Y., Du, T., Li, L., Zhang, L., Wang, J., 2021. Biochar from waste biomass as hygroscopic filler for pervious concrete to improve evaporative cooling performance. Constr. Build. Mater. 287. doi:10.1016/j.conbuildmat.2021.123078.

Tombesi, N., Pozo, K., Álvarez, M., Přibylová, P., Kukučka, P., Audy, O., Klánová, J., 2017. Tracking polychlorinated biphenyls (PCBs) and polybrominated diphenyl ethers (PBDEs) in sediments and soils from the southwest of Buenos Aires Province, Argentina (South eastern part of the GRULAC region). Sci. Total Environ. 575, 1470-1476. https://doi.org/10.1016/j.scitotenv.2016.10.013

Trinh, M.M., Tsai, C.L., Chang, M.B., 2019. Characterization of polybrominated diphenyl ethers (PBDEs) in various aqueous samples in Taiwan. Sci. Total Environ. 649, 388-395. https://doi.org/10.1016/j.scitotenv.2018.08.204

Tu, Z.; Guo, M. Z.; Poon, C. S.; Shi, C. Effects of limestone powder on $CaCO_3$ precipitation in CO_2 cured cement pastes. Cem. Concr. Compos. 2016, 72, 9–16, doi.org/10.1016/j.cemconcomp.2016.05.019.

US EPA 1311, Toxicity characteristic leaching procedure. US Environ. Prot. Agency, Washington, DC, USA, 1992.

USBI, How biochar & carbon credits work? Newsletter September 2021.

Vassilev, S. V., Baxter, D., Andersen, L.K., Vassileva, C.G., 2010. An overview of the chemical composition of biomass. Fuel. Res. 89, 913-933. https://doi.org/10.1016/j.fuel.2009.10.022.

Walling, S. A.; Provis, J. L. A discussion of the papers “Impact of hydrated magnesium carbonate additives on the carbonation of reactive MgO cements” and “enhancing the carbonation of MgO cement porous blocks through improved curing conditions”, Cem. Concr. Res. 2016, 79 424–426, doi.org/10.1016/j.cemconres.2015.09.010.

Wang, B., Fan, C., 2020. Hydration behavior and immobilization mechanism of MgO–SiO_2–H_2O cementitious system blended with MSWI fly ash. Chemosphere 250. doi:10.1016/j.chemosphere.2020.126269

Wang, B., Pang, B., 2019. Mechanical property and toughening mechanism of water reducing agents modified graphene nanoplatelets reinforced cement composites. Constr. Build. Mater. 226, 699–711. doi:10.1016/j.conbuildmat.2019.07.229.

Wang, L.; Chen, S. S.; Tsang, D. C. W.; Poon, C. S.; Shih, K., 2016. Recycling contaminated wood into eco-friendly particleboard using green cement and carbon dioxide curing. J. Clean. Prod. 2016, 137, 861–870, doi.org/10.1016/j.jclepro.2016.07.180.

Wang, Y.S., Dai, J.G., Wang, L., Tsang, D.C.W., Poon, C.S., 2018a. Influence of lead on stabilization/solidification by ordinary Portland cement and magnesium phosphate cement. Chemosphere 190, 90–96. doi:10.1016/j.chemosphere.2017.09.114.

Wang, L., Yu, K., Li, J.S., Tsang, D.C.W., Poon, C.S., Yoo, J.C., Baek, K., Ding, S., Hou, D., Dai, J.G., 2018b. Low-carbon and low-alkalinity stabilization/solidification of high-Pb contaminated soil. Chem. Eng. J. 351, 418–427. doi:10.1016/j.cej.2018.06.118.

Wang, L., Chen, L., Tsang, D.C.W., Li, J.S., Baek, K., Hou, D., Ding, S., Poon, C.S., 2018c. Recycling dredged sediment into fill materials, partition blocks, and paving blocks: Technical and economic assessment. J. Clean. Prod. 199, 69–76. doi:10.1016/j.jclepro.2018.07.165.

Wang, L., Cho, D.W., Tsang, D.C.W., Cao, X., Hou, D., Shen, Z., Alessi, D.S., Ok, Y.S., Poon, C.S., 2019a. Green remediation of As and Pb contaminated soil using cement-free clay-based stabilization/solidification. Environ. Int. 126, 336–345. doi:10.1016/j.envint.2019.02.057.

Wang, L.; Chen, L.; Tsang, D. C. W.; Kua, H. W.; Yang, J.; Ok, Y. S.; Ding, S.; Hou, D.; Poon, C. S., 2019b. The roles of biochar as green admixture for sediment-based construction products. Cem. Concr. Compos. 104, 103348, doi.org/10.1016/j.cemconcomp.2019.103348.

Wang, L.; Chen, L.; Cho, D. W.; Tsang, D. C. W.; Yang, J.; Hou, D.; Baek, K.; Kua, H. W.; Poon, C. S., 2019c. Novel synergy of Si-rich minerals and reactive MgO for stabilisation/solidification of contaminated sediment. J. Hazard. Mater. 365, 695–706, doi.org/10.1016/j.jhazmat.2018.11.067.

Wang, Y., Liu, Y., Zhan, W., Zheng, K., Wang, J., Zhang, C., Chen, R., 2020a. Stabilization of heavy metal-contaminated soils by biochar: Challenges and recommendations. Sci. Total Environ. 729, 139060. https://doi.org/10.1016/j.scitotenv.2020.139060

Wang, L.; Chen, L.; Tsang, D. C. W.; Guo, B.; Yang, J.; Shen, Z.; Hou, D.; Ok, Y. S.; Poon, C. S., 2020b. Biochar as green additives in cement-based composite with carbon dioxide curing. J. Clean. Prod. 258, 120678, doi.org/10.1016/j.jclepro.2020.120678.

Wang, L.; Chen, L.; Provis, J. L.; Tsang, D. C. W.; Poon, C. S., 2020c. Accelerated carbonation of reactive MgO and Portland cement blends under flowing CO_2 gas. Cem. Concr. Compos. 2020, 106, 103489, doi.org/10.1016/j.cemconcomp.2019.103489.

Wang, D.; Xiong, C.; Li, W.; Chang, J., 2020d Growth of calcium carbonate induced by accelerated carbonation of tricalcium silicate. ACS Sustain. Chem. Eng. 2020, 8, 39, 14718-14731, doi.org/10.1021/acssuschemeng.0c02260.

Wang, L., Chen, L., Poon, C.S., Wang, C.H., Ok, Y.S., Mechtcherine, V., Tsang, D.C.W., 2021a. Roles of Biochar and CO_2 Curing in Sustainable Magnesia Cement-Based Composites. ACS Sustain. Chem. Eng. 9, 8603-8610. https://doi.org/10.1021/acssuschemeng.1c02008.

Wang, L., Ur Rehman, N., Curosu, I., Zhu, Z., Beigh, M.A.B., Liebscher, M., Chen, L., Tsang, D.C.W., Hempel, S., Mechtcherine, V., 2021b. On the use of limestone calcined clay cement (LC^3) in high-strength strain-hardening cement-based composites (HS-SHCC). Cem. Concr. Res. 144. doi:10.1016/j.cemconres.2021.106421.

Wang, L., Zhang, Y., Chen, L., Guo, B., Tan, Y., Sasaki, K., Tsang, D.C.W., 2022a. Designing novel magnesium oxysulfate cement for stabilization/solidification of municipal solid waste incineration fly ash. J. Hazard. Mater. 423. doi:10.1016/j.jhazmat.2021.127025.

Wang, Y. Y.; Jing, X. R.; Li, L. L.; Liu, W. J.; Tong, Z. H.; Jiang, H. Biotoxicity evaluations of three typical biochars using a simulated system of fast pyrolytic biochar extracts on organisms of three kingdoms. ACS Sustain. Chem. Eng. 2017, 5, 1, 481–488, doi.org/10.1021/acssuschemeng.6b01859.

Weber, K., Quicker, P., 2018. Properties of biochar. Fuel 217, 240–261. doi:10.1016/j.fuel.2017.12.054

Wei, D., Dave, R., Pfeffer, R., 2002. Mixing and characterization of nanosized powders: An assessment of different techniques. J. Nanoparticle Res. 4, 21-41.

https://doi.org/10.1023/A:1020184524538

World Bank, 2021. State and trends of carbon pricing 2021. Retrieved from https://openknowledge.worldbank.org/handle/10986/35620 (Accessed: 20. Sep. 2021).

Wu, H.L., Jin, F., Bo, Y.L., Du, Y.J., Zheng, J.X., 2018. Leaching and microstructural properties of lead contaminated kaolin stabilized by GGBS-MgO in semi-dynamic leaching tests. Constr. Build. Mater. 172, 626-634. https://doi.org/10.1016/j.conbuildmat.2018.03.164

Xiong, X.; Yu, I. K. M.; Cao, L.; Tsang, D. C. W.; Zhang, S.; Ok, Y. S. A review of biochar-based catalysts for chemical synthesis, biofuel production, and pollution control. Bioresour. Technol. 2017, 246, 254-270, doi.org/10.1016/j.biortech.2017.06.163.

Xuan, D.; Zhan, B.; Poon, C. S. A maturity approach to estimate compressive strength development of CO_2-cured concrete blocks. Cem. Concr. Compos. 2018, 85, 153–160. doi.org/10.1016/j.cemconcomp.2017.10.005.

Xue, Y., Liu, X., 2021. Detoxification, solidification and recycling of municipal solid waste incineration fly ash: A review. Chem. Eng. J. doi:10.1016/j.cej.2021.130349

Yakubu, Y., Zhou, J., Ping, D., Shu, Z., Chen, Y., 2018. Effects of pH dynamics on solidification/stabilization of municipal solid waste incineration fly ash. J. Environ. Manage. 207, 243–248. doi:10.1016/j.jenvman.2017.11.042

Yang, C.C., 1998. Effect of the transition zone on the elastic moduli of mortar. Cem. Concr. Res. 28, 727-736. https://doi.org/10.1016/S0008-8846(98)00035-0

Yang, H., Yan, R., Chen, H., Lee, D.H., Zheng, C., 2007. Characteristics of hemicellulose, cellulose and lignin pyrolysis. Fuel. 86, 1781-1788.

https://doi.org/10.1016/j.fuel.2006.12.013

Yang, H.J., Jeong, H.J., Bong, K.M., Jin, D.R., Kang, T.W., Ryu, H.S., Han, J.H., Yang, W.J., Jung, H., Hwang, S.H., Na, E.H., 2020. Organic matter and heavy metal in river sediments of southwestern coastal Korea: Spatial distributions, pollution, and ecological risk assessment. Mar. Pollut. Bull. 159, 111466. https://doi.org/10.1016/j.marpolbul.2020.111466

Yu, I.K.M., Xiong, X., Tsang, D.C.W., Wang, L., Hunt, A.J., Song, H., Shang, J., Ok, Y.S., Poon, C.S., 2019. Aluminium-biochar composites as sustainable heterogeneous catalysts for glucose isomerisation in a biorefinery. Green Chem. 21, 1267–1281. doi:10.1039/c8gc02466a

Yu, I.K.M., Xiong, X., Tsang, D.C.W., Wang, L., Hunt, A.J., Song, H., Shang, J., Ok, Y.S., Poon, C.S., 2019. Aluminium-biochar composites as sustainable heterogeneous catalysts for glucose isomerisation in a biorefinery. Green Chem. 21, 1267–1281. doi:10.1039/c8gc02466a.

Zahed, M.A., Salehi, S., Madadi, R., Hejabi, F., 2021. Biochar as a sustainable product for remediation of petroleum contaminated soil. Curr. Res. Green Sustain. Chem. 4, 100055. https://doi.org/10.1016/j.crgsc.2021.100055

Zhan, B. J.; Xuan, D. X.; Poon, C. S.; Scrivener, K. L. Characterization of interfacial transition zone in concrete prepared with carbonated modeled recycled concrete aggregates. Cem. Concr. Res. 2020, 136, 106175, doi.org/10.1016/j.cemconres.2020.106175.

Zhang, C., Zeng, G., Huang, D., Lai, C., Chen, M., Cheng, M., Tang, W., Tang, L., Dong, H., Huang, B., Tan, X., Wang, R., 2019. Biochar for environmental management: Mitigating greenhouse gas emissions, contaminant treatment, and potential negative impacts. Chem. Eng. J. doi:10.1016/j.cej.2019.05.139

Zhang, J., Liu, G., Chen, B., Song, D., Qi, J., Liu, X., 2014. Analysis of CO_2 Emission for the cement manufacturing with alternative raw materials: A LCA-based framework, in: Energy Procedia. pp. 2541–2545. doi:10.1016/j.egypro.2014.12.041.

Zhang, R.; Bassim, N.; Panesar, D. K. Characterization of Mg components in reactive MgO - Portland cement blends during hydration and carbonation. J. CO_2 Util. 2018, 27, 518–527, doi.org/10.1016/j.jcou.2018.08.025.

Zhang, R.; Panesar, D. K. Carbonated Binder Systems Containing Reactive MgO and Portland Cement: Strength, Chemical Composition and Pore Structure. J. Clean. Prod. 2020, 271, doi.org/10.1016/j.jclepro.2020.122021.

Zhang, R.; Panesar, D. K. Design of Carbonated R-MgO-PC Binder system: effect of r-MgO replacement level and water-to-binder ratio. J. Am. Ceram. Soc. 2020, 103, 1, 656-669, doi.org/10.1111/jace.16719.

Zhang, T.; Dieckmann, E.; Song, S.; Xie, J.; Yu, Z.; Cheeseman, C. Properties of magnesium silicate hydrate (M-S-H) cement mortars containing chicken feather fibres. Constr. Build. Mater. 2018, 180, 692–697, doi.org/10.1016/j.conbuildmat.2018.05.292.

Zhang, Y., Wang, L., Chen, L., Ma, B., Zhang, Y., Ni, W., Tsang, D.C.W., 2021. Treatment of municipal solid waste incineration fly ash: State-of-the-art technologies and future perspectives. J. Hazard. Mater. doi:10.1016/j.jhazmat.2021.125132

Zhao, C., Shao, B., Yan, M., Liu, Z., Liang, Q., He, Q., Wu, T., Liu, Y., Pan, Y., Huang, J., Wang, J., Liang, J., Tang, L., 2021. Activation of peroxymonosulfate by biochar-based catalysts and applications in the degradation of organic contaminants: A review. Chem. Eng. J. doi:10.1016/j.cej.2021.128829.

Zhao, Y., Wang, H.T., Lu, W.J., Damgaard, A., Christensen, T.H., 2009. Life-cycle assessment of the municipal solid waste management system in Hangzhou, China (EASEWASTE). Waste Manag. Res. 27, 399–406. doi:10.1177/0734242X09103823.

Zhu, Q.; Zeng, S.; Yu, Y. A model to stabilize CO_2 uptake capacity during carbonation-calcination cycles and its case of CaO-MgO. Environ. Sci. Technol. 2017, 51, 1, 552-559, doi.org/10.1021/acs.est.6b04100.

Appendix-Supplementary Information

Table S3.1 Chemical compositions of raw materials (wt.%).

Table S3.2 Phases and references used for Rietveld refinement in Q-XRD analysis.

Table S3.3 The quality of matching results for Q-XRD analysis.

Table S3.4 The content calculation of C-S-H gel based on Q-XRD analysis.

Table S3.5 Relative integral areas (%) for Q^n in biochar modified pastes.

Table S3.6 Pore size distribution and porosity (%) of biochar modified pastes.

Table S3.7 Immobilization efficiency of Pb in MSWI fly ash S/S blocks.

Table S4.1 Chemical compositions of magnesia cement and Portland cement.

Table S4.2 Mixture formulations (wt.%) of biochar-incorporated pastes.

Table S4.3 The functions expressing background, peak shift, peak-shape, and preferred orientation for Q-XRD analysis.

Table S4.4 Phases and references used for Rietveld refinement in Q-XRD analysis.

Table S4.5 Content calculation for DTG curves of air cured and CO_2 cured MC and MP pastes with biochar addition.

Table S4.6 Content calculation for Q-XRD analysis of air cured and CO2 cured MC and MP pastes with biochar addition.

Table S4.7 The quality of matching results for QXRD analysis.

Table S5.1 Example of cost-benefit analysis for biochar blocks.

Table S5.2 Contribution of each constituent on the overall benefit of biochar blocks.

Figure S3.1. SEM image of (a) & (c) RBC and (b) & (c) YBC.

Figure S3.2. Particle size distribution of MSWI fly ash.

Figure S3.3. TG of (a) biochar and (b) & (c) 28-d pastes with/without biochar addition.

Figure S3.4. ^{29}Si MAS NMR spectra of ordinary Portland cement.

Figure S3.5. Pore size distributions in 28-d pastes with/without biochar in the mixtures.

Figure S3.6. TG analysis of MSWI fly ash S/S blocks with/without biochar addition.

Figure S4.1. TG and XRD diffractograms of 28-d air cured MC and MP pastes with biochar addition.

Figure S4.2. Schematic diagram of internal curing effect of biochar in cement system.

Figure S4.3. SEM image of Air BC and CO_2 BC.

Figure S4.4. TG and XRD diffractograms of biochar-incorporated MC and MP pastes after 1-d CO_2 plus 6-d air curing.

Figure S4.5. Pore size distribution of 28-d air cured pastes with biochar addition.

Figure S4.6. Deconvolution results of DTG curves of 28-d air cured MC and MP pastes with biochar addition.

Figure S4.7. Deconvolution results of DTG curves of MC and MP pastes with biochar addition after 1-d CO_2 plus 6-d air curing.

Figure S4.8. Rietveld refinement of 28-d air cured MC and MP pastes with biochar addition.

Figure S4.9. Rietveld refinement of MC and MP pastes with biochar addition after 1-d CO_2 plus 6-d air curing.

Figure S5.1. SEM image of biochar.

Figure S5.2. Particle size distribution of raw materials.

Figure S5.3. System boundary of biochar blocks.

Table S3.1 Chemical compositions of raw materials (wt.%).

	Na_2O	MgO	Al_2O_3	SiO_2	SO_3	Cl	K_2O	CaO	Fe_2O_3
MSWI fly ash	8.47	1.06	0.95	4.56	5.24	21.00	4.32	51.40	0.59
OPC	0.17	1.38	4.79	18.99	4.52	0.79	0.79	65.70	3.10
RBC	0.00	0.62	0.18	88.90	0.57	0.23	6.15	1.12	0.15
YBC	0.00	6.45	0.64	15.40	14.10	1.68	6.84	50.60	1.60

MSWI fly ash: municipal solid waste incineration fly ash; OPC: ordinary Portland cement; RBC: rice husk biochar; YBC: yard waste biochar.

Table S3.2 Phases and references used for Rietveld refinement in Q-XRD analysis

COD ID	Phases	Formula	Space group	Reference
2310675	Dicalcium silicate	Ca_2SiO_4	Pbnm	Smith et al.,
8104367	Calcium silicate	Ca_3SiO_5	R3m	Nishi et al.,
1000017	Corundum	Al_2O_3	R-3c:H	Tsirelson et al.,
1001768	Portlandite	$Ca(OH)_2$	P-3m1	Desgranges et al.,
9015084	Ettringite	$Ca_6Al_2(SO_4)_3(OH)_{12}(H_2O)_{26}$	P31c	Goetz-Neunhoeffer et al.,

Note: XRD patterns of the phases was obtained from the Crystallography Open Database.

Table S3.3 The quality of matching results for QXRD analysis.

	R_p (%)	R_{wp} (%)	Re	GOF
Control	5.36	7.84	3.36	2.33
RBC-2	4.45	6.14	3.37	1.82
RBC-5	4.69	6.42	3.36	1.91
RBC-10	5.34	7.49	3.33	2.25
YBC-2	5.44	7.35	3.34	2.20
YBC-5	4.57	6.24	3.34	1.86
YBC-10	3.45	4.54	3.38	1.34

R_p: pattern factor R_{wp}: the weighted pattern factor; R_{ewp}: expected pattern factor GOF: the goodness of fit; A GOF value between 1.0 and 2.9 is generally considered satisfactory.

Table S3.4. The content calculation of C-S-H gel based on Q-XRD analysis.

	C-S-H gel (wt.%) *
Control	41.64
RBC-2	45.65
RBC-5	48.56
RBC-10	52.04
YBC-2	43.07
YBC-5	45.59
YBC-10	49.52

*: These values were C-S-H gel contents in dried samples without free water. Noted that the free water was removed from the samples by using solvent exchange method before the Q-XRD analysis.

C-S-H gel content = Amorphous content – dried biochar [a] / dried sample [b].

[a] Dried biochar = SSD biochar – water absorption rate × dried biochar

[b] Dried sample = Hydrated sample (containing free water) – free water in hydrated sample [c]

[c] Free water in hydrated sample = Total water (including water for cement and water in biochar) – bound water in hydrated sample [d]

[d] Bound water in hydrated sample = Bound water ratio in dried sample from TG analysis – (dried biochar + cement) / (100 - Bound water ratio in dried sample from TG analysis)

Table S3.5 Relative integral areas (%) for Q^n in paste.

	Q^0	Q^1	Q^2	Q^3	D_c
Control	62.4	21.5	16.1	-	1.43
R-10	48.3	27.8	21.0	2.9	1.52
Y-10	52.4	27.9	19.7	-	1.41

Table S3.6 Pore size distribution (mL g^{-1}) and porosity (%) of biochar modified pastes.

	Cumulative pore volume	Capillary pores (7-100 nm) [a]	Mesopores (100-10000 nm)	Air pores (10000-100000 nm)	Porosity
Control	0.0914	0.0610	0.0274	0.0030	18.2
RBC-2	0.0908	0.0619	0.0262	0.0027	17.8
RBC-10	0.0969	0.0720	0.0229	0.0020	17.7
YBC-2	0.0982	0.0630	0.0333	0.0020	18.8
YBC-10	0.1022	0.0705	0.0288	0.0029	19.0

[a]: The pore size classification was from the structural perspectives according to the reference [1], which was different from that of environmental adsorbents.

References

1. Penttala, V.E., 1989. strength and freezing durability of high- strength concretes 171–181.

Table S3.7: Immobilization efficiency of Pb in MSWI fly ash S/S blocks.

	Immobilization efficiency of Pb (%) [a]
C-70FA	98.1
C-80FA	95.6
C-90FA	74.8
R-70FA	98.2
R-80FA	96.1
R-90FA	78.9
Y-70FA	98.3
Y-80FA	96.2
Y-90FA	80.4

[a]: Immobilization efficiency = (leachability of MSWI fly ash before TCLP - leachability of S/S products after TCLP) ×100% / (leachability of MSWI fly ash before TCLP)

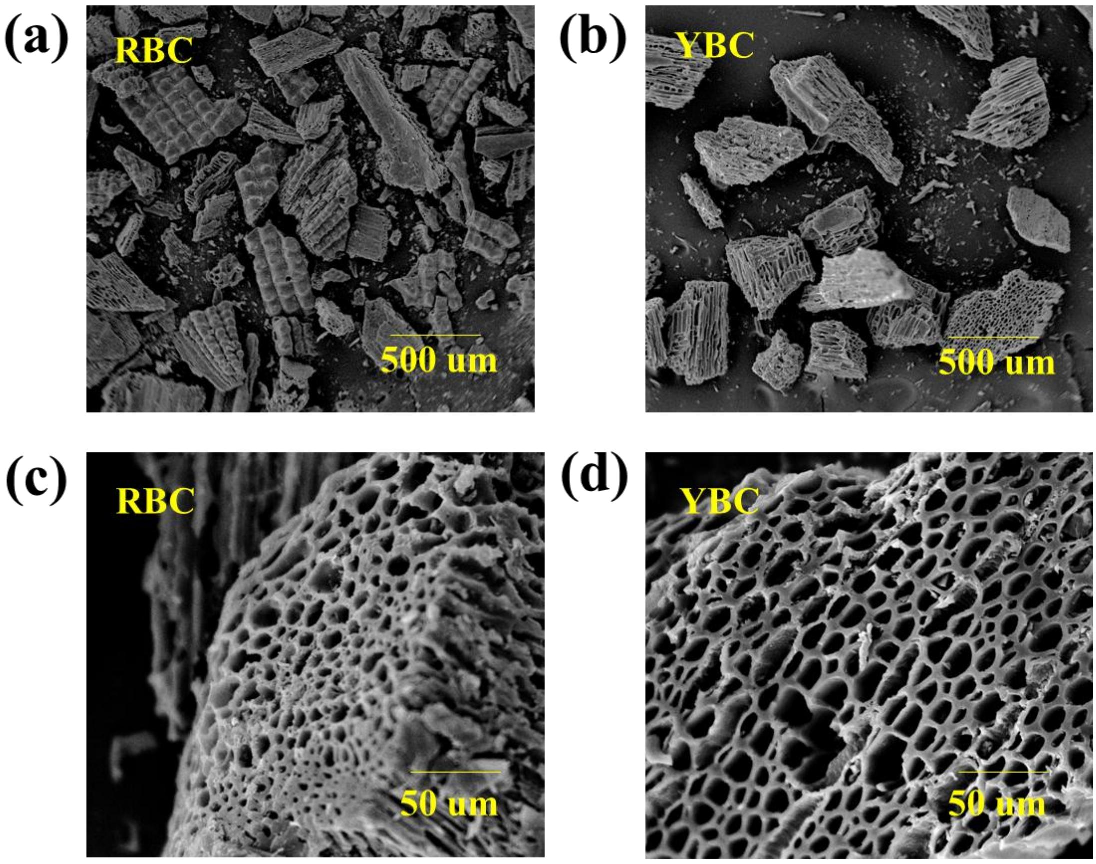

Figure S3.1. SEM image of (a) & (c) RBC and (b) & (c) YBC.

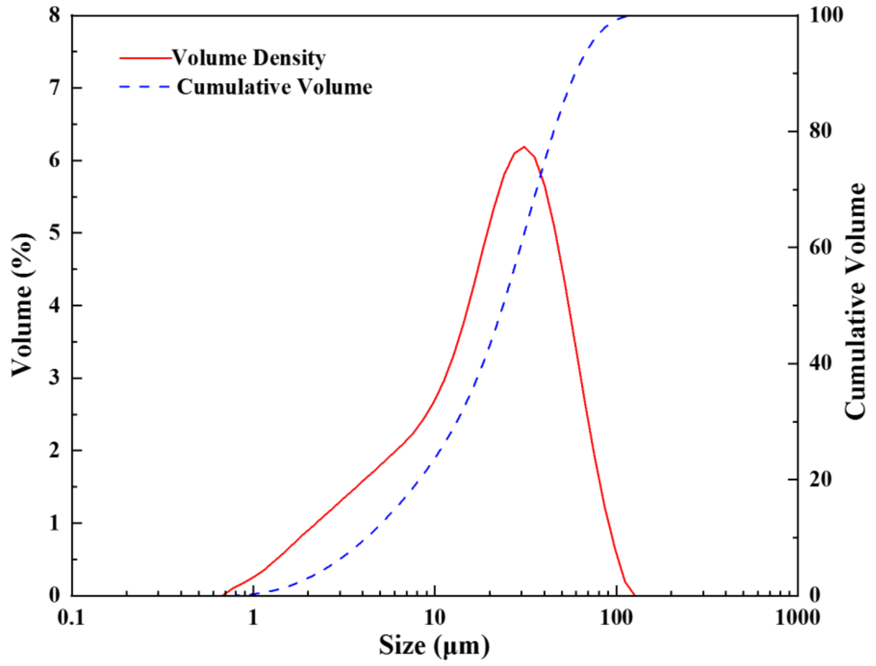

Figure S3.2. Particle size distribution of MSWI fly ash.

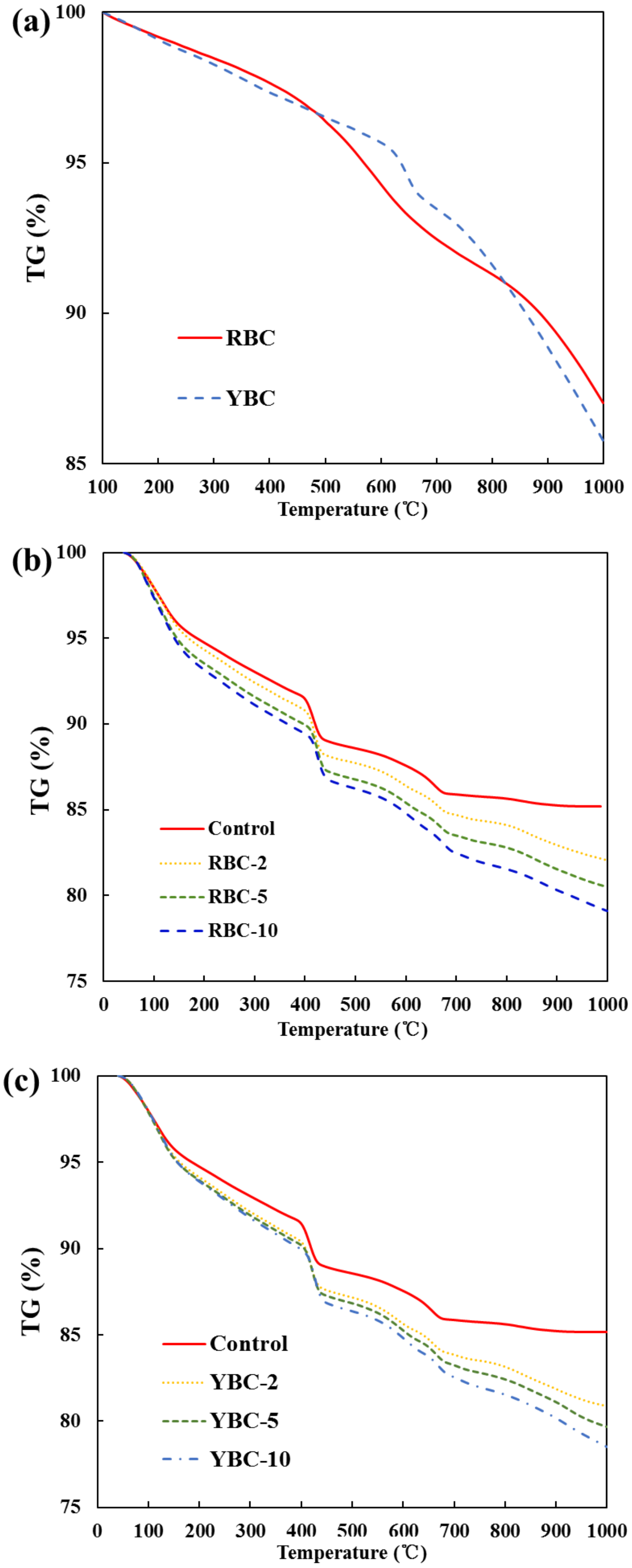

Figure S3.3. TG of (a) biochar and (b) & (c) 28-d pastes with/without biochar addition.

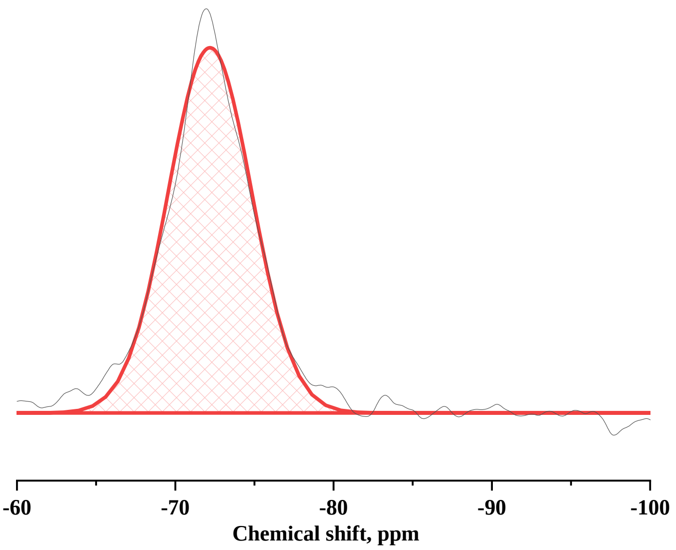

Figure S3.4. ^{29}Si MAS NMR spectra of ordinary Portland cement.

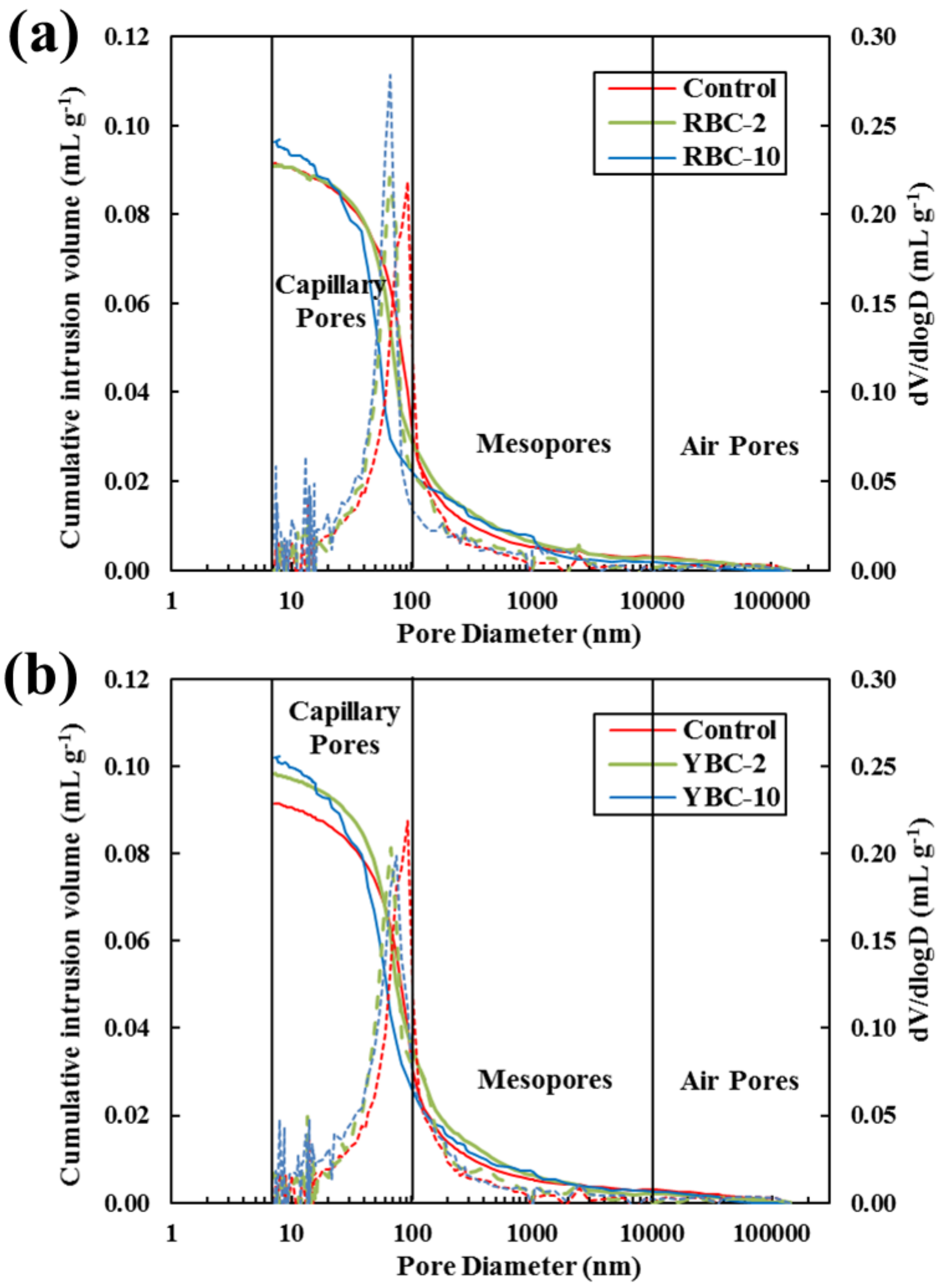

Figure S3.5. Pore size distributions in 28-d pastes with/without biochar in the mixtures.

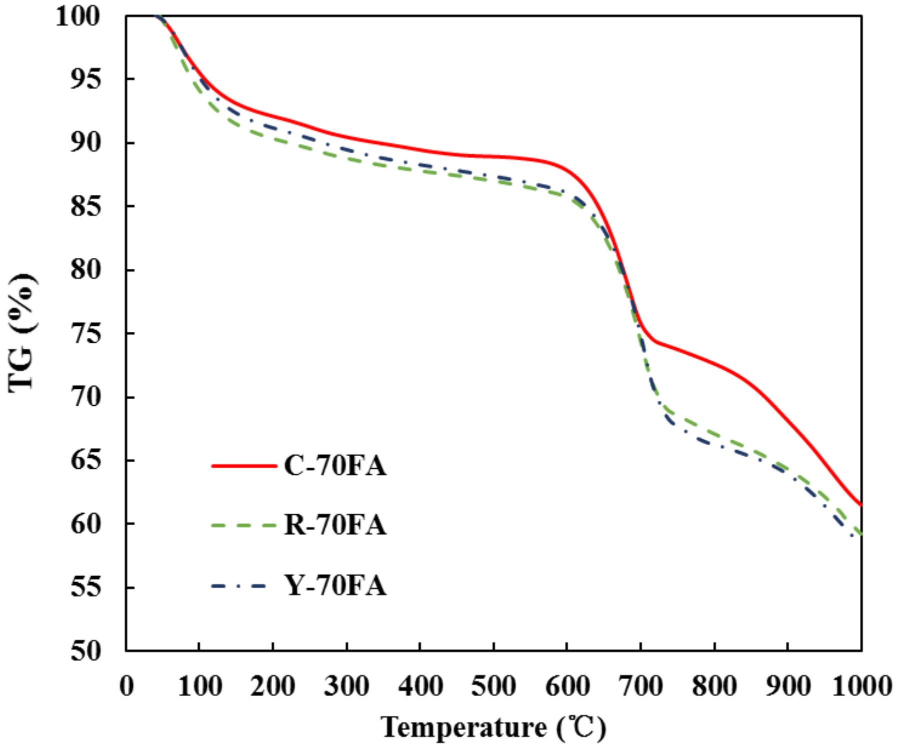

Figure S3.6. TG of MSWI fly ash S/S blocks with/without biochar addition.

Table S4.1 Chemical compositions of magnesia cement and Portland cement.

	Na_2O	MgO	Al_2O_3	SiO_2	P_2O_5	SO_3	K_2O	CaO	Fe_2O_3	LOI
MC	0.00	90.46	0.46	5.81	0.10	0.10	0.15	2.22	0.59	5.42
OPC	0.17	1.38	4.79	18.99	0.08	4.52	0.79	65.72	3.10	2.45

LOI: loss on ignition; MC: magnesia cement; OPC: ordinary Portland cement.

Table S4.2 Mixture formulations (wt.%) of biochar-incorporated pastes.

	MC (%)	OPC (%)	Air BC (%)	CO_2 BC (%)	Water to cement
MC	100	0	0	0	0.24
MC-Air BC	98	0	2	0	0.24
MC-CO_2 BC	98	0	0	2	0.24
MP	50	50	0	0	0.24
MP-Air BC	49	49	2	0	0.24
MP-CO_2 BC	49	49	0	2	0.24

BC: biochar; MC: magnesia cement; OPC: ordinary Portland cement; MP: 50% ordinary Portland cement and 50% magnesia cement.

Table S4.3 The functions expressing background, peak shift, peak-shape, and preferred orientation for Q-XRD analysis.

Model	**Function**
Background	B-spline
Peak shift	Shift axial displacement
Peak-shape	Split pseudo-Voigt
Preferred orientation	March-Dollase

Table S4.4 Phases and references used for Rietveld refinement in Q-XRD analysis (XRD patterns of the phases can be obtained from the Crystallography Open Database).

COD ID	Phases	Formula	Space group	Reference
1000054	Brucite	$Mg(OH)_2$	P-3m1	Zigan et al.,
2310675	Calcium silicate	Ca_2SiO_4	Pbnm	Smith et al.,
8104367	Calcium silicate oxide	Ca_3SiO_5	R3m	Nishi et al.,
1000017	Corundum	Al_2O_3	R-3c:H	Tsirelson et al.,
2101057	Magnesite	$MgCO_3$	R-3c:H	Maslen et al.,
7214217	Magnesium calcite	$Ca_{0.94}Mg_{0.06}CO_3$*	R-3c:H	Falini et al.,
1000053	Magnesium oxide	MgO	Fm-3m	Sasaki et al.,
1001768	Portlandite	$Ca(OH)_2$	P-3m1	Desgranges et al.,
1011172	Quartz	SiO_2	P3121	Brill et al.,

* The formula of magnesium calcite is presented as $Ca_xMg_{1-x}CO_3$ in XRD patterns due to the overlapping of different magnesium calcite phase.

Table S4.5(a) Content calculation for DTG curves of air cured and CO_2 cured MC pastes with biochar addition.

	28-d air cured			1-d CO_2 + 6-d air cured		
	MC	MC-Air BC	MC-CO_2 BC	MC	MC-Air BC	MC-CO_2 BC
Total mass loss (30-1000°C) (%)	20.88	21.97	21.42	25.22	27.78	27.66
Residual mass (%)	79.12	78.03	78.58	74.78	72.22	72.34
Integral area of $Mg(OH)_2$ (%)	72.82	72.22	72.92	50.31	50.00	49.47
Integral area of $MgCO_3$ (%)	21.97	22.05	21.88	19.35	16.53	14.60
Content of $Mg(OH)_2$	61.92	65.52	64.05	54.67	61.97	60.95
Content of $MgCO_3$	11.07	11.85	11.39	12.46	12.14	10.66

Table S4.5(b) Content calculation for DTG curves of air cured and CO_2 cured MP pastes with biochar addition.

	28-d air cured			1-d CO_2 + 6-d air cured		
	MP	MP-Air BC	MP-CO_2 BC	MP	MP-Air BC	MP-CO_2 BC
Total mass loss (30-1000°C) (%)	15.57	16.36	19.37	17.41	17.81	19.43
Residual mass (%)	84.43	83.64	80.63	82.59	82.19	80.57
Integral area of $Mg(OH)_2$ (%)	35.74	32.63	33.66	30.47	28.64	26.91
Integral area of $Ca(OH)_2$ (%)	8.40	7.08	6.32	9.11	8.48	6.64
Integral area of $MgCO_3$ (%)	24.72	23.06	20.05	19.11	19.03	21.72
Integral area of $CaCO_3$ (%)	12.17	20.36	20.99	20.52	26.07	28.08
Content of $Mg(OH)_2$[a]	21.23	20.57	26.06	20.70	20.00	20.91
Content of $Ca(OH)_2$[b]	6.37	5.69	6.24	7.89	7.55	6.58

Content of $MgCO_3$[c]	8.70	8.61	9.20	7.69	7.87	10.00
Content of $CaCO_3$[d]	5.10	9.05	11.46	9.83	12.84	15.39

Note: For comparison, the content values showed in this table have been renormalized to binder-biochar mass; Unit of the values is per unit mass of the anhydrous binder; The integral area was obtained from the statistical deconvolution results. The deconvolution of the overlapped peaks in DTG curves was conducted by fitting Gaussian peak profiles using the OriginPro 2021 software; see Figure S7 and S8.

[a] Content of $Mg(OH)_2$ = Total mass loss × integral area of $Mg(OH)_2$ × 58/18 / residual mass;

[b] Content of $Ca(OH)_2$ = Total mass loss × integral area of $Ca(OH)_2$ × 74/18 / residual mass;

[c] Content of $MgCO_3$ = Total mass loss × integral area of $MgCO_3$ × 84/44 / residual mass;

[d] Content of $CaCO_3$ = Total mass loss × integral area of $CaCO_3$× 100/44 / residual mass.

Table S4.6 Content calculation for Q-XRD analysis of air cured and CO_2 cured MC and MP pastes with biochar addition.

28-d air cured	MC	MC-Air BC	MC-CO_2 BC	MP	MP-Air BC	MP-CO_2 BC
Magnesium Oxide	56.37	51.77	52.69	35.65	34.55	33.49
Brucite	45.63	47.55	44.54	17.29	15.78	17.74
Magnesite	8.97	9.74	10.69	4.15	5.14	6.33
Magnesium Calcite	2.65	3.46	3.95	7.82	8.49	9.67
Quartz	1.39	1.28	1.53	1.18	1.79	1.49
Amorphous	11.38	14.35	13.87	17.88	18.77	20.71
Calcium Silicate Oxide	-	-	-	15.99	16.02	14.63
Calcium Silicate	-	-	-	10.90	11.60	11.91
Portlandite	-	-	-	7.58	7.41	8.06

1-d CO_2 + 6-d air cured	MC	MC-Air BC	MC-CO_2 BC	MP	MP-Air BC	MP-CO_2 BC
Magnesium Oxide	43.46	39.19	37.05	36.45	34.57	31.28
Brucite	45.87	49.57	50.32	13.68	12.78	14.52
Magnesite	18.32	20.49	21.43	10.17	11.44	12.41
Magnesium Calcite	10.30	11.63	12.03	11.50	13.26	14.52
Quartz	1.60	2.08	1.66	1.33	1.22	1.37
Amorphous	14.17	15.51	15.76	19.25	20.08	25.32
Calcium Silicate Oxide	-	-	-	8.48	9.86	9.93
Calcium Silicate	-	-	-	10.05	8.76	6.58
Portlandite	-	-	-	10.17	9.73	8.19

Note: For comparison, the values in this table have been renormalized to binder-biochar mass by dividing by the residual mass in TG results after dehydration and decarbonation; Unit of the values is per unit mass of the anhydrous binder.

Table S4.7 The quality of matching results for QXRD analysis.

Curing condition	Sample	R_{wp} (%)	GOF
28-d air cured	MC	5.38	2.56
	MC-Air BC	5.47	2.63
	MC-CO2 BC	5.67	2.73
	MP	5.10	2.30
	MP-Air BC	5.05	2.26
	MP-CO_2 BC	4.70	2.10
1-d CO_2 + 6-d air cured	MC	4.78	2.25
	MC-Air BC	5.22	2.52
	MC-CO_2 BC	5.06	2.42
	MP	5.10	2.30
	MP-Air BC	5.49	2.48
	MP-CO_2 BC	5.35	2.41

Rwp: the weighted pattern factor; GOF: the goodness of fit; A GOF value between 1.0 and 2.9 is generally considered satisfactory (Mertens et al., 2007).

Reference:

Mertens, G., Madau, P., Durinck, D., Blanpain, B., Elsen, J., 2007. Quantitative mineralogical analysis of hydraulic limes by X-ray diffraction. Cement and Concrete Research 37, 1524-1530.

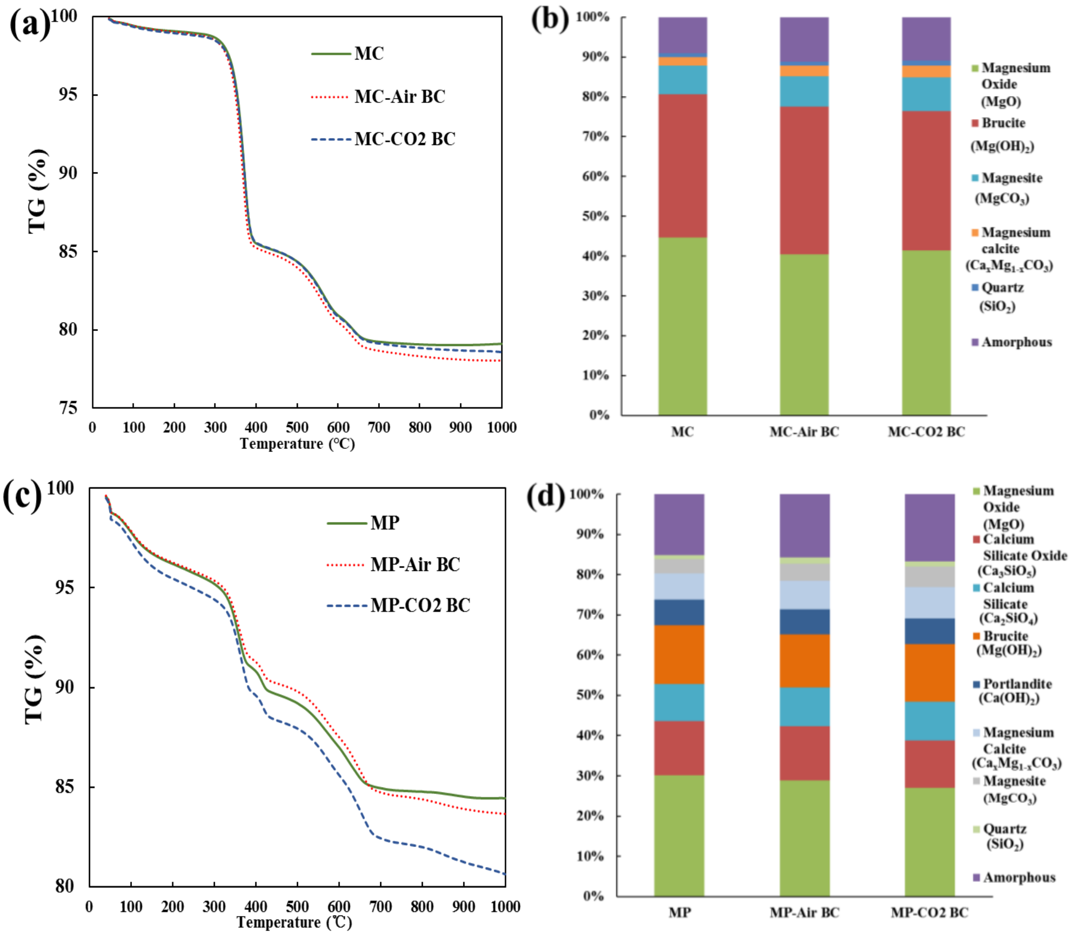

Figure S4.1. TG and Q-XRD analysis of 28-d air cured MC and MP pastes with biochar addition: (a) TG of MC pastes; (b) Q-XRD analysis of MC pastes; (c) TG of MP pastes; (d) Q-XRD analysis of MP pastes.

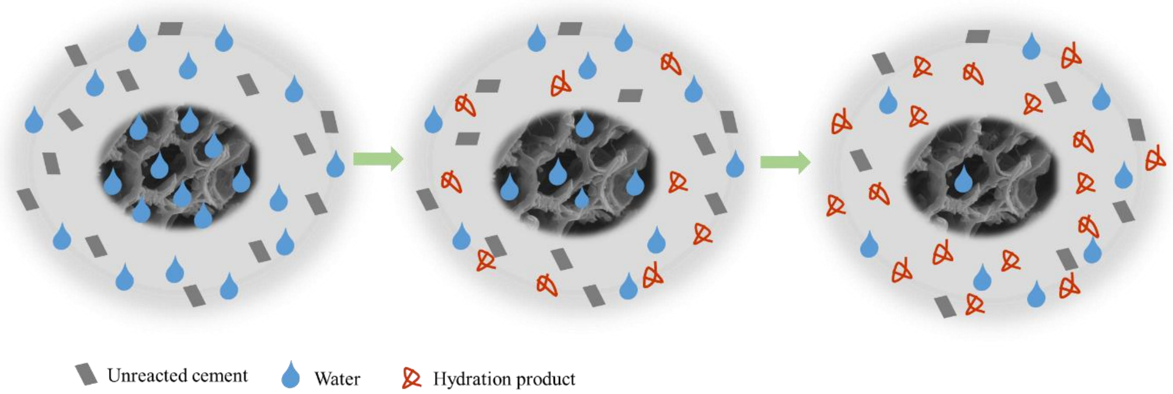

Figure S4.2. Schematic diagram of internal curing effect of biochar in cement system.

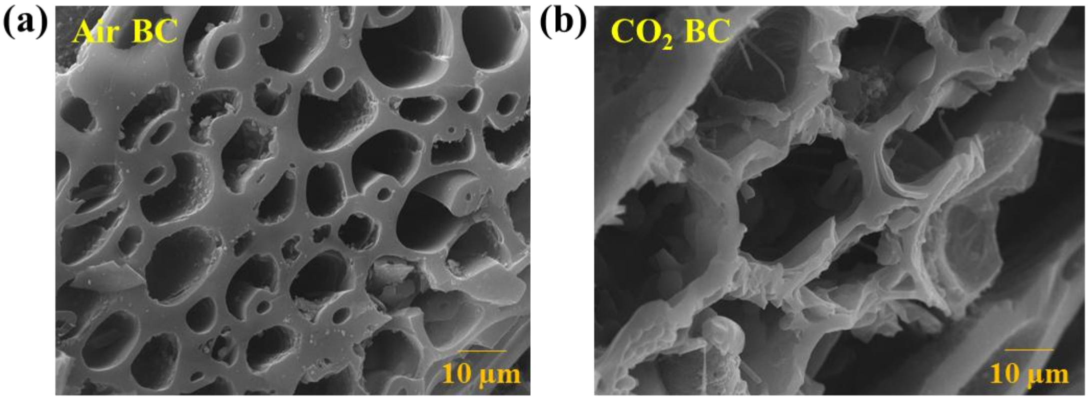

Figure S4.3. SEM image of (a) Air BC and (b) CO_2 BC.

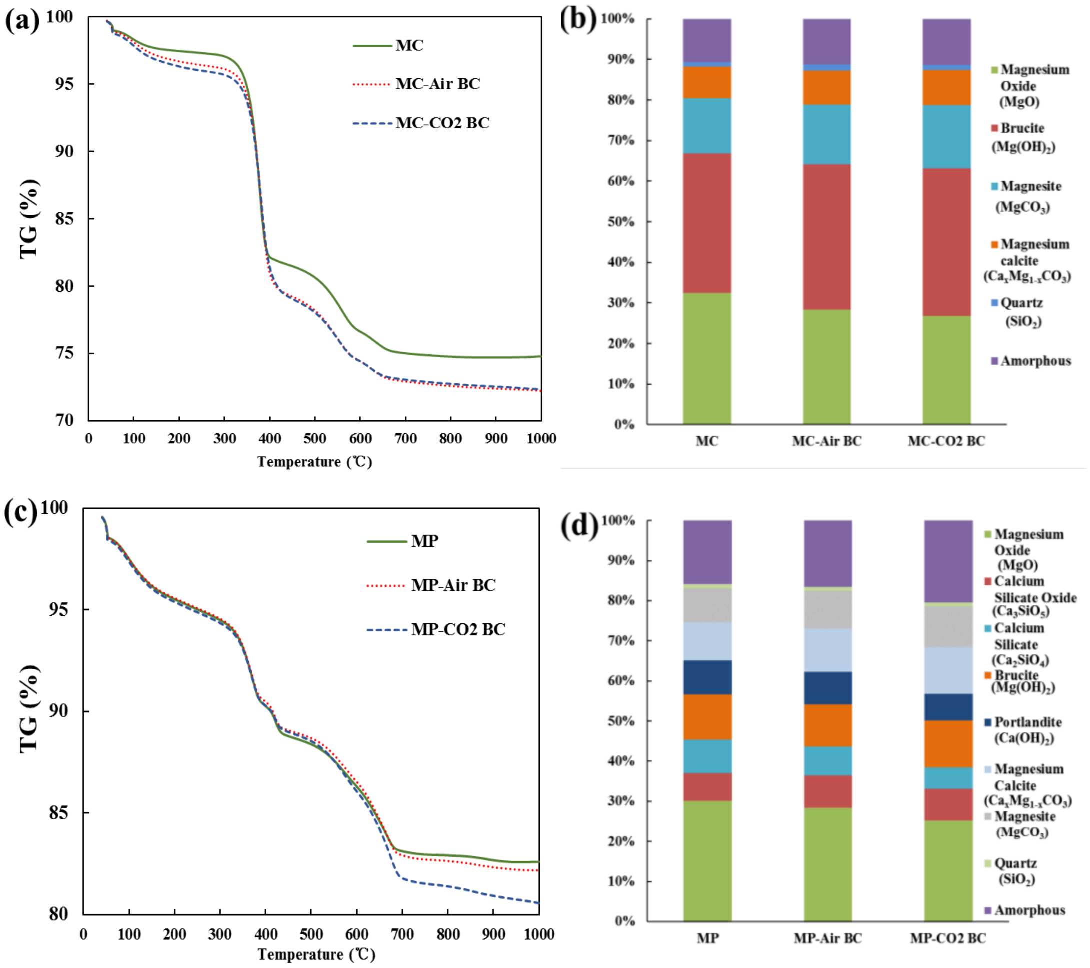

Figure S4.4. TG and Q-XRD analysis of biochar-incorporated MC and MP pastes after 1-d CO_2 plus 6-d air curing: (a) TG of CO_2 cured MC pastes; (b) Q-XRD analysis of CO_2 cured MC pastes; TG of CO_2 cured MP pastes; (b) Q-XRD analysis of CO_2 cured MP pastes.

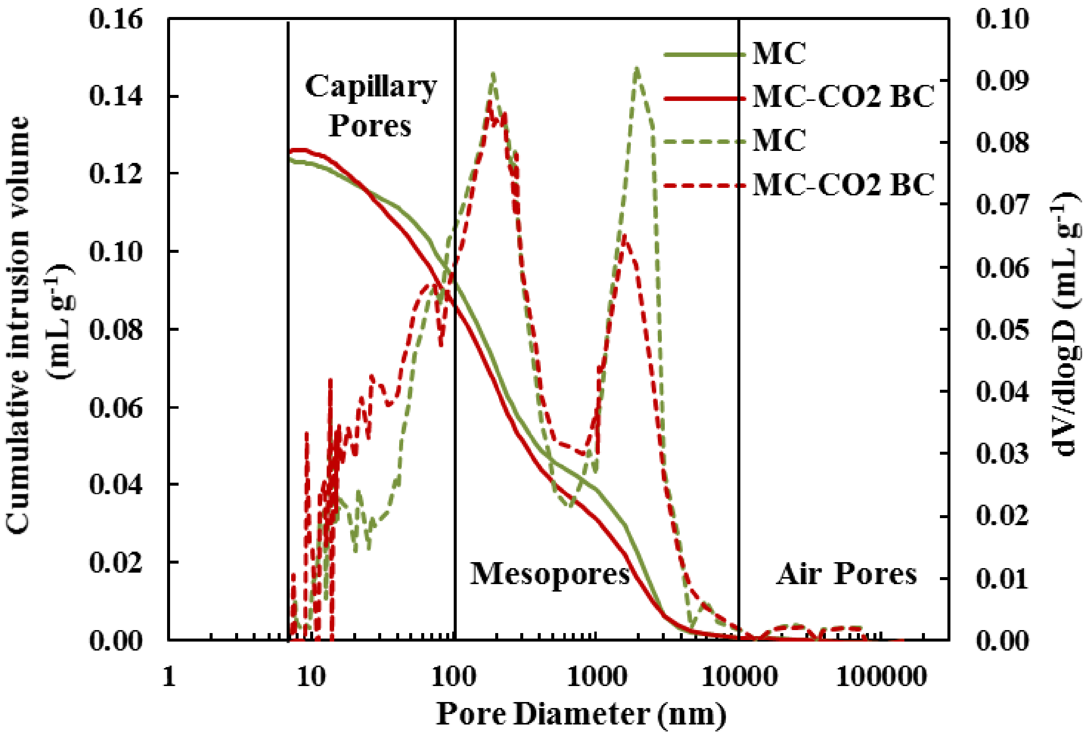

Figure S4.5. Pore size distribution of 28-d air cured blocks with biochar addition.

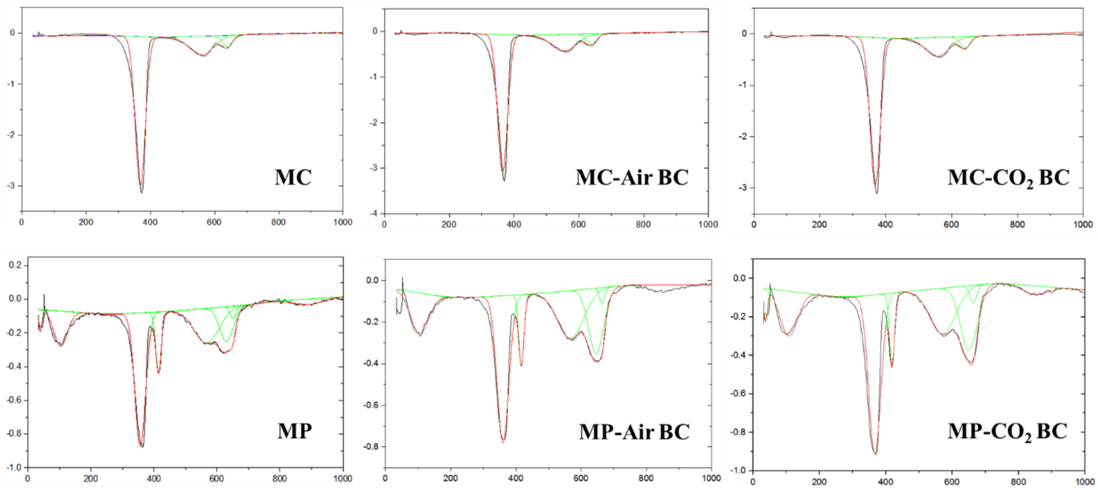

Figure S4.6. Deconvolution results of DTG curves of 28-d air cured MC and MP pastes with biochar addition.

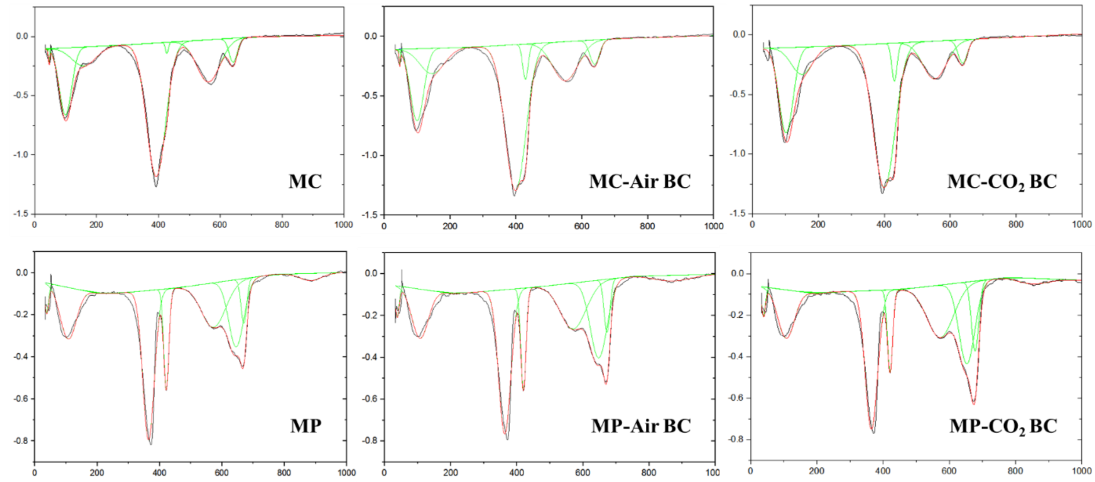

Figure S4.7. Deconvolution results of DTG curves of MC and MP pastes with biochar addition after 1-d CO_2 plus 6-d air curing.

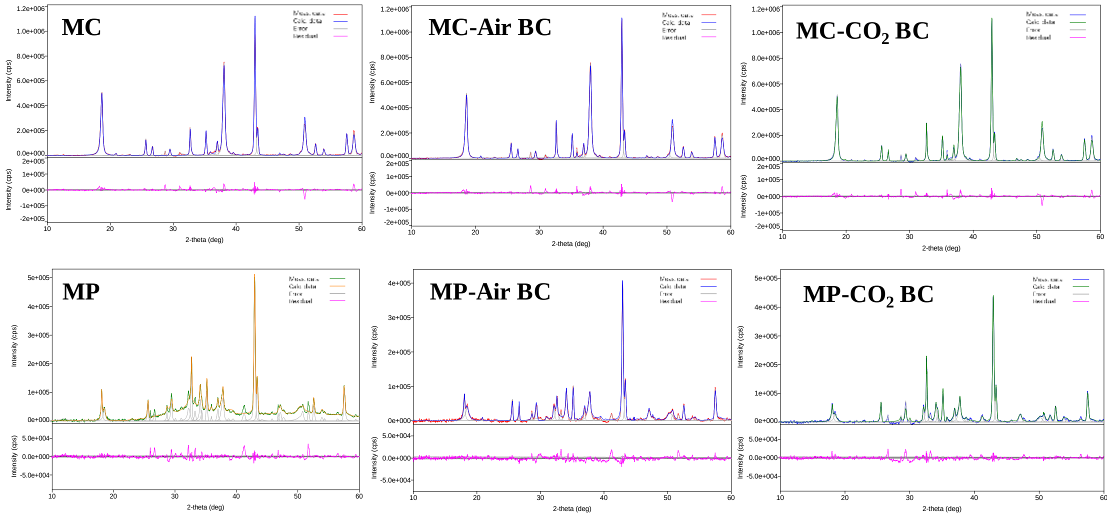

Figure S4.8. Rietveld refinement of 28-d air cured MC and MP pastes with biochar addition (The observed goodness of fit is noted in Table S4.7).

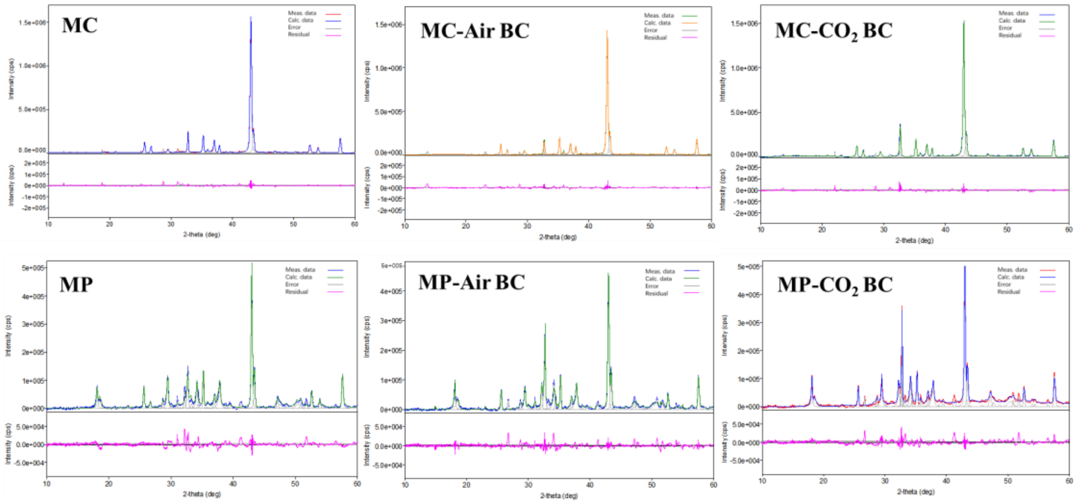

Figure S4.9. Rietveld refinement of MC and MP pastes with biochar addition after 1-d CO_2 plus 6-d air curing (The observed goodness of fit is noted in Table S4.7).

Table S5.1 Example of cost-benefit analysis for biochar blocks (30BC mixture).

Assuming the production capacity of factory is 100,000 blocks (Block size = 240 mm × 115 mm × 53 mm) per day and unit price is 53.7 USD per m^3.			
Capital costs (USD)	Unit Price	Price per m^3	Note
Land cost	769 m^{-2}	0.481	Sub-urban land for non-living activities (1000 m^2)
Building cost	923,077	0.577	Assuming 30-year operation
Production equipment	3,077	1.92	Assuming 30-year operation
Strength test equipment	7,692	0.00974	Strength test, 3-year service life
Total		2.99	
Operational costs	Unit Price	Price per m^3	
Materials cost		31.6	Cement etc. cost
Energy cost	0.15 kW·h^{-1}	1.17	Including electricity, fuel
Maintenance cost	15,384 y^{-1}	0.288	Machine maintenance
Labour cost	30.8 d^{-1}	10.5	Five workers
Curing cost	0	0	Air curing, the curing room was included in land cost
Total		43.6	
Comparative costs /benefits	Unit Price	Price per m^3	
Landfill disposal fee	25.6 t^{-1}	22.4	Recycling wood waste

saving (biochar)			
Landfill disposal fee saving (recycled aggregate)	9.1 t^{-1}	5.85	Recycling construction waste
Total		28.3	
Carbon tax/credit	Unit Price	Price per m^3	
Total	13.5 t^{-1}	-1.3	
Product benefit per m^3 = Price - Capital cost - Operational cost			7.11
Disposal fee saving per m^3 = Comparative cost/benefits			28.3
Over benefit per m^3 = Product benefit + Disposal fee saving + Carbon tax/credit			34.1

Table S5.2 Contribution of each constituent on the overall benefit of biochar blocks (USD m^{-3}).

	Product benefit	Disposal fee saving	Carbon tax/credit [a]	Overall benefit
Ref	1.9	12.0	-11.3	2.6
10BC	3.6	18.2	-7.7	14.1
20BC	5.3	23.6	-4.3	24.5
30BC	7.1	28.3	-1.3	34.1
30BC-BS	7.5	28.3	1.5	37.3
30BC-SF	3.5	28.3	1.5	33.3
30BC-FA	11.3	28.3	1.5	41.1
30BC-MK	5.8	28.3	1.3	35.4

[a]: Carbon tax/credit = CO_2 emissions tonne $^{-1}$ (kg) (Figure 10a) × 10^{-3} × block density [b] × 13.5 USD tonne $^{-1}$.

[b]: Block density: Ref = 2 tonne m^{-3}; 10BC = 1.9 tonne m^{-3}; 20BC = 1.8 tonne m^{-3}; 30BC = 1.7 tonne m^{-3}; 30BC-BS = 1.7 tonne m^{-3}; 30BC-SF = 1.7 tonne m^{-3}; 30BC-FA = 1.7 tonne m^{-3}; 30BC-MK = 1.7 tonne m^{-3};

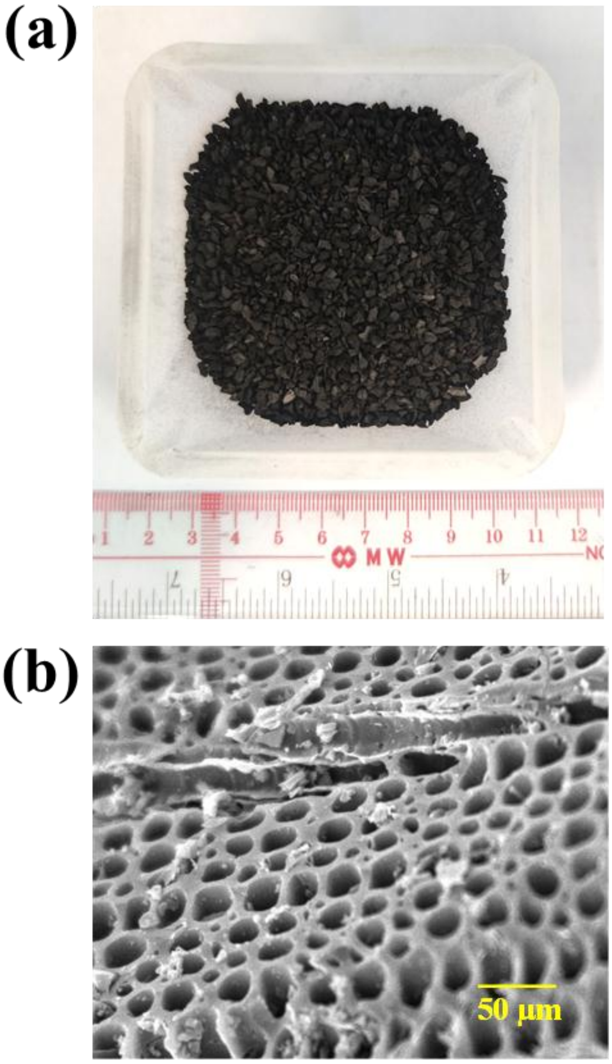

Figure S5.1. (a) Photo of biochar (b) SEM image of biochar.

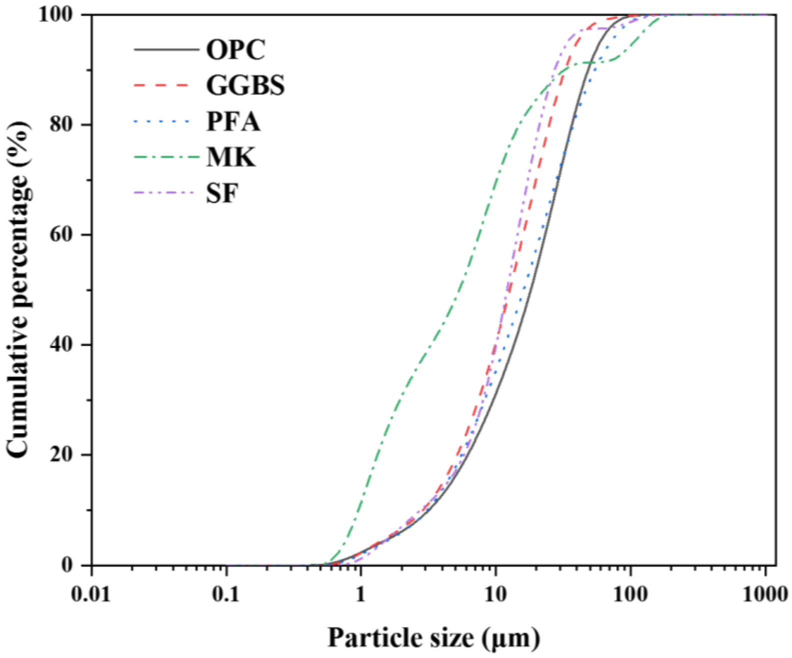

Figure S5.2. Particle size distribution of raw materials.

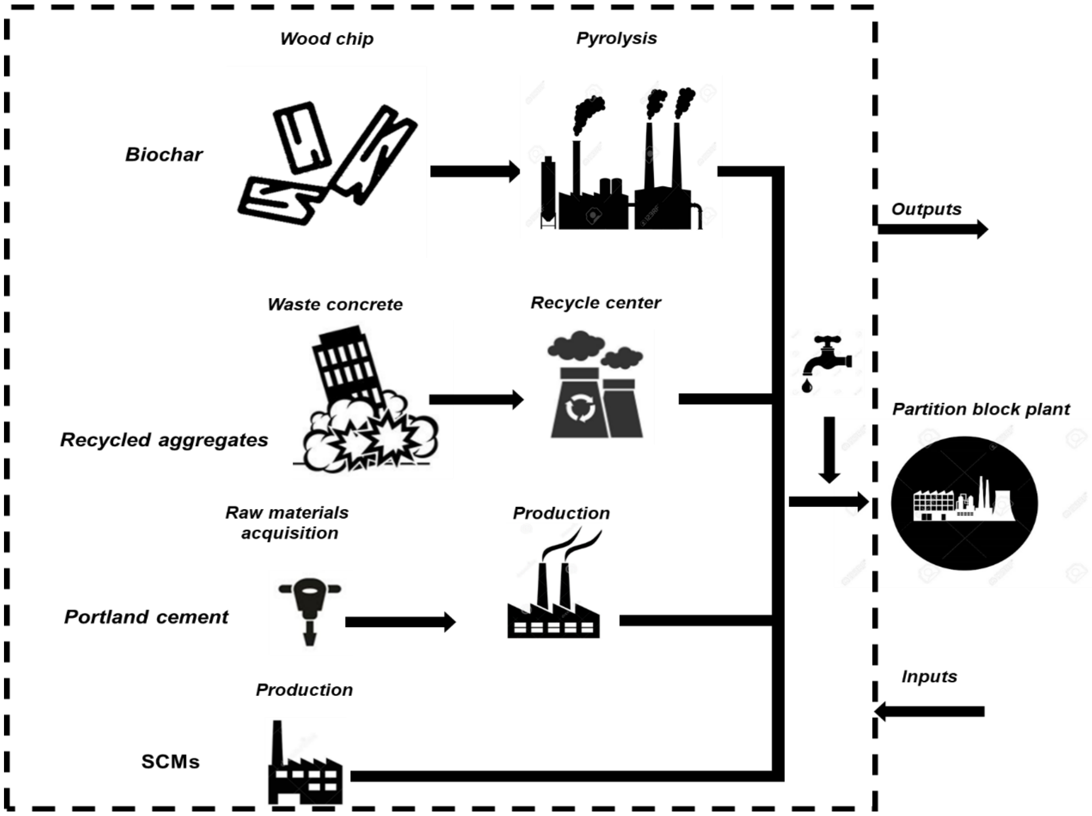

Figure S5.3. System boundary of biochar blocks.